

NUMERICAL INVESTIGATION OF AERODYNAMICS OF MISSILES WITH  
WRAP-AROUND TAIL FINS

A THESIS SUBMITTED TO  
THE GRADUATE SCHOOL OF NATURAL AND APPLIED SCIENCES  
OF  
MIDDLE EAST TECHNICAL UNIVERSITY

BY

UĞURTAN DEMİRTAŞ

IN PARTIAL FULFILLMENT OF THE REQUIREMENTS  
FOR  
THE DEGREE OF DOCTOR OF PHILOSOPHY  
IN  
AEROSPACE ENGINEERING

FEBRUARY 2024



Approval of the thesis:

**NUMERICAL INVESTIGATION OF AERODYNAMICS OF MISSILES  
WITH WRAP-AROUND TAIL FINS**

submitted by **Uğurtan Demirtaş** in partial fulfillment of the requirements for the degree of **Doctor of Philosophy in Aerospace Engineering, Middle East Technical University** by,

Prof. Dr. Halil Kalıpçılar  
Dean, Graduate School of **Natural and Applied Sciences**

Prof. Dr. Serkan Özgen  
Head of the Department, **Aerospace Engineering**

Assoc. Prof. Dr. Nilay Sezer Uzol  
Supervisor, **Aerospace Engineering, METU**

**Examining Committee Members:**

Prof. Dr. Sinan Eyi  
Aerospace Engineering, METU

Assoc. Prof. Dr. Nilay Sezer Uzol  
Aerospace Engineering, METU

Assist. Prof. Dr. Sıtkı Uslu  
Mechanical Engineering, TEDU

Prof. Dr. Yusuf Özyörük  
Aerospace Engineering, METU

Assist. Prof. Dr. Onur Baş  
Mechanical Engineering, TEDU

Date: 15.02.2024

**I hereby declare that all information in this document has been obtained and presented in accordance with academic rules and ethical conduct. I also declare that, as required by these rules and conduct, I have fully cited and referenced all material and results that are not original to this work.**

Name Last name : Uğurtan Demirtaş

Signature :

## ABSTRACT

### NUMERICAL INVESTIGATION OF AERODYNAMICS OF MISSILES WITH WRAP-AROUND TAIL FINS

Demirtaş, Uğurtan  
Doctor of Philosophy, Aerospace Engineering  
Supervisor : Assoc. Prof. Dr. Nilay Sezer Uzol

February 2024, 116 pages

This thesis investigates the aerodynamic characteristics of roll induction for missiles with wrap-around tail fins by performing steady-state RANS and unsteady URANS and DDES simulations. In RANS simulations, the effects of freestream Mach number and angle of attack on the roll moment coefficient are examined and compared with the wind tunnel results of Dahlke missile geometry. In order to analyze the effect of Riemann solver in unsteady cases, an exact Riemann solver is integrated into the open-source CFD flow solver SU2. In DDES simulations, the missile with wrap-around fins (WAF) is analyzed for Mach number of 0.5 and an angle of attack of  $10^\circ$  by using both exact Riemann solver (ER) and Roe's approximate Riemann solver (ROE). The results show that the ER solver exhibits smaller dominant frequencies with larger amplitude than of ROE solver for complex separated flow solutions of wrap-around fins. A missile geometry with basic planar fins is also used as a validation case for the prediction of static and dynamic aerodynamic coefficients by performing RANS and URANS simulations. Due to the absence of unsteady experimental validation data for the missile geometries, NACA 0021 and OAT 15A airfoils are analyzed by both ER and ROE Riemann solvers. DDES simulation is performed for NACA 0021 airfoil in deep stall case at an angle

of attack of  $60^\circ$ . ER solver shows smaller discrepancy in the frequency spectrum of the lift coefficient compared to the ROE solver with the experimental data. The URANS simulation is performed for OAT 15A airfoil in transonic shock buffeting case at Mach number of 0.73 and an angle of attack of  $3.9^\circ$ . There is no notable discrepancy with experimental data in the power spectral density of the pressure sensor located in the oscillatory shockwave path on the upper surface of the airfoil for both Riemann solvers.

Keywords: Wrap-Around Fin (WAF), Roll Induction, RANS, URANS, DDES, CFD, Riemann solver

## ÖZ

### SARMAL KUYRUK KANATÇIKLI FÜZELERİN AERODİNAMİĞİNİN SAYISAL OLARAK İNCELENMESİ

Demirtaş, Uğurtan  
Doktora, Havacılık ve Uzay Mühendisliği  
Tez Yöneticisi: Doç. Dr. Nilay Sezer Uzol

Şubat 2024, 116 sayfa

Bu tez, sarmal kuyruk kanatçıklı füzelerdeki dönme indüksiyonunun aerodinamik karakteristiklerini, daimî-durum RANS ve zamana-bağlı URANS ve DDES simülasyonları yaparak incelemektedir. RANS simülasyonlarında, serbest akış Mach sayısı ve hücum açısının dönme moment katsayısı üzerindeki etkileri Dahlke füze geometrisinin rüzgâr tüneli sonuçları ile karşılaştırılarak incelenmiştir. Zamana-bağlı durumda Riemann çözücüsünün etkisini analiz etmek için, bir kesin Riemann çözücü açık-kaynaklı HAD akış çözücü SU2 ile entegre edilmiştir. DDES simülasyonlarında, sarmal kanatçıklara (WAF) sahip füze 0.5 Mach sayısı ve 10° hücum açısında her iki kesin Riemann çözücü (ER) ve Roe'nun yaklaşık Riemann çözücüsü (ROE) ile analiz edilmiştir. Sonuçlar, sarmal kanatçıkların karmaşık kopmalı akışları için ER çözücünün ROE çözücüsüne göre daha büyük genliğe sahip daha küçük baskın frekanslar sergilediğini gösterir. Basit düzlemsel kanatçıklara sahip bir füze geometrisi de, daimi-durum RANS ve zamana-bağlı URANS simülasyonları yaparak statik ve dinamik aerodinamik katsayıların tahmininde bir doğrulama durumu olarak kullanılmıştır. Füze geometrileri için zamana-bağlı deneysel doğrulama verileri olmadığı için, NACA 0021 ve OAT 15A kanat kesitleri her iki ER ve ROE Riemann çözücüleri ile analiz edilmiştir. NACA 0021 kanat kesiti

için DDES simülasyonu derin stall durumunda,  $60^\circ$  hücum açısında yapılmıştır. ER çözücü, ROE çözücüsüne kıyasla taşıma katsayısının frekans spektrumunda deneysel verilerle daha küçük bir farklılık göstermiştir. OAT 15A kanat kesiti için, zamana-bağlı URANS simülasyonu transonik şok titreşim/darbe (buffeting) durumunda, 0.73 Mach sayısı ve  $3.9^\circ$  hücum açısında yapılmıştır. Kanat profilinin üst yüzeyindeki salınımlı şok dalgası yolunda yer alan basınç sensörünün güç spektral yoğunluğuyla karşılaştırıldığında Riemann çözücüler arasında belirgin bir fark gözlenmemiştir.

Anahtar Kelimeler: Sarmal Kanatçık, Dönme İndüksiyonu, RANS, URANS, DDES, HAD, Riemann Çözücü



## ACKNOWLEDGMENTS

I would like to express my deepest gratitude to the individuals and organizations who have significantly contributed to the completion of this Ph.D. thesis.

My sincere appreciation goes to my supervisor, Assoc. Prof. Dr. Nilay Sezer-Uzol, for her unwavering support, invaluable guidance, and scholarly mentorship throughout my doctoral journey. Her expertise and encouragement have been instrumental in shaping the trajectory of this research.

I would like to thank to my Thesis Progress Committee Members and Thesis Jury Members for their comments and support.

Heartfelt thanks to my parents for their unconditional love, unwavering support, and endless encouragement. Their belief in my capabilities has been a constant source of inspiration.

I appreciate Dr. Mustafa Özgür Ateşođlu for his collaboration, valuable insights, and the intellectual discussions upon flight mechanics that have shaped the conceptual framework of this work.

Acknowledgments to my colleagues Arda Dođancı, Hasan Bařaran, and Emirhan Evin for their cooperation during professional life.

My thanks to Merve Karatař, MD, for her expertise, contributions, and collaboration in editorial tasks during writing stage.

I express my gratitude to Prof. Dr. Umut Orguner for his insightful contributions, scholarly advice, and constructive feedback that significantly enriched my intellectual depth during my studies.

Special thanks to Dr. ađrı Urfalı Mamatođlu and Günes Mamatođlu for their friendly and warm support when I felt myself hopeless.

I am grateful for the support of ROKETSAN during this Ph.D. thesis study while working at ROKETSAN. ROKETSAN's support has significantly contributed to the successful completion of this research.

I express my gratitude to TÜBİTAK ULAKBİM for providing the use of HPC parallel supercomputers of TRUBA during this Ph.D. thesis study. The CFD calculations reported in this thesis were fully performed at TUBITAK ULAKBİM, High Performance and Grid Computing Center (TRUBA resources).

## TABLE OF CONTENTS

ABSTRACT.....	v
ÖZ.....	vii
ACKNOWLEDGMENTS.....	ix
TABLE OF CONTENTS.....	xi
LIST OF TABLES.....	xiv
LIST OF FIGURES.....	xv
LIST OF ABBREVIATIONS.....	xix
LIST OF SYMBOLS.....	xxi
1 INTRODUCTION.....	1
1.1 Literature Review on Missiles with Wrap-Around Tail Fins.....	1
1.2 Literature Review on Computational Fluid Dynamics.....	5
1.3 Thesis Motivation and Objectives.....	8
1.4 Thesis Outline.....	10
2 NUMERICAL METHODOLOGIES.....	13
2.1 Nonlinear Hyperbolic Partial Differential Equations.....	13
2.1.1 Scalar Nonlinear Hyperbolic Equations.....	14
2.1.2 Euler Equations.....	17
2.1.3 Finite Volume Method.....	18
2.1.4 Riemann Problem in Finite Volume Method.....	20
2.1.5 Roe’s Approximate Riemann Solver.....	21
2.1.6 Exact Riemann Solver.....	23
2.2 Compressible Navier-Stokes Equations.....	26

2.3	Reynolds-Averaged Navier-Stokes Equations .....	28
2.4	Detached Eddy Simulation with Spalart-Allmaras Model .....	30
2.5	Dynamic Aerodynamic Coefficients .....	32
2.5.1	Pitch Damping Coefficient and Dynamic Stability .....	32
3	COMPUTATIONAL TEST CASES .....	37
3.1	Basic Finner Geometry .....	39
3.2	Dahlke Geometry .....	39
3.3	NACA 0021 Airfoil in Deep Stall .....	41
3.4	OAT 15A Airfoil in Transonic Flow .....	42
4	RESULTS FOR MISSILE CFD SIMULATIONS .....	43
4.1	CFD Simulations for Missile with Basic Fins .....	43
4.1.1	Grid Independence Study .....	43
4.1.2	Steady-State Simulations: RANS Results .....	47
4.1.3	Unsteady Simulations: URANS Results for Dynamic Coefficients.....	52
4.1.4	Summary and Discussions .....	55
4.2	CFD Simulations for Missile with Wrap-Around Fins .....	56
4.2.1	Grid Independence Study .....	56
4.2.2	Roll Induction for Missiles with Wrap-Around Fins .....	61
4.2.3	DDES Results of Missile with WAFs .....	72
4.2.4	Summary and Discussions .....	86
5	RESULTS FOR AIRFOIL CFD SIMULATIONS .....	87
5.1	NACA 0021 Airfoil in Deep Stall .....	87
5.1.1	Grid Independence Study .....	88
5.1.2	Results of DDES Simulations .....	91

5.1.3	Computational Performance .....	94
5.2	OAT 15A Airfoil in Transonic Flow .....	95
5.2.1	Grid Independence Study .....	95
5.2.2	Results of URANS Simulations .....	99
6	CONCLUSIONS .....	103
	REFERENCES .....	107
	CURRICULUM VITAE .....	116

## LIST OF TABLES

### TABLES

Table 1.1 Computational Test Cases .....	10
Table 4.1 Basic Finner: Grid Independence Study for RANS Simulations .....	44
Table 4.2 Basic Finner - RANS Results: Aerodynamics Coefficients at $M = 0.766$ .....	48
Table 4.3 Basic Finner - RANS Results: Aerodynamics Coefficients at $M = 0.934$ .....	48
Table 4.4 Basic Finner - URANS: CFD Simulation Parameters at $M = 0.766$ .....	52
Table 4.5 Basic Finner - URANS Results: $(C_{Mq} + C_{M\dot{\alpha}})$ Calculations.....	54
Table 4.6 Missile with WAFs: Grid Independence Study for RANS Simulations .	57
Table 4.7 Missile with WAF: Grid Independence Study for DDES Simulations ...	73
Table 5.1 NACA 0021 Airfoil: Grid Independence Study .....	90
Table 5.2 OAT 15A Airfoil: Grid Independence Study for RANS Simulations.....	97
Table 5.3 OAT 15A Airfoil - RANS Results: Aerodynamic Coefficients .....	97

## LIST OF FIGURES

### FIGURES

Figure 2.1: The boundary values of conserved variable $u$ and flux function $f$ at a discontinuity.....	16
Figure 2.2: The Riemann Problem in 1D Euler Equations .....	21
Figure 2.3: Riemann problem in finite volume method.....	24
Figure 2.4: Exact Riemann solver shock capturing algorithm.....	25
Figure 2.5: a) Pitching and b) Plunging Motion of a Missile .....	33
Figure 2.6: Pitching Moment Hysteresis Curve with respect to Angle of Attack ..	35
Figure 3.1: Basic Finner: Missile Model Geometry with Basic Fins.....	39
Figure 3.2: NACA 0021 Airfoil.....	41
Figure 3.3: OAT 15A Airfoil .....	42
Figure 4.1: Basic Finner: Unstructured Grid .....	44
Figure 4.2: Basic Finner: $y^+$ contours on the surface.....	45
Figure 4.3: Basic Finner: Residual Plots for the Coarse and Medium Grids.....	45
Figure 4.4: Basic Finner: Residual Plots for the Fine and Finest grids .....	46
Figure 4.5: Basic Finner: Axial Force Coefficient ( $C_{Fx}$ ) Grid Dependency .....	47
Figure 4.6: Basic Finner: Roll Moment Coefficient ( $C_{Mx}$ ) Grid Dependency .....	47
Figure 4.7: Basic Finner: Pressure contours at sea level for $M_\infty = 0.766$ at different angles of attack of $\alpha = 0^\circ, 5^\circ, 10^\circ$ .....	50
Figure 4.8: Basic Finner: Mach contours at sea level for $M_\infty = 0.766$ at different angles of attack of $\alpha = 0^\circ, 5^\circ, 10^\circ$ .....	51
Figure 4.9: Basic Finner: Normal Force Coefficient ( $C_{Fz}$ ) vs Time .....	53
Figure 4.10: Basic Finner: Pitching Moment Coefficient ( $C_{My}$ ) vs Time .....	53
Figure 4.11: Basic Finner: Pitching Moment Coefficient Hysteresis Curve .....	54
Figure 4.12: Basic Finner: Pitch Damping Coefficient ( $C_{Mq} + C_{M\dot{\alpha}}$ ) vs Time.....	55
Figure 4.13: Missile with WAFs: Unstructured Grid .....	56
Figure 4.14: Missile with WAFs: $y^+$ contours on the surface grid .....	57
Figure 4.15: Missile with WAFs: Residual plots for coarse grid .....	58

Figure 4.16: Missile with WAFs: Residual plots for medium grid .....	58
Figure 4.17: Missile with WAFs: Residual plots for fine grid .....	59
Figure 4.18: Missile with WAFs: Residual plots for finest grid .....	59
Figure 4.19: Missile with WAFs: Roll Moment Coefficient Grid Dependency .....	60
Figure 4.20: Missile with WAFs: Axial Force Coefficient Grid Dependency .....	60
Figure 4.21: Missile with WAFs: Roll Induction in Subsonic Flow .....	61
Figure 4.22: Missile with WAFs: Comparison of CFD results with Dahlke wind tunnel tests .....	62
Figure 4.23: Missile with WAFs: Mach Contours at M = 0.6 for .....	63
Figure 4.24: Missile with WAFs: Mach Contours at M = 0.6 for .....	63
Figure 4.25: Missile with WAFs: Mach contours for different Mach number flow conditions at M = 0.6, 0.937, 1.053, and 1.1 for RANS simulations with SA turbulence model by using ER (left) and ROE (right) Riemann solvers.....	65
Figure 4.26: Missile with WAFs: Mach contours for different Mach number flow conditions at M = 0.6, 0.937, 1.053, and 1.1 for RANS simulations with <i>k-<math>\omega</math></i> SST turbulence model by using ER (left) and ROE (right) Riemann solvers.....	66
Figure 4.27: Missile with WAFs: Pressure Coefficient Distribution at M = 1.1.....	67
Figure 4.28: Missile with WAFs: Pressure Coefficient vs Chord along Midspan on Tail 3.....	67
Figure 4.29: Missile with WAFs: Normal Force Coefficient ( $C_{Fz}$ ).....	69
Figure 4.30: Missile with WAFs: Roll Moment Coefficient ( $C_{Mx}$ ).....	69
Figure 4.31: Missile with WAFs: Partial $C_{Mx}$ contributions of body parts (Body only, Tail 1 and 3, Tail 2 only and Tail 4 only) at M = 0.5 .....	70
Figure 4.32: Missile with WAFs: Velocity decomposition on Tail 2 in a nonzero Angle of Attack .....	70
Figure 4.33: Missile with WAFs: Expansion and compression in Tail 2 in a nonzero Angle of Attack .....	71
Figure 4.34: Missile with WAFs: Mach contours using DES (M = 0.5, $\alpha = 10^\circ$ )...	72
Figure 4.35: Missile with WAFs: RANS/LES index change along the tail percentage of chord from leading edge (LE) to trailing edge (TE) .....	74



Figure 4.36: Missile with WAFs: RANS/LES index change in the wake and tail downstream at the mid-section vertical plane.....	74
Figure 4.37: Missile with WAFs: $C_{Fx}$ signal in time domain .....	75
Figure 4.38: Missile with WAFs: $C_{Fy}$ signal in time domain .....	75
Figure 4.39: Missile with WAFs: $C_{Fz}$ signal in time domain.....	76
Figure 4.40: Missile with WAFs: Comparison of two halves in FFT spectrum (ER) .....	77
Figure 4.41: Missile with WAFs: Comparison of two halves in FFT spectrum (ROE).....	77
Figure 4.42: Missile with WAFs: FFT spectrum of $C_{Fz}$ signal.....	78
Figure 4.43: Missile with WAFs: FFT Spectrum Comparison (Tail 1).....	79
Figure 4.44: Missile with WAFs: FFT Spectrum Comparison (Tail 3).....	79
Figure 4.45: Missile with WAFs: Time accurate DDES Simulations: Instantaneous streamlines at $t = 4.5e-4$ s and $t = 9e-4$ s around the tip, mid, and root regions of wrap-around fins and Mach contours at the centerline cut plane. ....	81
Figure 4.46: Missile with WAFs: Time accurate DDES Simulations: Instantaneous streamlines at $t = 13.5e-4$ s and $t = 27e-4$ s around the tip, mid, and root regions of wrap-around fins and Mach contours at the centerline cut plane. ....	82
Figure 4.47: Missile with WAFs: Time accurate DDES Simulations: Instantaneous Q-criterion iso-surfaces over Tail 1 (left) and Tail 3 (right).....	83
Figure 4.48: Missile with WAFs: Time accurate DDES Simulations: Instantaneous coefficient of pressure iso-surfaces over Tail 1 (left) and Tail 3 (right).....	84
Figure 4.49: Missile with WAFs: Time accurate DDES Simulations: Instantaneous coefficient of pressure distribution over Tail 1 (left) and Tail 3 (right) .....	85
Figure 5.1: NACA 0021 Airfoil: Cylindrical Computational Domain and Unstructured Grid .....	88
Figure 5.2: NACA 0021 Airfoil: Unstructured Grid.....	89
Figure 5.3: NACA 0021 Airfoil: Rectangular Surface Mesh .....	89
Figure 5.4: NACA 0021 Airfoil - RANS Results: Time-Averaged Pressure Coefficient Distribution .....	90

Figure 5.5: NACA 0021 Airfoil - DDES Results: Time History of Lift Coefficient .....	92
Figure 5.6: NACA 0021 Airfoil - DDES Results: FFT spectrum - Lift Coefficient vs Strouhal number (St) using Exact Riemann (ER) and Approximate Riemann (ROE) Solvers .....	93
Figure 5.7: NACA 0021 Airfoil - DDES Results: Time-Averaged Pressure Coefficient Distribution using ER Riemann solver .....	93
Figure 5.8: NACA 0021 Airfoil - DDES Results: Time-Averaged Pressure Coefficient Distribution using ROE Riemann solver .....	94
Figure 5.9: NACA 0021 Airfoil - DDES Results: Computational Performance of ER and ROE Methods by taking moving-average of 5000 iterations .....	95
Figure 5.10: OAT 15A Airfoil: Computational Domain and Structured Grid .....	96
Figure 5.11: OAT 15A Airfoil: Structured O-Grid around the Airfoil .....	97
Figure 5.12: OAT 15A Airfoil - RANS Results: Residual Plots for the Coarse, Medium, and Fine Grids .....	98
Figure 5.13: OAT 15A Airfoil - URANS Results: Time-Averaged Pressure Coefficient Distribution at $M = 0.73$ and $\alpha = 3.9^\circ$ .....	100
Figure 5.14: OAT 15A Airfoil - URANS Results: Time History of Pressure .....	100
Figure 5.15: OAT 15A Airfoil - URANS Results: Power Spectral Density (PSD) of Pressure at the pressure sensor .....	101

## LIST OF ABBREVIATIONS

### ABBREVIATIONS

AoA	Angle of Attack
CFD	Computational Fluid Dynamics
DES	Detached Eddy Simulation
DDES	Delayed Detached Eddy Simulation
DNS	Direct Numerical Simulation
ER	Exact Riemann Solver
FF	Free Flight
FVM	Finite Volume Method
HPC	High Performance Computing
LE	Leading Edge
PDE	Partial Differential Equation
RANS	Reynolds-Averaged Navier-Stokes
ROE	Roe's Approximate Riemann Solver
SA	Spalart-Allmaras
SGS	Sub-Grid-Scale
SST	Shear Stress Transport
TE	Trailing Edge
TTCP	The Technical Cooperation Program

URANS	Unsteady Reynolds-Averaged Navier-Stokes
VLM	Vortex Lattice Method
WAF	Wrap-Around Fin

## LIST OF SYMBOLS

### SYMBOLS

CFL	CFL (Courant–Friedrichs–Lewy) Number
$C_{Fx}$	Axial Force Coefficient
$C_{Fy}$	Side Force Coefficient
$C_{Fz}$	Normal Force Coefficient
$C_{Mp}$	Roll Damping Coefficient
	Roll Moment Coefficient Change wrt Roll Rate ( $C_{Mxp}$ )
$C_{Mq}$	Pitch Damping Coefficient
	Pitching Moment Coefficient Change wrt Pitch Rate ( $C_{Myq}$ )
$C_{Mx}$	Roll Moment Coefficient
$C_{My}$	Pitching Moment Coefficient
$C_{M\alpha}$	Static Stability Coefficient
	Pitching Moment Coefficient Change wrt AoA ( $C_{My\alpha}$ )
$C_{M\dot{\alpha}}$	Dynamic Stability Coefficient
	Pitching Moment Coefficient Change wrt AoA Rate ( $C_{My\dot{\alpha}}$ )
$C_p$	Pressure Coefficient
CP	Center of Pressure
M	Mach Number
$N_r, N_\theta, N_z$	Number of Grid Points in Radial, Tangential, Spanwise Directions

$q(t)$	Pitch Rate
Re	Reynolds Number
St	Strouhal Number
$\alpha$	Angle of Attack (AoA)
$\dot{\alpha}(t)$	Angle of Attack Rate

# CHAPTER 1

## INTRODUCTION

The tube-launching missiles with wrap-around tail fins exhibit a packaging advantage as they do not require any volume allocation for the fins within the fuselage, a characteristic not shared by conventional missiles with planar fins. However, the asymmetric shape of wrap-around tails induces a roll moment even at neutral flight angles. Additionally, the amplitude and physical distribution of shed vortices over the wrap-around tails are influenced differently by body blockage and flow separation phenomena under non-zero flight angle of attack conditions. Due to these peculiarities, wrap-around tails are generally designed rigorously particularly in roll autopilot and trim conditions [1].

Although the induced roll moment is generally two orders of magnitude smaller than that of pitch and yaw moments, the smaller roll moment of inertia causes a larger angular acceleration in roll axis than the other two axes. Consequently, the roll autopilot and roll command must be designed to have more robust response times. Additionally, the roll autopilot must trim the induced roll moment for efficient laser guidance due to the fact that oscillatory roll motion prevents the laser beam stability.

### **1.1 Literature Review on Missiles with Wrap-Around Tail Fins**

Due to the roll moment induction with the packaging advantage of the Wrap-Around Fins (WAF) for missiles, there are experimental [1-10] and computational [11-15] studies, and analysis using aerodynamic/fligh dynamics simulation models [16-18], and design studies [8, 11, 19] on missiles with wrap-around tail fins in the literature, that are mostly available with some limited data, from early studies till

today as summarized in Table 1.1 and 1.2 as experimental and computational studies, respectively.

There are experimental studies about WAFs, both in wind tunnels and in free flight tests, and free flight model tests (aeroballistic range tests), in the late 1970s and 1980s for subsonic flow conditions and in 1990s for supersonic flow conditions as summarized in Table 1.1. Holmes [2] performed an experimental study to measure the surface pressure distribution on wrap-around tail fins of the standard The Technical Cooperation Program (TTCP) model missile to understand the roll induction mechanism. Dahlke and Flowers [1] extended this experimental study to measure the roll moment coefficient under different angles of attack and Mach numbers. Lucero [3] performed wind tunnel tests for comparing the performance of wrap-around fins and planar fins as control surfaces. Eastman and Wenndt [4] conducted wind tunnel tests on a slender maneuvering missile with four wrap-around tail fins at different Mach numbers, at angle of attack of  $30^\circ$  and at several roll angles and fin deflections. Predictions with the aerodynamic simulation models also compared well with the experiments and showing the differences between the WAFs and flat fins.

Winchenbach *et al.* [5] analyzed the dynamic instability by subsonic and supersonic free flight tests through which the trajectories are measured. They noted that the side moment has dynamic instability in supersonic flights. Abate and Winchenbach [6] analyzed the free flight test data for missile models with solid and slotted WAFs. They tried to have slots on wrap-around tail fins in order to decrease the roll induction without affecting the pitch stability. Vitale *et al.* [7] performed free flight model tests and investigated the shockwave patterns and turbulent bursts forming in the boundary layer for supersonic flight conditions, and made comparisons with CFD analyses.

Swenson *et al.* [8] performed a wind tunnel tests in order to understand aerodynamic effects of length to diameter ratio, fin sweep angles, fin thickness and Mach numbers. Tilmann *et al.* [9] analyzed the shock structure and the pressure distribution over the



wrap-around fins experimentally in wind tunnel tests at Mach number of 0.9 and by performing Euler CFD simulations. In a more recent experimental study, Mandic [10] performed wind tunnel tests for different missile configurations with wraparound fins and with flat fins to investigate rolling moment coefficients.

Table 1.1 Summary of Experimental Studies for Missiles with Wrap-Around Fins in Literature

<b>Author</b>	<b>Year</b>	<b>Experiment</b>	<b>Mach Number</b>
Holmes, J.E. [2]	1973	Wind Tunnel	0.3 – 1.3
Dahlke, C.W. and Flowers, L.D [1]	1974	Wind Tunnel	0.3 – 3.0
Lucero, E.F. [3]	1976	Wind Tunnel	0.65 – 0.98
Eastman, D.W. and Wenndt, D.L. [4]	1985	Wind Tunnel	0.6 – 1.8
Winchenbach, G.L., Buff, R.S., Whyte, R.H., and Hathaway, W.H. [5]	1986	Free Flight Tests	0.6 – 1.35
Abate, G.L. and Winchenbach, G.L. [6]	1991	Free Flight Model Tests	0.8 – 1.6
Vitale, R.E., Abate, G.L., Winchenbach, G.L., and Riner, W. [7]	1992	Free Flight Model Tests	2.75 – 5.15
Swenson, MW., Abate, G.L., and Whyte, R.H. [8]	1994	Free Flight Model Tests	1.03 – 2.96
Tilman C.P., Huffman R.E., Buter, T.A. and Bowersox, R.D.W. [9]	1997	Wind Tunnel	2.9
Mandic, S. [10]	2006	Wind Tunnel	0.5 – 0.8

In the early numerical studies as summarized in Table 1.2, Bar-Haim and Seginer [11] performed subsonic potential flow simulations for the standard TTCP missile model at zero angle of attack by using the Vortex Lattice Method (VLM) for the fins also with free wake models to investigate the mechanisms for the induced rolling moments due to wrap-around fins. Vitale *et al.* [7] performed free flight model tests and Euler simulations for missiles with WAFs and compared the results under supersonic conditions. They noted that an anomaly on the variation of pitch stability coefficient against Mach number occurs due to the subsonic leading edge flow which is accelerated into the supersonic regime. It causes asymmetric shockwave patterns for different freestream Mach numbers. Abate and Cook [12] performed Euler simulations for a range of subsonic and supersonic flow conditions for missile models with WAFs in order to understand the roll induction mechanism and roll reversal in supersonic regime. They used de Laval nozzle analogy to explain the roll induction and roll reversal phenomena for missiles with wrap-around tail fins.

In recent numerical studies, Kim *et al.* [13] investigated the behavior of roll characteristics for a standard rolling wrap-around fin missile model (TTCP model) under supersonic flow conditions with and without steady-state roll rate condition. The computational study was performed by solving 3-D Euler equations and the comparisons with the test data and comparisons for the roll damping moment coefficients were presented. Li *et al.* [14] performed a computational study to compare the missiles with wrap-around tail fins and conventional planar fins by RANS simulations for supersonic flight conditions. They found that there is no roll induction with planar fins and the normal force and pitch derivatives differ less than 1%.

Mikhail [15] used the available experimental data for the roll damping coefficients of missiles with wrap-around tail fins for different Mach numbers and cant angles for generating an algebraic correlation to model the roll damping coefficient in aerodynamic prediction codes. Tanrikulu and Mahmutyazicioglu [16, 17] analyzed the WAF aerodynamics at supersonic Mach numbers with a flight dynamics simulation model and discussed the effect of side moment coupled with

the magnus effect for missiles with wrap-around tail fins considering with the base cavity. Sharma and Kumar [18] reviewed the CFD analysis of WAFs in the literature and summarized the geometries, domain setup, grid generation, and results for WAF aerodynamics as a benchmark for future analysis and design studies.

Table 1.2 Summary of Computational Studies for Missiles with Wrap-Around Fins in Literature

<b>Author</b>	<b>Year</b>	<b>CFD Flow Solver</b>	<b>Mach Number</b>
Bar-Haim, B. and Seginer, A. [11]	1983	Potential Flow VLM Code	0.3 – 0.8
Vitale, R.E., Abate, G.L., Winchenbach, G.L., and Riner, W. [7]	1992	Euler Code EAGLE	2.75 – 5.15
Abate, G.L. and Cook, T. [12]	1993	Euler Code EAGLE	0.35 – 3.5
Kim, J.Y., Cho, S., and Lee, I. [13]	2012	Euler Code	1.3 – 3.0
Li, M., Abbas, L.K., and Rui, X. [14]	2015	RANS – $k-\omega$ SST Code	1.2 – 3.0

## 1.2 Literature Review on Computational Fluid Dynamics

Computational Fluid Dynamics is commonly used for generating aerodynamic database required in guidance, navigation and control systems of missiles [19-26]. This database contains six static aerodynamic coefficients for different combinations of altitude, Mach number, angle of attack, side slip angle and deflection angles. In the early stages of missile design, the aerodynamic database is utilized to develop a flight simulator before the first test launch. As the data processing rate of flight

computer is limited by the processor speed, the autopilot robustness and the missile maneuverability must be optimized as per the flight characteristics of each missile design. Therefore, the accuracy of aerodynamic coefficients generated by Computational Fluid Dynamics is of primary importance for guidance and autopilot subsystems.

The conservation equations of mass, momentum and energy are employed in CFD analyses for aerodynamic database generation. These equations are strongly coupled for compressible flows, necessitating the use of coupled solvers in finite volume method. In finite volume method, the domain is discretized into small cells, in each of which the cell averages of conserved quantities are changed by the net amount of flux divided by the cell volume.

The fluxes in the Navier-Stokes Equation can be classified as viscous and inviscid flux. In the absence of viscous effects, the Navier-Stokes equation transforms into the Euler equation, a nonlinear hyperbolic partial differential equation (PDE) in which all eigenvalues are real. Due to the nonlinearity in hyperbolic PDEs, there exist at least one or more genuinely nonlinear eigenmodes that can have strong or weak solutions [27-33]. Rohde [34] investigated the eigenmodes of Euler equations for general geometries for finite volume method applications.

The oscillations on the pressure fields arise due to the turbulent eddies energy cascade between different eddy sizes. Since it is computationally expensive to resolve all the turbulent eddies as in Direct Numerical Simulations (DNS) until the scale of Kolmogorov at which viscous dissipation comes into action to seize the energy transfer between cascades, different subgrid scale models such as Smagorinsky and Vreman SGS models are used in Large Eddy Simulations [35-37]. Although the required grid size for LES is larger than that of DNS, in the wall bounded problems the difference decreases sharply, increasing the computational cost of LES. For that reason, Spalart *et al.* [38-40] proposed a hybrid RANS-LES method based on the single equation turbulence model.

Wilcox proposed and developed two equation  $k-\omega$  turbulence model in which turbulent kinetic energy  $k$  and specific dissipation rate  $\omega$  are solved as per governing equations [41]. Menter combined the advantages of two popular turbulent models by a blending function that is determined by the closest distance the wall since free shear and wall bounded turbulence modelling requires different model parameters [42].

In finite volume method, the flux on the cell boundaries is calculated using the left and right hand side of the fluxes. Since the first order schemes are highly dissipative, second order accurate schemes are generally used. In order to obey the maximum principle and total variation diminishing conditions, the second order schemes are used with flux limiters. The flux limiter is an active research area in the computational fluid dynamics [43-48].

After performing the limiters, the flux on each cell interface can be calculated from the fluxes on the left and the right sides of the cell interface with a single discontinuity known as the Riemann problem. Due to the nonlinearity in Euler equations, the exact solution of the Riemann problem requires iterative techniques and wave identification to detect the weak solutions. In order to avoid the computational cost, there are many approximate Riemann solvers and alternative flux methods in the literature [49-62].

The most well known Riemann solvers are Roe's Approximate Riemann solver [49] that is explained in detail in the next Chapter. Liou *et al.* [50-53] developed Advection Upstream Splitting Method family for calculating the flux by splitting it as the velocity and pressure fluxes. Jameson *et al.* [54-57] developed a JST central scheme with artificial viscosity to avoid the Riemann problem and the limiters. In spite of the computational cost of exact Riemann solver, each approximate Riemann solver is tested on Sod's shock tube problem by comparing the result of exact Riemann solver [52]. For that reason, an in house exact Riemann solver is used to compare with an approximate Riemann solver in a real life CFD problem.

The errors of approximate Riemann solvers are particularly prominent in unsteady cases, low density flows and transonic cases [58-62]. Chiodaroli *et al.* [63] proved

that the admissible weak solutions exist in Euler equations with smooth initial data under subsonic flow conditions. As a consequence, the errors on the inviscid flux can significantly alter temporal and spatial nature of the pressure distribution over the missile surface. Given that the accuracy of the pressure distribution is of paramount importance in missile guidance, analyzing the differences between exact and approximate Riemann solvers has a practical interest for addressing further unsteady aerodynamic problems.

Palacios *et al.* [64] developed an open source CFD software package called SU2 that combines all different limiters, gradient techniques, turbulence models and flux schemes for unstructured grids by C++. There are many steady and unsteady validation studies on SU2 including internal and external flows [65-73]. For that reason, an in house developed Exact Riemann (ER) solver is added to the open source CFD code SU2 for comparing the difference with the built-in Roe's Approximate Riemann (ROE) solver in SU2.

### **1.3 Thesis Motivation and Objectives**

This thesis mainly investigates the aerodynamic characteristics of roll induction for missiles with wrap-around tail fins by performing steady-state RANS and unsteady DDES simulations at different Mach numbers and angles of attack. In order to better capture the features of the unsteady complex separated flows of wrap-around fins and for better prediction of the aerodynamic coefficients, especially the roll moment coefficient, an Exact Riemann (ER) solver is implemented and used and the comparisons with the Approximate Riemann (ROE) solver and with the available experimental data for four different test cases are done.

Four different experimental configurations are selected for the CFD simulations as shown in Table 1.3. The first case is the generic missile geometry that was tested in free flight under transonic flow conditions by Dupuis [74]. Although there was no unsteady data sampling, the same test was repeated for many cases for optimizing

the aerodynamic database for better flight trajectory estimation. For that reason, this case is selected to compare the differences between the Riemann solvers in steady-state and unsteady RANS simulations. The second case is the generic missile geometry with wrap-around tail fins that was tested under different Mach numbers in a wind tunnel test campaign by Dahlke and Flowers [1]. In order to clarify the aerodynamic roll moment induction at neutral flight angles, the CFD simulations are performed for this missile geometry. Additionally, the roll moment change with angle of attack at Mach number of 0.5 is also investigated RANS simulations. In order to indicate the differences between the Riemann solvers, the flow condition at Mach number of 0.5 and an angle of attack of  $10^\circ$  is used.

Due to the lack of unsteady experimental data in the literature for the missiles with WAFs, other unsteady test cases that are available for airfoils are selected. The third case is the NACA 0021 airfoil in deep stall case at an angle of attack of  $60^\circ$  which was studied in the wind tunnel tests performed by Swalwell *et al.* [75, 76]. Since for this flow condition at a high angle of attack, there are the nonlinearities and unsteady effects generated by shed vortices in the separated flow and the test data has the FFT spectrum of the lift coefficient, this test case is selected as one of the unsteady validation cases. This case is also used for code validation in many CFD studies in the literature [77-79]. The fourth case is the OAT 15A airfoil under transonic shock buffeting which has rapid and periodic changes in the pressure distribution due to an unsteady shockwave on the airfoil upper surface. Joacquin *et al.* [80] performed a set of wind tunnel experiments at an angle of attack range to illustrate the boundary of transonic buffeting by a pressure sensor located on the the airfoil surface. Due to the unsteady nature of the shockwaves, this case is selected for comparison and validation.

Table 1.1 Computational Test Cases

<b>TEST CASES</b>	<b>Flow Conditions</b>	<b>Steady-State / Unsteady CFD</b>
Missile with Basic Fins (Basic Finner Geometry [74])	High Subsonic Low AoA	RANS / URANS
Missile with WAFs (Dahlke Geometry [1])	High Subsonic Transonic Low AoA	RANS / DDES
NACA 0021 Airfoil [75]	Low Subsonic High AoA Deep Stall	- / DDES
OAT 15A Airfoil [80]	High Subsonic Low AoA Transonic Buffeting	RANS / URANS

#### 1.4 Thesis Outline

In this thesis, first in Chapter 1, an introduction about wrap-around fins is presented with the literature review on the computational and experimental studies about missiles and WAFs and the literature review on the numerical approaches in CFD simulations and especially the Riemann solvers are presented. Then, the thesis motivation and objectives are described, and the outline is presented.

In Chapter 2, the numerical methodology, governing equations, turbulence modeling, and exact and approximate Riemann solvers are described.

In Chapter 3, the computational test cases investigated in this thesis are presented with details of the geometry and grid generation and flow conditions.



In Chapter 4, the results of the CFD simulations performed for the missiles with wrap-around fins and with basic planar fins and the aerodynamic characteristics of WAFs are presented in detail.

In Chapter 5, the results of the CFD simulations for two airfoils at two different specific conditions, deep stall and transonic buffeting cases, are presented in detail as validation studies for the exact Riemann solver implemented in this thesis study.

Finally, in Chapter 6, the conclusions and future work suggestions are presented.



## CHAPTER 2

### NUMERICAL METHODOLOGIES

In the first part of this Chapter, the theoretical background is presented starting from scalar nonlinear hyperbolic partial differential equations to system of equations to define the structure of Euler equations of gas dynamics rigorously.

In the second part, the role of Euler equations in the Navier-Stokes equations is explained in order to stress its effect on the Computational Fluid Dynamics (CFD) analyses. In the third part, Reynolds-Averaged Navier-Stokes (RANS) is explained in terms of the Finite Volume Method (FVM) with Spalart-Allmaras (SA) turbulence model. In the fourth part, the concept of Large Eddy Simulation (LES) and hybrid RANS-LES methods based on Detached Eddy Simulation (DES) are explained with its emphasis over the flight stability and maneuverability of missiles.

#### 2.1 Nonlinear Hyperbolic Partial Differential Equations

Hyperbolic partial differential equations (PDE) are unidirectional depending on the direction of eigenvalues in physical space unlike elliptic and parabolic PDEs. Therefore, a PDE system can be called hyperbolic if and only if the jacobian matrix  $A$  is diagonalizable with real eigenvalues for all real coefficients as shown in Equations 1 - 3.

$$\vec{u} = (u_1, \dots, u_s), \quad \vec{u} = \vec{u}(\vec{x}, t), \quad \vec{x} \in \mathbb{R}^d, \quad \frac{\partial \vec{u}}{\partial t} + \sum_{j=1}^d \frac{\partial}{\partial x_j} \vec{f}^j(\vec{u}) = 0, \quad (1)$$

$$A^j := \begin{bmatrix} \frac{\partial f_1^j}{\partial u_1} & \dots & \frac{\partial f_1^j}{\partial u_s} \\ \vdots & \ddots & \vdots \\ \frac{\partial f_s^j}{\partial u_1} & \dots & \frac{\partial f_s^j}{\partial u_s} \end{bmatrix}, \quad \text{for } j = 1, \dots, d \quad (2)$$

$$\forall \alpha_j \in \mathbb{R}, \quad A := \alpha_1 A^1 + \dots + \alpha_d A^d \quad (3)$$

The linearity or nonlinearity of hyperbolic equations is determined by the variation of an eigenvalue,  $\lambda_i$ , along the corresponding eigenvector,  $\omega_i$ , direction in the state space as shown in Equation 4.

$$\nabla_{\vec{u}} \lambda_i = \left[ \frac{\partial \lambda_i}{\partial u_1} \dots \frac{\partial \lambda_i}{\partial u_s} \right] \quad (4)$$

$$\begin{aligned} \nabla_{\vec{u}} \lambda_i^T \cdot \omega_i &\neq 0 \text{ Genuine Nonlinearity} \\ \nabla_{\vec{u}} \lambda_i^T \cdot \omega_i &= 0 \text{ Linear Degeneracy} \end{aligned} \quad (5)$$

It is clear that  $\nabla_{\vec{u}} \lambda_i$  is the gradient vector of eigenvalue  $\lambda_i$  over the conserved vector  $\vec{u}$ . Its dot product by the corresponding eigenvector,  $\omega_i$ , shows the variation of the eigenvalue in the eigenvector direction. Genuinely nonlinear eigenvalues are the source of nonlinearity whereas linearly degenerate eigenvalues are not the source of nonlinearities but they may affect genuinely nonlinear eigenvectors if they exist in the system of equations. If all the eigenvalues in the system of equations are linearly degenerate, which means that there is no genuinely nonlinear eigenvalues in the system of equations, the set of equations can be called linear hyperbolic equations.

### 2.1.1 Scalar Nonlinear Hyperbolic Equations

Inviscid Burgers equation, as nonlinear hyperbolic scalar PDE, is shown in conservative form as in Equation 6.

$$\frac{\partial u}{\partial t} + \frac{\partial f}{\partial x} = 0, \quad f = \frac{u^2}{2} \quad (6)$$

If this equation is written in non conservative form, the Jacobian matrix has only one left and right eigenvector  $\omega = [1]$  and the eigenvalue is  $\lambda = u$  with a diagonalizable property as shown in Equation 7 - 9.

$$\frac{\partial u}{\partial t} + u \frac{\partial u}{\partial x} = 0 \quad (7)$$

$$A = P^{-1} \Lambda P = [1][u][1] \quad (8)$$

$$\nabla_{\vec{u}} \lambda_i^T \cdot \omega_i = \left[ \frac{\partial u}{\partial u} \right] \cdot [1] = 1 \neq 0 \quad (9)$$

It is clear that the scalar product of the gradient of eigenvalue and the corresponding eigenvector is equal to 1 which is nonzero that is the clear proof of nonlinearity. The type of solution for nonlinear eigenmodes in hyperbolic equations cannot be restricted in a continuous form. For that reason, the nonconservative form in Equation 7 that is based on the assumption that  $u$  is a continuous function is not valid in the computational domain.

It is called the weak solution that satisfies Equation 6 yet it is not continuously differentiable. In order to find the discontinuous solution, the nonconservative form of the equation should be rewritten in the integral form as in Equation 10.

$$\frac{\partial}{\partial t} \int_{x_1}^{x_2} u dx = -f(u) \Big|_{x_1}^{x_2} \quad (10)$$

If a discontinuity is assumed to exist in a position  $x_s(t) \in [x_1, x_2]$ , the left hand side of Equation 10 can be rewritten as in Equation 11 and 12 in order to take the time derivative inside the integral because the function  $u$  has no derivative in the discontinuity position  $x_s(t)$ .

$$\frac{\partial}{\partial t} \left[ \int_{x_1}^{x_s(t)} u dx + \int_{x_s(t)}^{x_2} u dx \right] = -f(u) \Big|_{x_1}^{x_2} \quad (11)$$

$$\int_{x_1}^{x_s(t)} \frac{\partial u}{\partial t} dx + \int_{x_s(t)}^{x_2} \frac{\partial u}{\partial t} dx + u^- \frac{dx_s}{dt} - u^+ \frac{dx_s}{dt} = -f(u) \Big|_{x_1}^{x_2} \quad (12)$$

In Equation 12,  $-$  and  $+$  superscripts indicate the value of variable  $u$  in the upstream and downstream on the boundaries of the discontinuity, respectively, as shown in Figure 2.1.

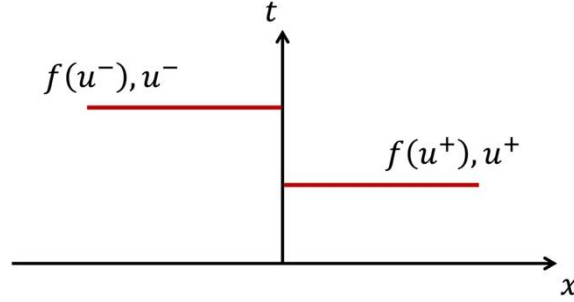


Figure 2.1: The boundary values of conserved variable  $u$  and flux function  $f$  at a discontinuity

If the boundary  $[x_1, x_2]$  is shrunk until the boundary of the discontinuity, the Rankine-Hugoniot jump condition must be satisfied as shown in Equation 13.

$$s = \frac{dx_s}{dt} = \frac{f(u^-) - f(u^+)}{u^- - u^+} \quad (13)$$

There are many different weak solutions can be obtained in hyperbolic nonlinear scalar PDE's. However, the type of solution must be unique to satisfy uniqueness of the solution. Since the direction of the wave is restricted in the hyperbolic equations, the weak solution appears when the characteristics of the waves intersects. It requires the Lax entropy condition to be satisfied for weak solutions as shown in Equation 14.

$$f'(u^-) > s > f'(u^+) \quad (14)$$

This condition states that the form of a discontinuity is possible if and only if the derivative of flux function with respect to the conserved quantity decreases i.e. the conflict of characteristics appear in the domain.

### 2.1.2 Euler Equations

Euler equations are well known nonlinear hyperbolic set of PDE that govern the mass, momentum and energy conservation as shown in Equation 15-18 for one dimensional case under the ideal gas assumption.

$$\frac{\partial \vec{Q}}{\partial t} + \frac{\partial \vec{F}}{\partial x} = 0 \quad (15)$$

$$\vec{Q} = \begin{bmatrix} \rho \\ \rho u \\ \rho e_o \end{bmatrix}, \quad \vec{F} = u \begin{bmatrix} \rho \\ \rho u \\ \rho e_o \end{bmatrix} + P \begin{bmatrix} 0 \\ 1 \\ u \end{bmatrix} \quad (16)$$

$$e_o = \frac{a^2}{\gamma(\gamma - 1)} + e_k, \quad h_o = \frac{a^2}{(\gamma - 1)} + e_k \quad (17)$$

$$a^2 = \gamma RT, \quad \gamma = \frac{c_p}{c_v}, \quad e_k = \frac{1}{2}u^2, \quad P = \frac{\rho a^2}{\gamma} \quad (18)$$

If the Jacobian matrix is calculated by taking the derivative of flux vector elements with respect to the conserved vector elements, it is straightforward to prove that there are only real eigenvalues with three independent eigenvectors as shown in Equation 19-21.

$$\bar{A} = \begin{bmatrix} 0 & 1 & 0 \\ (\gamma - 3)e_k & (3 - \gamma)u & \gamma - 1 \\ u[(\gamma - 1)e_k - h_o] & h_o - (\gamma - 1)u^2 & \gamma u \end{bmatrix} \quad (19)$$

$$R = [\vec{R}_1 \vec{R}_2 \vec{R}_3] = \begin{bmatrix} 1 & 1 & 1 \\ u - a & u & u + a \\ h_o - ua & \frac{u^2}{2} & h_o + ua \end{bmatrix} \quad (20)$$

$$\lambda = [u - a, \quad u, \quad u + a] \quad (21)$$

If the gradients of the eigenvalues are taken with respect to the elements of conserved vector  $\vec{Q}$ , the classification of eigenvectors can be performed with respect to the rule given in Equation 5. As shown in Equation 22, the eigenvalues of  $u - a$  and  $u + a$  that are called acoustic eigenmodes are genuinely nonlinear whereas the eigenvalue

of  $u$  that is called the contact discontinuity is linearly degenerate as shown in Equation 22-23.

$$\nabla_{\vec{Q}} u \pm \nabla_{\vec{Q}} a = \frac{1}{\rho} \begin{bmatrix} -u \\ 1 \\ 0 \end{bmatrix} \pm \frac{\gamma(\gamma-1)}{2\rho a} \begin{bmatrix} -c_v T + \frac{u^2}{2} \\ -u \\ 1 \end{bmatrix} \quad (22)$$

$$\nabla_{\vec{Q}} \lambda_i^T \cdot \vec{R}_i = \left[ -\frac{a}{2\rho}(\gamma+1), \quad 0, \quad \frac{a}{2\rho}(\gamma+1) \right] \quad (23)$$

### 2.1.3 Finite Volume Method

When Euler equations are extended into three dimensional case, two extra equations are involved in the set of equations to conserve momentum in other two dimensions. Semi discretized form of the equations are used in order to obtain a single flux vector in Finite Volume Method as shown in Equations 24-25:

$$\frac{\partial}{\partial t} \int_{\Omega} \vec{Q} dV + \oint_{\partial\Omega} \vec{F} dA = 0 \quad (24)$$

$$\frac{\partial}{\partial t} \int_{\Omega} \vec{Q} dV + \sum_j \vec{F} \cdot \vec{n}_{ij} A_{ij} = 0 \quad (25)$$

The normalized flux vector  $\vec{F} \cdot \vec{n}_{ij}$  and conserved quantity vector  $\vec{Q}$  are as shown in Equation 26-29. The normalization of the flux is obtained by decomposing the inviscid flux as convective and pressure flux terms by multiplying by the cell face normal unit vector as shown in Equation 26:

$$\vec{Q} = \begin{bmatrix} \rho \\ \rho u \\ \rho v \\ \rho w \\ \rho e_o \end{bmatrix}, \quad \vec{F} = V_n \begin{bmatrix} \rho \\ \rho u \\ \rho v \\ \rho w \\ \rho e_o \end{bmatrix} + P \begin{bmatrix} 0 \\ n_x \\ n_y \\ n_z \\ V_n \end{bmatrix} \quad (26)$$

$$V_n = \vec{V} \cdot \vec{n} = un_x + vn_y + wn_z \quad (27)$$



$$n_x^2 + n_y^2 + n_z^2 = 1 \quad (28)$$

$$a^2 = \gamma RT, \quad \gamma = \frac{c_p}{c_v}, \quad e_k = \frac{1}{2}(u^2 + v^2 + w^2), \quad P = \frac{\rho a^2}{\gamma} \quad (29)$$

If the Jacobian matrix is calculated by taking the derivative of flux vector elements with respect to the conserved vector elements, the Jacobian matrix, its eigenvalues and eigenvectors are shown in Equation 30-32.  $V_n - a$  and  $V_n + a$  are acoustic eigenmodes that are genuinely nonlinear whereas repeated eigenvalues of  $V_n$ 's are linearly degenerate composing of one contact discontinuity and two vorticity waves.

$$\bar{j} = \begin{bmatrix} 0 & n_x & n_y & n_z & 0 \\ (\gamma - 1)e_k n_x - uV_n & V_n - (\gamma - 2)un_x & un_y - (\gamma - 1)vn_x & un_z - (\gamma - 1)wn_x & (\gamma - 1)n_x \\ (\gamma - 1)e_k n_y - vV_n & vn_x - (\gamma - 1)un_y & V_n - (\gamma - 2)vn_y & vn_z - (\gamma - 1)wn_y & (\gamma - 1)n_y \\ (\gamma - 1)e_k n_z - wV_n & wn_x - (\gamma - 1)un_z & wn_y - (\gamma - 1)vn_z & V_n - (\gamma - 2)wn_z & (\gamma - 1)n_z \\ [(\gamma - 1)e_k - h_0]V_n & h_0 n_x - (\gamma - 1)uV_n & h_0 n_y - (\gamma - 1)vV_n & h_0 n_z - (\gamma - 1)wV_n & \gamma V_n \end{bmatrix} \quad (30)$$

$$\lambda_i = \{V_n - a, \quad V_n, \quad V_n + a, \quad V_n, \quad V_n\} \quad (31)$$

$$[\vec{R}_1 \vec{R}_2 \vec{R}_3 \vec{R}_4 \vec{R}_5] = \begin{bmatrix} 1 & 1 & 1 & 0 & 0 \\ u - an_x & u & u + an_x & n_y & -n_z \\ v - an_y & v & v + an_y & -n_x & 0 \\ w - an_z & w & w + an_z & 0 & n_x \\ h_0 - aV_n & e_k & h_0 + aV_n & un_y - vn_x & wn_x - un_z \end{bmatrix} \quad (32)$$

The contact discontinuity  $\vec{R}_2$  does not change the velocity components and pressure but the density and temperature. In this case, ideal gas law dictates that under constant pressure the temperature must change like entropy. Vorticity waves  $\vec{R}_4$  and  $\vec{R}_5$  cannot change the density, pressure, temperature, and normal velocity component with respect to its direction but only the tangential velocity component to generate a variation in the vorticity along the wave characteristic direction. As linearly degenerate waves, vorticity waves and contact discontinuity (also known as entropy wave in other sources) have only one form of solution. Those waves can change the total enthalpy.

The acoustic eigenvalues  $\vec{R}_1$  and  $\vec{R}_3$  are the only genuinely nonlinear eigenvalues that alter the pressure in Euler equations. Those waves can have two different solutions as rarefaction waves and shockwaves. The rarefaction waves, as idiosyncrasy of nonlinear hyperbolic differential equations, are continuous and isentropic through which isentropic relations between pressure and density decrease isentropically and velocity decreases. The shockwaves are discontinuous through which normal velocity component decreases unlike pressure and density. The relative velocity based Rankine-Hugoniot conditions are applied in shockwaves [22-30]. Rarefaction waves are isentropic i.e., reversible and adiabatic for all thermal and chemical equilibrium conditions. The relative velocities with respect to shockwave speed must be taken into account for imposing Rankine-Hugoniot jump condition. The relative total enthalpy is conserved along a shockwave which means that the total enthalpy difference in the up and downstream of a shockwave is due to the temporal derivatives in total internal energy but not the shockwave. Therefore, the total enthalpy must be conserved in stationary shockwaves.

#### **2.1.4 Riemann Problem in Finite Volume Method**

Riemann problem is a kind of initial value problem that consists of a conservation equation with a single discontinuity in the solution domain as shown in Figure 2.2 for one dimensional Euler equations. In the context of the FVM, the Riemann problem refers to the problem of computing the flux across a cell interface between two neighboring cells in a discretized domain.

Once the velocity vector multiplied by dot product with the cell unit vector on neighboring sides, the problem becomes similar to the one dimensional Euler equations that contain two genuinely nonlinear fields with a single contact discontinuity.

The Riemann problem arises when computing the flux across the interface between two neighboring cells. At the interface, the solution may exhibit a contact

discontinuity, a shock wave or a rarefaction wave. To compute the flux, the state of the solution on either side of the interface must be identified. The Riemann problem is the problem of determining the state in the boundary from the initial conditions.

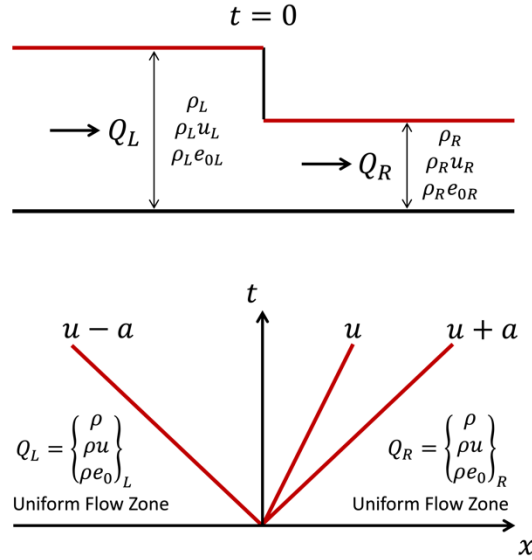


Figure 2.2: The Riemann Problem in 1D Euler Equations

### 2.1.5 Roe's Approximate Riemann Solver

Due to the nonlinear nature of Euler equations, the exact solution of Riemann problem needs iterative techniques that require more computational power. In order to avoid this requirement, Roe [49] developed an approximate Riemann solver that linearizes the problem by using an average technique proposed by Roe [49]. If an hyperbolic problem is linearized, it can be said that the difference between each wave must be a scalar multiple of the corresponding eigenvector as shown in Equations 49-53:

$$\bar{A}^- = P^{-1}\Lambda^-P, \quad \bar{A}^+ = P^{-1}\Lambda^+P \quad (49)$$

$$\Lambda^- = \sum_i^n \min(0, \lambda_i), \quad \Lambda^+ = \sum_i^n \max(0, \lambda_i) \quad (50)$$

$$\vec{F}_{wall} = \vec{F}_L + \bar{A}^-(\vec{Q}_R - \vec{Q}_L) \quad (51)$$

$$\vec{F}_{wall} = \vec{F}_R - \bar{A}^+ (\vec{Q}_R - \vec{Q}_L) \quad (52)$$

$$\vec{F}_{wall} = \frac{\vec{F}_L + \vec{F}_R}{2} - \frac{|\bar{A}|}{2} (\vec{Q}_R - \vec{Q}_L) \quad (53)$$

The question is to construct the linearized Jacobian matrix  $|\bar{A}|$  using average method of Roe. Roe chooses a parameter vector  $\vec{U}$  to take its average from left and right sides of the cell interface as shown in Equation 54. Since the density is not required to construct the Jacobian matrix, only the velocity components, total enthalpy and speed of sound are calculated as shown in Equations 55-56:

$$\vec{U} = \sqrt{\rho} \begin{bmatrix} 1 \\ u \\ v \\ w \\ h_o \end{bmatrix} \quad (54)$$

$$\tilde{u} = \frac{\sqrt{\rho_L} u_L + \sqrt{\rho_R} u_R}{\sqrt{\rho_L} + \sqrt{\rho_R}}, \tilde{v} = \frac{\sqrt{\rho_L} v_L + \sqrt{\rho_R} v_R}{\sqrt{\rho_L} + \sqrt{\rho_R}}, \tilde{w} = \frac{\sqrt{\rho_L} w_L + \sqrt{\rho_R} w_R}{\sqrt{\rho_L} + \sqrt{\rho_R}} \quad (55)$$

$$\tilde{H} = \frac{\sqrt{\rho_L} H_L + \sqrt{\rho_R} H_R}{\sqrt{\rho_L} + \sqrt{\rho_R}}, \tilde{\alpha} = \sqrt{(\gamma - 1) \left( \tilde{H} - \frac{1}{2} (\tilde{u}^2 + \tilde{v}^2 + \tilde{w}^2) \right)} \quad (56)$$

The other method is the central scheme with artificial viscosity instead of constructing a Jacobian Matrix. The need of artificial viscosity is due to the nonlinear nature of Euler equations. It is called artificial viscosity because the difference between neighboring faces is similar with a diffusive flux that includes viscosity as diffusion coefficient as shown in Equation 57 that is also known as Rusanov flux [60]:

$$\vec{F}_{wall} = \frac{\vec{F}_L + \vec{F}_R}{2} - \frac{|\lambda|_{max}}{2} (\vec{Q}_R - \vec{Q}_L) \quad (57)$$

The maximum eigenvalue of a matrix is called spectral radius since a vector can extend by scalar multiple of this eigenvalue when it is multiplied by that matrix. Although this technique preserves stability and hyperbolicity of the Jacobian matrix,

it is too dissipative since it covers the complete difference on conserved quantities. Jameson *et al.* [27] added extra parameters to the artificial viscosity besides maximum eigenvalue. Since the genuinely nonlinear eigenmodes are the only eigenmodes that can change the pressure, their strength can be determined by the local pressure difference.

### 2.1.6 Exact Riemann Solver

Alternative flux calculation schemes are in good accuracy for most of the flight regimes. However, their accuracy might have tendency to decrease if Mach number is very low to increase the condition number of the Jacobian matrix to make the scheme over diffusive or very close the transonic conditions in which linearization of Riemann problem fails [16].

In order to have an effective benchmark through which the accuracy levels can be illustrated, an iterative Exact Riemann (ER) solver is added to the open source CFD code SU2 [42]. Before solving the Riemann problem, the types of genuinely nonlinear waves must be determined.

Despite of the fact that the computationally expensive iterative techniques must be performed in exact Riemann solver, the determination of wave types has no such a high computational expense.

There are four different probabilities that are RR, RS, SR and SS where R and S stand for rarefaction and shock, respectively. The pressure has to increase and decrease in downstream of the shock and rarefaction, respectively. For that reason, the shock must exist in the low pressure side in one rarefaction one shock solution. Therefore there are three possibilities left. Therefore it is required to assign minimum and maximum pressure sides before the determination of wave types if  $p_L \neq p_R$  as shown in Figure 4.2 and Equation 58:

$$p_{min} = \min(p_L, p_R), \quad p_{max} = \max(p_L, p_R) \quad (58)$$

The pressure  $p^*$  on the cell face may be larger or smaller than both  $p_L$  and  $p_R$  or may be between  $p_L$  and  $p_R$  if  $p_L \neq p_R$ . In case of equality, there are three possibilities that are RR, SS or zero amplitude nonlinear waves i.e. isolated contact discontinuity.

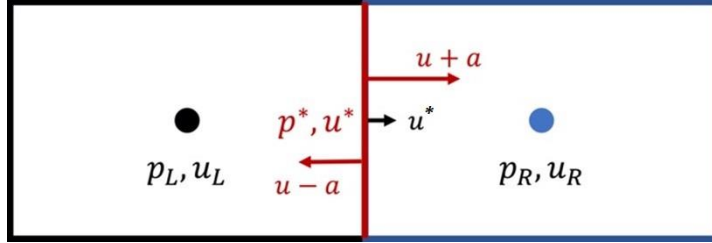


Figure 2.3: Riemann problem in finite volume method

In Figure 2.3, the directions of waves are shown in a subsonic flow with a positive velocity  $u^*$  on the cell interface in the direction of the unit normal vector. In order to determine the wave types, the governing equations on both sides of nonlinear waves must be used as shown in Equations 59-61:

$$u^* = u_L + \text{sign}(u - a) * f_L(p^*, \vec{U}_L) \quad (59)$$

$$u^* = u_R + \text{sign}(u + a) * f_R(p, \vec{U}_R)$$

$$0 = u_R - u_L + f_L(p^*, \vec{U}_L) + f_R(p^*, \vec{U}_R) \quad (60)$$

$$f(p^*, \vec{U}_{L,R}) = \begin{cases} (p^* - p_{L,R}) \left[ \frac{2}{\rho_{L,R} ((\gamma + 1)p^* + (\gamma - 1)p_{L,R})} \right]^{\frac{1}{2}}, & p_{L,R} < p^*(S) \\ \frac{2a_{L,R}}{\gamma - 1} \left[ \left( \frac{p^*}{p_{L,R}} \right)^{\frac{\gamma-1}{2\gamma}} - 1 \right], & p_{L,R} \geq p^*(R) \end{cases} \quad (61)$$

The Equation 59 must be satisfied for calorically perfect gases with constant specific heat ratio. The type of functions is derived from isentropic relations and Rankine-Hugoniot jump conditions for rarefaction and shock solutions, respectively [11, 23]. Both functions have positive first derivative and negative second derivative and they converge to a negative value when  $p^*$  is going to zero and to a positive value when  $p^*$  is going to plus infinity.

Due to this property, the type of genuinely nonlinear fields can be determined with respect to the algorithm given in Figure 4.3. First, the functions of  $f_L$  and  $f_R$  are constructed as two rarefaction solution. If the function  $F$  has a positive value when  $F(p_{max})$  is calculated, then there exist two rarefaction solutions. If it has a negative value and if  $p_L = p_R$ , then there exists a two shock solution. If it has a zero value and if  $p_L = p_R$ , then there exists zero amplitude i.e. isolated discontinuity. If it has a negative value and if  $p_L \neq p_R$ , then the side with minimum pressure has a shock solution. In the second step, the function  $F$  is constructed with a shock solution on minimum pressure side and a rarefaction solution on maximum pressure side. If the function  $F$  has a positive value when  $F(p_{max})$  is calculated, then there exists one rarefaction on shock solution. If it has a negative value, then there exist two shock solutions as shown in Figure 2.4.

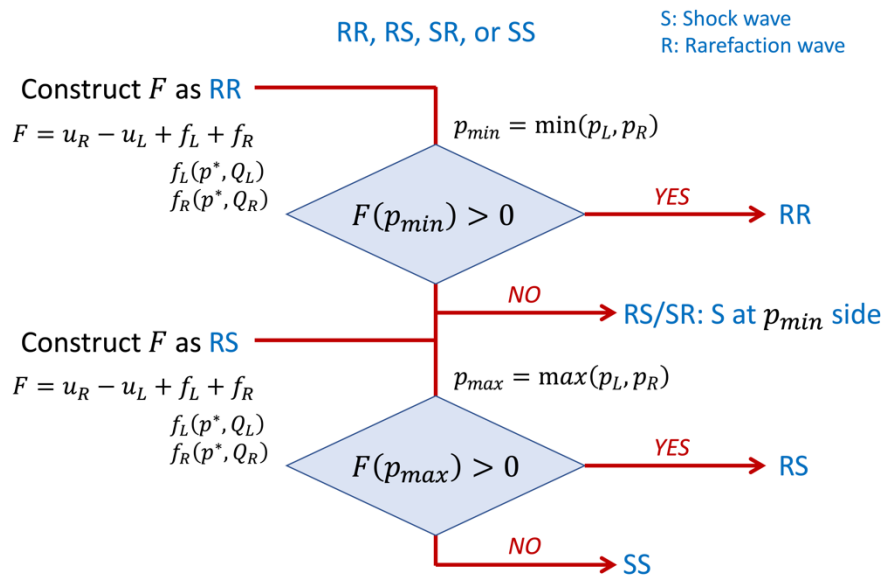


Figure 2.4: Exact Riemann solver shock capturing algorithm

Once the type of the nonlinear waves is identified, then the root of function  $F$  must be found for finding  $p^*$  that is the pressure on the interface and exact solution of the Riemann problem. Newton-Raphson algorithm is used for root finding since the function  $F$  has a monotonicity and for that reason Newton-Raphson is faster than bisection method as shown in Equation 62:

$$P_{k+1}^* = P_k^* - \frac{f(P_k^*)}{\frac{\partial f(P_k^*)}{\partial P^*}} \quad (62)$$

Since two rarefaction has an analytical solution unlike shock including solution, two rarefaction solution is used as an initial guess to find the root in Newton-Raphson algorithm. Once  $p^*$  is calculated,  $\rho^*$  and  $u^*$  can be calculated by using isentropic or Rankine Hugoniot relations depending on the type of the solution. Depending on the sign of  $u^*$ , the tangential velocity component can be added into solution from the side of tangential velocity with the same sign of nonlinear wave in the Finite Volume Method. The function is added into SU2 C++ structure as a new function under the convection subfolder in the flow folder.

As stopping criteria, `EXACT_RIEMANN_MAX_ITER` and `EXACT_RIEMANN_SOLVER_ERROR` parameters are added into the `cconfig` file under the common folder. Maximum iteration and solver error are fixed as 100 and  $1e-7$  by default, respectively. All CFD simulations are performed by those settings unless otherwise specified.

## 2.2 Compressible Navier-Stokes Equations

Euler equations of gas dynamics can be obtained from Navier-Stokes equations with absence of viscosity, thermal conductivity and viscous heat dissipation as shown in Equations 33-37:

$$\frac{\partial \vec{Q}}{\partial t} + \nabla \cdot \bar{\bar{F}}_{inv} - \nabla \cdot \bar{\bar{F}}_{vis} = 0 \quad (33)$$

$$\bar{\bar{F}}_{inv} = \begin{bmatrix} \rho u & \rho v & \rho w \\ \rho u^2 + p & \rho v u & \rho w u \\ \rho u v & \rho v^2 + p & \rho w v \\ \rho u w & \rho v w & \rho w^2 + p \\ u p + u e_o & v p + v e_o & w p + w e_o \end{bmatrix} \quad (34)$$



$$\vec{V} = \begin{bmatrix} u \\ v \\ w \end{bmatrix}, \quad \nabla\vec{V} = \begin{bmatrix} \frac{\partial u}{\partial x} & \frac{\partial u}{\partial y} & \frac{\partial u}{\partial z} \\ \frac{\partial v}{\partial x} & \frac{\partial v}{\partial y} & \frac{\partial v}{\partial z} \\ \frac{\partial w}{\partial x} & \frac{\partial w}{\partial y} & \frac{\partial w}{\partial z} \end{bmatrix} \quad (35)$$

$$\bar{\tau} = \mu(\nabla\vec{V} + \nabla\vec{V}^T) - \mu\frac{2}{3}\bar{I}(\nabla\cdot\vec{V}) = \mu \begin{bmatrix} \frac{4}{3}\frac{\partial u}{\partial x} & \frac{\partial u}{\partial y} + \frac{\partial v}{\partial x} & \frac{\partial u}{\partial z} + \frac{\partial w}{\partial x} \\ \frac{\partial v}{\partial x} + \frac{\partial u}{\partial y} & \frac{4}{3}\frac{\partial v}{\partial y} & \frac{\partial v}{\partial z} + \frac{\partial w}{\partial y} \\ \frac{\partial w}{\partial x} + \frac{\partial u}{\partial z} & \frac{\partial w}{\partial y} + \frac{\partial v}{\partial z} & \frac{4}{3}\frac{\partial w}{\partial z} \end{bmatrix} \quad (36)$$

$$\bar{F}_{vis} = \begin{bmatrix} 0 \\ \bar{\tau} \\ \bar{\tau} \cdot \vec{V} + k\nabla T \end{bmatrix} \quad (37)$$

The summation of velocity gradient and its transpose  $\nabla\vec{V} + \nabla\vec{V}^T$  is the rate of strain tensor of rank 2. Its multiplication by the dynamic viscosity is equal to crude shear tensor due to the linearity between stress and strain for Newtonian fluids such as air and water. The subtracted term  $\mu\frac{2}{3}\bar{I}(\nabla\cdot\vec{V})$  is stress contribution due to the rapid expansion or compression in the fluid due to the difference between mechanical and thermodynamic pressures. The shear stress tensor  $\bar{\tau}$  is a rank 2 tensor that is the mathematical notation of the shape deformation on the fluid element.

The dot product of shear stress by the velocity vector  $\bar{\tau} \cdot \vec{V}$  is the viscous heat dissipation mechanism that increases the internal energy of a gas by converting mechanical energy into the heat energy. In turbulence, the turbulent eddies transfer their energy to the smaller eddies until the viscous heat dissipation prevents energy transfer to smaller eddies at Kolmogorov scale. The multiplication of thermal gradient by thermal conductivity of a gas  $k\nabla T$  is the heat transfer by conduction due to Fourier's law of conduction.

### 2.3 Reynolds-Averaged Navier-Stokes Equations

Reynolds-Averaged Navier-Stokes (RANS) equations are obtained when the quantities are decomposed into time averaged and fluctuating components by Reynolds decomposition in nonconservative form of the Navier-Stokes equations as shown in Equations 37 and 38:

$$u(\vec{x}, t) = u' + \bar{u} \quad (37)$$

$$\rho \bar{u}_j \frac{\partial(\bar{u}_i)}{\partial x_j} = \frac{\partial}{\partial x_j} \left( -\bar{p} \delta_{ij} + \mu_d \left( \frac{\partial \bar{u}_i}{\partial x_j} + \frac{\partial \bar{u}_j}{\partial x_i} - \frac{2}{3} \frac{\partial \bar{u}_j}{\partial x_j} \delta_{ij} \right) - \rho \overline{u'_i u'_j} \right) \quad (38)$$

Due to the fact that the energy transfer between different eddy sizes cannot take place simultaneously at all times, the fluctuating term in the velocity field appears due to the turbulence. Since the turbulent eddy dissipation cannot take place until Kolmogorov scale that is too small for computational resolution, turbulence models are used to include the effect of  $\rho \overline{u'_i u'_j}$  by time average rate of strain and turbulent viscosity as shown in Equations 39-41:

$$-\rho \overline{u'_i u'_j} = \mu_t \left( \frac{\partial \bar{u}_i}{\partial x_j} + \frac{\partial \bar{u}_j}{\partial x_i} \right) \quad (39)$$

$$\mu_{eff} = \mu_t + \mu_d \quad (40)$$

$$\rho \bar{u}_j \frac{\partial(\bar{u}_i)}{\partial x_j} = \frac{\partial}{\partial x_j} \left( -\bar{p} \delta_{ij} + \mu_{eff} \left( \frac{\partial \bar{u}_i}{\partial x_j} + \frac{\partial \bar{u}_j}{\partial x_i} - \frac{2}{3} \frac{\partial \bar{u}_j}{\partial x_j} \delta_{ij} \right) \right) \quad (41)$$

The turbulence occurs due to the fracture of a fluid element under large momentum flux-shear stress ratio that is known as Reynolds number as shown in Equation 42:

$$Re = \frac{\rho V D}{\mu} = \frac{\rho V^2 D}{\mu V} = \frac{\rho V^2}{\mu \frac{V}{D}} \quad (42)$$

If a fluid element is exposed to an increasing shear force, it undergoes a fracture after certain Reynolds number depending on the problem. After the fracture, two opposing

vortices are formed inside the flow field. Due to the vortex stretching, they transfer their energy to smaller eddies until their energy is dissipated by the viscous heat dissipation i.e. triggering mechanism of the turbulence.

Turbulence models aim to model turbulent viscosity by time average rate of shear stress. However, the unsteady effects in a fluid problem does not necessarily occur due to the turbulence but the nature of the hyperbolic PDE's that might generate unsteady effects due to an imbalance between different eigenmodes due to the boundary conditions of a fluid problem. For that reason, Unsteady Reynolds-Averaged Navier-Stokes (URANS) Equations are used as shown in Equation 43:

$$\frac{\partial(\bar{u}_i)}{\partial t} + \rho \bar{u}_j \frac{\partial(\bar{u}_i)}{\partial x_j} = \frac{\partial}{\partial x_j} \left( -\bar{p} \delta_{ij} + \mu_{eff} \left( \frac{\partial \bar{u}_i}{\partial x_j} + \frac{\partial \bar{u}_j}{\partial x_i} - \frac{2}{3} \frac{\partial \bar{u}_j}{\partial x_j} \delta_{ij} \right) \right) \quad (43)$$

URANS models aim to model all the velocity fluctuations in a given time interval by eddy viscosity and time rate of strain by average velocity gradients. If the grid density is enough to resolve very large eddies in the domain, they are also modeled by the eddy viscosity terms. In order to avoid this effect, eddy viscosity should be modelled by sub grid scale (SGS) models instead of RANS based models i.e. Large Eddy Simulation (LES) [31, 69]. Smagorinsky [81] proposed a SGS model by assuming that turbulent energy production and dissipation are in equilibrium for small scales in SGS as shown in Equation 44:

$$\mu_{eddy} = C \rho \Delta^2 |\bar{S}|, \quad |\bar{S}| = \sqrt{tr(\nabla \vec{V} + \nabla \vec{V}^T)^2} \quad (44)$$

This model is used by Deardorff [82] in first LES simulation. Since the eddies close to the walls are very small for wall bounded problems, hybrid RANS-LES models are used in many industrial problems.

## 2.4 Detached Eddy Simulation with Spalart-Allmaras Model

The fluctuating component of the velocity field might cause flight instabilities by affecting the aerodynamic coefficients if the dimensionalized untrimmed moments have large amplitude and small frequency. As the moment inertiae of a missile increase, the amplitudes of untrimmed moments decrease due to low pass filter behaviour of inertia matrix. However, the untrimmed moments that have small frequency and large amplitude must be trimmed by autopilots with smaller gains. If the gains are overdecreased, over robust autopilot algorithms decrease the maneuverability of the missile. Therefore, an optimization must be performed through a tradeoff between flight stability and maneuverability.

In order to determine the gain matrices of autopilot algorithms, it is required to collect real time data by free flights, wind tunnels or time dependent CFD analyses. The oscillations on the pressure field occur due to the energy transfer between different turbulent eddy sizes. The full resolution of eddies until the Kolmogorov scale is not realistic for two reasons. The first reason is that the computational cost is not realistic for state of the art computational infrastructure. The second reason is that the critical eddy sizes and frequencies are function of inertia matrix for flight stability. In other words, there is no reason to resolve eddies under a critical frequency that is determined by the flight Mach number and missile inertia matrix.

In wall bounded flows, eddies close to the wall do not have an impact on the flight stability since their size and frequency are very small and large, respectively. For that reason, DDES (Delayed Detached Eddy Simulation) technique that is based on Spalart-Allmaras turbulence model is used in this thesis.

In Spalart-Allmaras turbulence model, eddy viscosity is calculated from the conserved quantity  $\tilde{\nu}$  as shown in Equation 45:

$$\begin{aligned} \frac{D\tilde{v}}{Dt} = & C_{b1}[1 - f_{t2}]\tilde{S}\tilde{v} + \frac{1}{\sigma}\{\nabla \cdot [(\nu + \tilde{v})\nabla\tilde{v}] + C_{b2}|\nabla\tilde{v}|^2\} \\ & - \left[ C_{w1}f_w - \frac{C_{b1}}{\kappa^2}f_{t2} \right] \left( \frac{\tilde{v}}{\tilde{d}} \right)^2 + f_{t1}\Delta U^2 \end{aligned} \quad (45)$$

Left hand side of the equation that is the Lagrangian derivative of  $\tilde{v}$  must be in equilibrium with source, destruction and diffusion terms. The last source term  $f_{t1}\Delta U^2$  is responsible for the transition from laminar to turbulent inside the boundary layer. The details of the coefficients can be found in the works of Spalart *et al.* [20-22]. In isotropic turbulence, the right hand of the equation must be equal to zero i.e. an equilibrium must be established between the source  $C_{b1}[1 - f_{t2}]\tilde{S}\tilde{v}$  and destruction  $\left[ C_{w1}f_w - \frac{C_{b1}}{\kappa^2}f_{t2} \right] \left( \frac{\tilde{v}}{\tilde{d}} \right)^2$  terms because the diffusive term must be equal to zero every point in the domain. Apart from their coefficients, an equilibrium between the source and sink terms dictates that  $\tilde{v}$  is proportional with the multiplication of rate of strain by the square of distance as shown in Equation 46:

$$\tilde{v} = \tilde{S}d^2 \quad (46)$$

The term  $d$  in the destruction term is the closest distance to a wall in the domain in the Spalart-Allmaras model. This distance is changed in Detached Eddy Simulation by  $\tilde{d}$  as per the formula given in Equation 47:

$$\tilde{d} = \min(d, C_{DES}\Delta), \quad \Delta = \max(\Delta S) \quad (47)$$

The idea is to increase the magnitude of the destruction term in the model so that the destruction term increases to suppress  $\tilde{v}$  for resolving the large eddies. For the cells close to walls inside the boundary layer in a grid the distance  $d$  is smaller than the largest edge of the cell. For that reason, the destruction term is constructed according to the Equation 45. It provides a smooth transition from RANS to LES in the domain. However, this transition might cause grid induced separation if the increment rate between the last element of viscous layer and outer grid. For that reason, Spalart proposed a Delayed Detached Eddy Simulation (DDES) in which the transition

function is not only function of the grid but also the length scale of the turbulence in associated cells as shown in Equation 48:

$$\tilde{d} = d - f_d \max(0, d - C_{DES}\Delta), f_d = 1 - \tanh(8r_d)^3 \quad r_d = \frac{\nu + \nu_t}{\sqrt{U_{ij}U_{ij}}k^2 d^2} \quad (48)$$

Since tanh function can vary between 0 and 1 for positive inputs, there is a smooth transition from RANS to LES as  $r_d$  changes from zero to infinity.

## 2.5 Dynamic Aerodynamic Coefficients

During tactical maneuvers or under oscillatory atmospheric conditions, missiles are exposed to varying forces and moments under time rate of change in flight parameters such as velocity, angle of attack or side slip angle. Dynamic aerodynamic coefficients determine how the missile corresponds to those changes in flight parameters. For this reason, it is of primary importance to determine flight trajectory. The most important dynamic stability derivatives are pitch damping coefficient ( $C_{M\dot{\gamma}}$ ), dynamic stability coefficient ( $C_{M\dot{\alpha}}$ ), roll damping coefficient ( $C_{M\dot{\chi}}$ ), Magnus force and Magnus moment. These are used to analyze the missile flight stability as it undergoes complex motions.

### 2.5.1 Pitch Damping Coefficient and Dynamic Stability

The calculation of pitch damping and dynamic stability derivative require two different unsteady CFD simulations for pitching and plunging motions [83-87]. It is due to the fact that the pitching motion around the center of gravity of projectile is coupled by the variation of angle attack. However, there is no pitching maneuver in the plunging motion as shown in Figure 2.5.

In order to calculate the pitch damping coefficient and the dynamic stability derivatives, the missile is exposed to a forced oscillation as shown in Equation 63 and 64, respectively:

$$\alpha(t) = \alpha_0 + \alpha_{amp} \sin \omega t \quad (63)$$

$$x(t) = x_{amp} \sin \omega t \quad (64)$$

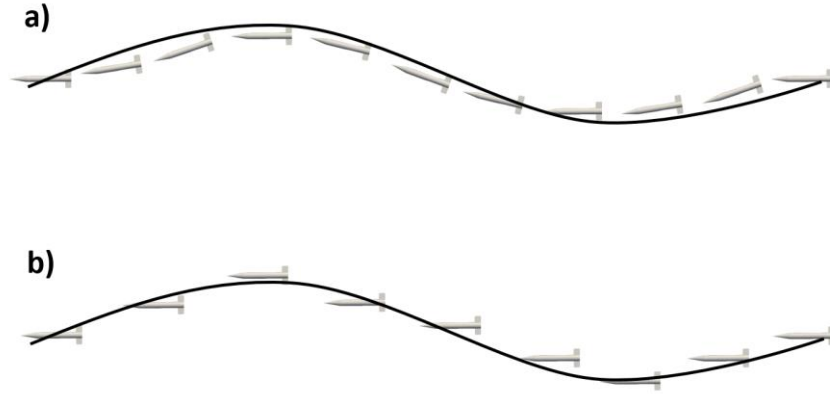


Figure 2.5: a) Pitching and b) Plunging Motion of a Missile

The analyses are performed around  $\alpha_0$  with an amplitude of  $1^\circ$  angle of attack in the pitching motion. The oscillation amplitude in the plunging motion, therefore, must be selected to have the same angle of attack range with the pitching motion for more precise calculation as shown in Equations 65-67:

$$\dot{x}(t) = x_{amp} \omega \cos \omega t \quad (65)$$

$$\alpha(t) = \tan^{-1} \frac{x_{amp} \omega \cos \omega t}{V_\infty} \quad (66)$$

$$x_{amp} = \frac{V_\infty \tan \alpha_0}{\omega} \quad (67)$$

$$k = \frac{\omega D}{2V_\infty} \quad (68)$$

The determination of oscillation frequency is performed by the nondimensionalized reduced frequency as shown in Equation 68. Despeyroux *et al.* [73] proposed to have a reduced frequency of 0.05 for numerically calculated dynamic stability of missiles with grid fin. Sahu *et al.* [74] used different values of reduced frequencies for

showing the effect of reduced frequency on the damping coefficients. The reduced frequency should be both large enough to distinct any numerical error and small enough to conserve the flight regime at each instant of the flight.

The equilibrium equation for pure pitching motion under the assumption of first order Taylor series expansion is as shown in Equation 69 [32]:

$$C_j(t) = C_j|_{0^\circ} + C_{j_\alpha} \alpha(t) + C_{j_q} \frac{q(t)D}{2V_\infty} + C_{j_{\dot{\alpha}}} \frac{\dot{\alpha}(t)D}{2V_\infty}, \quad j = M_y, F_z \quad (69)$$

where,  $C_j|_{0^\circ}$  and  $C_{j_\alpha}$  are the coefficient at angle of attack of  $0^\circ$  and static derivative with respect to angle of attack, respectively.

Since there is no plunging term in the forced pitching motion, the pitch rate  $q(t)$  and angle of attack rate  $\dot{\alpha}(t)$  are equal to each other. Pitch damping coefficient can be assumed constant for small amplitude oscillations [33, 34]. Once the integral of Equation 69 is taken with respect to  $\alpha$  under these two assumptions, Equation 70 is obtained. If the limits of the integral are kept over one period of motion,  $C_j|_{0^\circ}$  and  $C_{j_\alpha}$  terms are cancelled since they are not time dependent coefficients as shown in Equation 71:

$$C_{j_q} + C_{j_{\dot{\alpha}}} = \frac{2V_\infty \int [C_j(t) - C_j|_{0^\circ} - C_{j_\alpha} \alpha(t)] d\alpha}{D \int \dot{\alpha}(t) d\alpha} \quad (70)$$

$$C_{j_q} + C_{j_{\dot{\alpha}}} = \frac{2V_\infty \int C_j(t) d\alpha}{D \int \dot{\alpha}(t) d\alpha} \quad (71)$$

If  $\dot{\alpha}(t)$  is calculated using Equation 63 and the integral is taken over a single period of time, the sum of dynamic derivative and pitch damping ratio is as shown in Equation 72.

$$C_{j_q} + C_{j_{\dot{\alpha}}} = \frac{2V_\infty}{D\alpha_{amp}\pi} \int_0^T C_j(t) \cos \omega t dt, \quad T = \frac{2\pi}{\omega} \quad (72)$$



Since the time steps and pitching moment coefficients obtained from URANS equation are discontinuous, the trapezoidal rule is used to calculate  $C_{j_q} + C_{j_{\dot{\alpha}}}$  as shown in Equation 73:

$$C_{j_q} + C_{j_{\dot{\alpha}}} = \frac{2V_{\infty}}{D\alpha_{amp}\pi} \frac{\Delta t}{2} \sum_{n=1}^{N-1} C_j(t_n) \cos \omega t_n + C_j(t_{n+1}) \cos \omega t_{n+1} \quad (73)$$

Another method for pitch damping calculation is the mean angular displacement position. This method is used by Sahu *et al.* [74] and DeSpirito *et al.* [79] for generic missiles. As shown in Figure 2.6, an hysteresis curve is constructed by plotting the pitching moment coefficient ( $C_{My}$ ) or normal force coefficient ( $C_{Fz}$ ) with respect to angle of attack ( $\alpha$ ). In the hysteresis curve  $C_{j+}$  and  $C_{j-}$  points are determined so that  $C_{j_q} + C_{j_{\dot{\alpha}}}$  can be calculated as shown in Equation 74. It can be simplified for symmetric missile configurations that are oscillated around  $\alpha_0$  as shown in Equation 75:

$$C_{j_q} + C_{j_{\dot{\alpha}}} = (-1)^n \frac{(C_{j_{\pm}} - C_{j_0} - C_{j_{\alpha}} \alpha_0)}{k\alpha_{amp}}, \quad n = 0, 1, 2, \dots \quad (74)$$

$$C_{j_q} + C_{j_{\dot{\alpha}}} = \frac{C_{j+} - C_{j-}}{2k\alpha_{amp}} \quad (75)$$

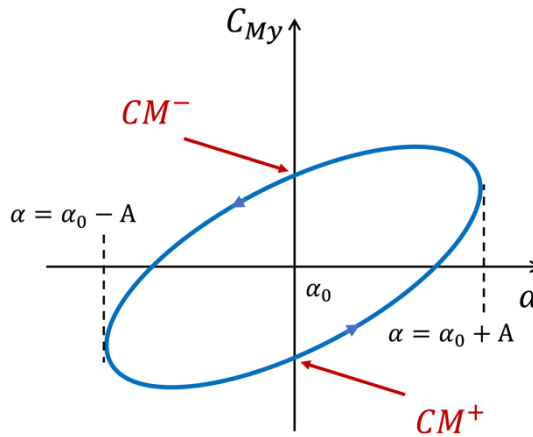


Figure 2.6: Pitching Moment Hysteresis Curve with respect to Angle of Attack



## CHAPTER 3

### COMPUTATIONAL TEST CASES

In this thesis, 3-D, unsteady, separated complex flow fields around missiles are investigated numerically by performing both steady-state and unsteady CFD simulations and by using the exact and approximate Riemann solvers.

A generic missile geometry with basic planar fins [74] is used as an initial computational test case for validation and verification of the Exact Riemann (ER) solver by performing RANS and URANS CFD simulations. The free flight test conditions and the available validated free flight aerodynamic database [74] are used for comparison of the CFD simulations with the test data.

A main computational test case for a generic missile geometry with wrap-around fins [1] is selected and the aerodynamic coefficients are investigated numerically in detail by performing RANS and DDES CFD simulations. The wind tunnel test conditions [1] are used for comparison of the CFD simulations with the available experimental data.

In addition, in order to examine the effects of the Riemann solvers on unsteady aerodynamic simulations, two other test cases with available experimental data are selected for code validation and verification. The unsteady test cases are an airfoil in deep stall in subsonic incompressible flow case with separated flow fields and an airfoil in transonic flow with supersonic flow pocket case with transonic buffeting.

The selected computational test cases, the flow conditions and the numerical approaches used are summarized in Table 3.1. Details of each of these test cases, the model geometries and the computational grids generated with the grid independence

studies, and the flow conditions of test cases are explained in detail in the following sections of this Chapter.

Table 3.1 Computational Test Cases, Flow Conditions and Numerical Approaches

TEST CASES	Flow Conditions		Numerical Approaches
	Mach Number	Angle of Attack	Steady-State / Unsteady CFD
Missile with Basic Fins (Basic Finner Geometry) (Dupuis, 2002 [74])	High Subsonic M = 0.766 & M = 0.934	Low AoA $\alpha = 0^\circ, 5^\circ, 10^\circ$	RANS / URANS
Missile with WAFs (Dahlke Geometry) (Dahlke and Flowers, 1974 [1])	High Subsonic M = 0.5-0.8 Transonic M = 0.937, 1.053, 1.1	Low AoA $\alpha = 0^\circ - 10^\circ$	RANS / DDES
NACA 0021 Airfoil (Swalwell, <i>et al.</i> , 2003 [75])	Low Subsonic M = 0.0947714 Re = 270,000	High AoA $\alpha = 60^\circ$	- / DDES
OAT 15A Airfoil (Joacquin, <i>et al.</i> , 2009 [80])	High Subsonic M = 0.73 Re = 2.6E6	Low AoA $\alpha = 3.9^\circ$	RANS / URANS



respectively. For moment calculations, the centroid of the body is selected at 0.22 m from the nose.

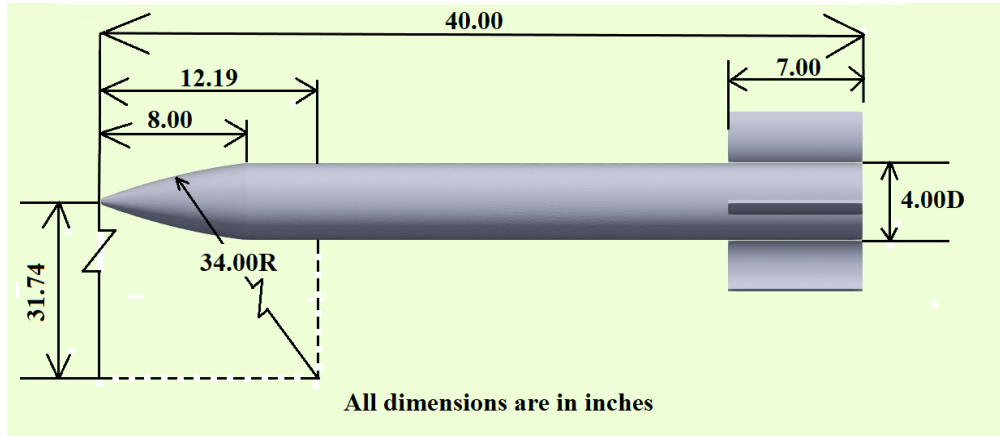


Figure 3.2: Missile with WAFs: Dahlke Missile Model Geometry with Wrap-Around Fins

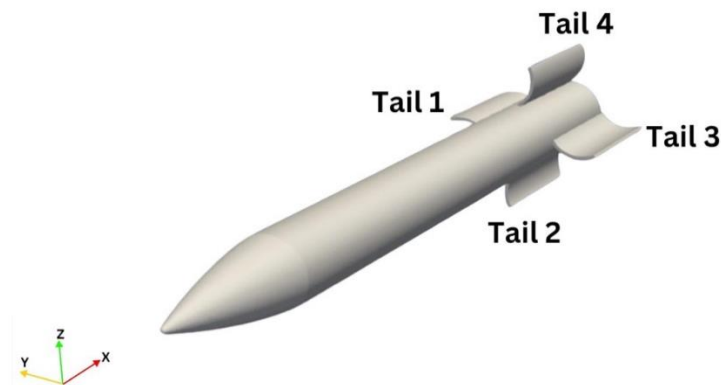


Figure 3.3: Missile with WAFs: 4 Wrap-Around Fins numbered as Tail 1, Tail 2, Tail 3, and Tail 4

The wrap-around tail fins induce a roll moment at different directions in subsonic and supersonic flows under sea level conditions. This case is selected for steady validation for different freestream Mach numbers and angles of attack by the wind tunnel tests [1]. In addition, the differences between Riemann solvers for steady and unsteady cases are illustrated by steady RANS and unsteady DDES simulations

### 3.3 NACA 0021 Airfoil in Deep Stall

The flow separation with high Reynolds number far beyond stall angle of attack is a challenging CFD problem due to challenging physical phenomena such as vortex shedding and turbulence. The NACA 0021 has well documented unsteady test database including unsteady lift and drag history and average pressure coefficients that is performed by Swalwell *et al.* [75, 76]. For that reason, this test case is used as a CFD validation case.

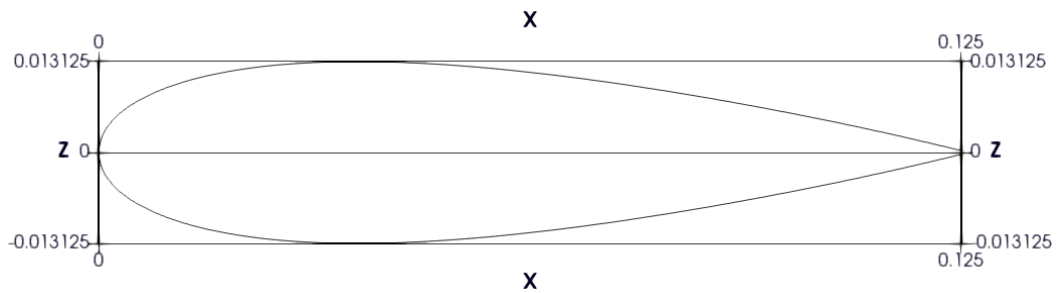


Figure 3.2: NACA 0021 Airfoil

Swalwell, *et al.*, [75] performed a set of wind tunnel tests for NACA 0021 airfoil with a chord length of 0.125 m with a chord length based Reynolds number of 270,000 as shown in Figure 3.4. It corresponds to a freestream Mach number of 0.0947714 for a pressure and temperature of 101325 Pa and 293 K, respectively. The documented unsteady data contain FFT spectrum of lift coefficient, the time averaged coefficient of pressure data on chord axis.

At large angles of attack, the airfoils behave like a bluff body to cause large shedding vortices coupled with an asymmetry and pressure difference. In addition to the well documented unsteady data, the vortex shedding under large pressure gradient presents an important experimental case for validation and comparison of Exact Riemann (ER) solver by Roe's Approximate Riemann solver (ROE). For that reason, the NACA 0021 test case at angle of attack of  $60^\circ$  is analyzed by both Exact Riemann solver and Roe's Approximate Riemann solver.

### 3.4 OAT 15A Airfoil in Transonic Flow

In transonic flow, shockwave boundary layer interaction coupled with flow separation may generate unsteady shock wave i.e. transonic buffeting. Transonic buffeting might have severe effects due to the vibrations on the blade or airfoil. For that reason, Joacqin *et al.* [80] performed a couple of wind tunnel tests to analyze the unsteady oscillations during transonic buffeting for OAT 15A airfoil with a chord length of 0.23 m as shown in Figure 3.5.

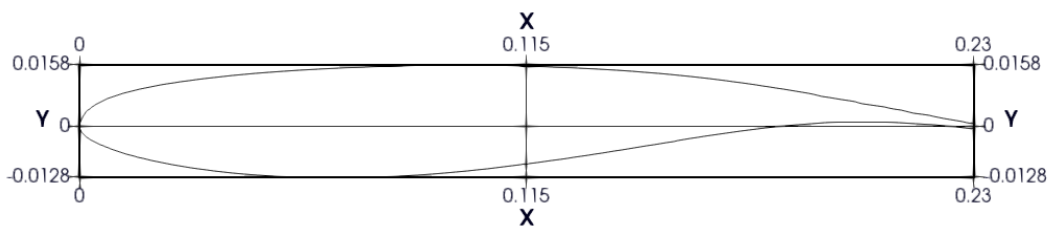


Figure 3.3: OAT 15A Airfoil

Joacquin *et al.* [80] performed the wind tunnel tests at 0.73 freestream Mach number with a chord length based Reynolds number of  $2.9 \times 10^6$ . It corresponds to a freestream pressure and temperature of 77000 Pa and 293.15 K, respectively. In order to compare the ability of Riemann solvers to detect unsteady shockwaves, this case with oscillatory shockwaves is performed. The maximum oscillation on the lift coefficient is observed at angle of attack of  $3.9^\circ$ . In addition to average coefficient of pressure distribution, a pressure probe is set in CFD cases to compare the peaks in the frequency domain with the experimental data.



## CHAPTER 4

### RESULTS FOR MISSILE CFD SIMULATIONS

In this Chapter, the results of the steady-state and unsteady CFD simulations for two selected missile geometries, one with the basic planar fins (Basic Finner Geometry) and one with the wrap-around fins (Missile with WAF: Dahlke Geometry) are presented. The RANS and URANS simulations are performed for the Basic Finner Geometry at Mach numbers of 0.766 and 0.934. The RANS and DDES simulations are performed for the Dahlke Geometry at Mach number of 0.5. The results are obtained by both Riemann solvers and compared with the available experimental data.

#### 4.1 CFD Simulations for Missile with Basic Fins

Basic Finner geometry is a generic rocket with an aerodynamic database including dynamic coefficients which is fitted by a series of repeating tests for trajectory estimation under sea level conditions. For that reason, this geometry is investigated for comparing the aerodynamic derivatives with an explained grid convergency study based on a tetrahedral unstructured grid with a prismatic viscous layers.

##### 4.1.1 Grid Independence Study

Spherical solution domain is constructed with a diameter of 6 meter that is 20 times larger than the missile length. There are two different locally refined volumes which cover tails and the wake region as shown in Figure 4.1. The grid convergency study is performed by four different grids with a refinement factor of 1.25 on each surface on the missile and refined volumes as shown in Table 4.1.

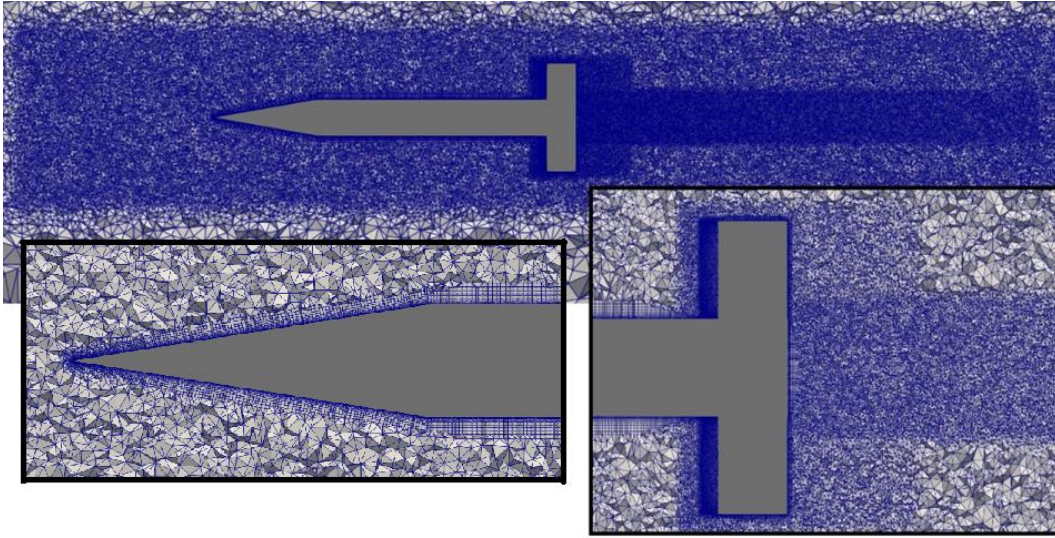


Figure 4.1: Basic Finner: Unstructured Grid

Table 4.1 Basic Finner: Grid Independence Study for RANS Simulations

Grids	Number of Surface Cells	Number of Volume Cells	First Layer Thickness [m]	Grid Size @ Tail [m]	Grid Size @ Wake [m]
Coarse	292682	15E+6	1E-6	8E-4	8E-4
Medium	391676	21E+6	1E-6	6E-4	6E-4
Fine	536808	25E+6	1E-6	5E-4	5E-4
Finest	707028	29E+6	1E-6	4E-4	4E-4

The grid convergency study is performed for ROE solver with Spalart-Allmaras (SA) turbulence model. The implicit time integration with a CFL number of 15.0 is performed for all grids. The surface  $y^+$  is kept below 1.0 as shown in Figure 4.2, for all grids with the first layer thickness of  $1e-6$  m and 30 viscous layers. The residuals decrease minimum four order until the maximum iteration number of 5000 is achieved as shown in Figure 4.3 and Figure 4.4.

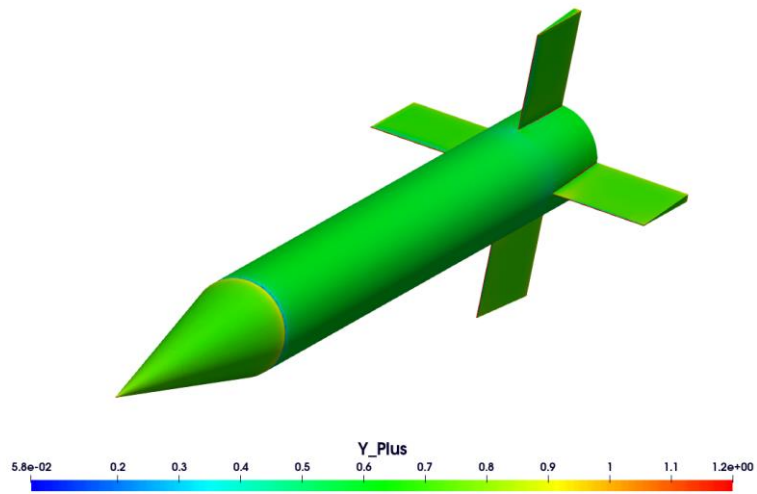


Figure 4.2: Basic Finner:  $y^+$  contours on the surface

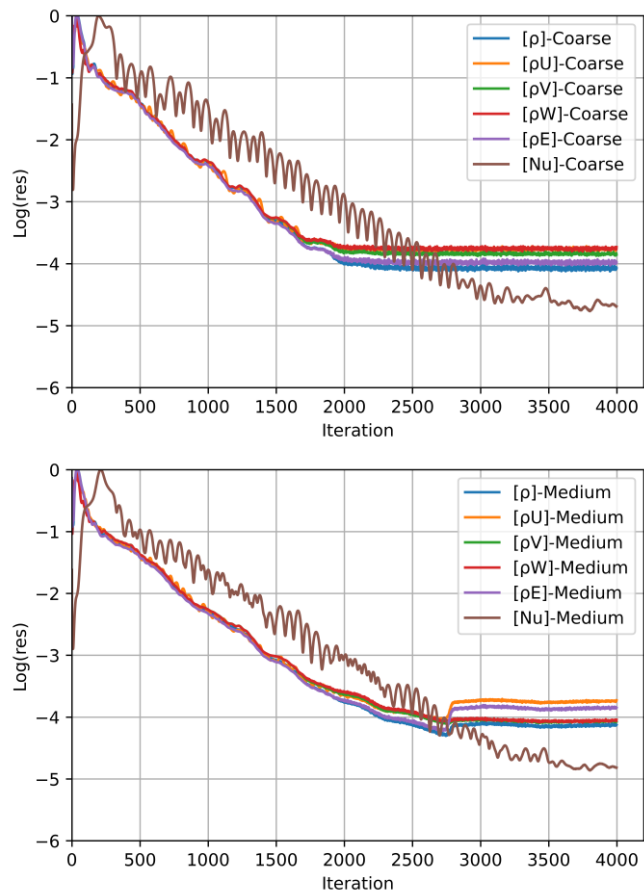


Figure 4.3: Basic Finner: Residual Plots for the Coarse and Medium Grids

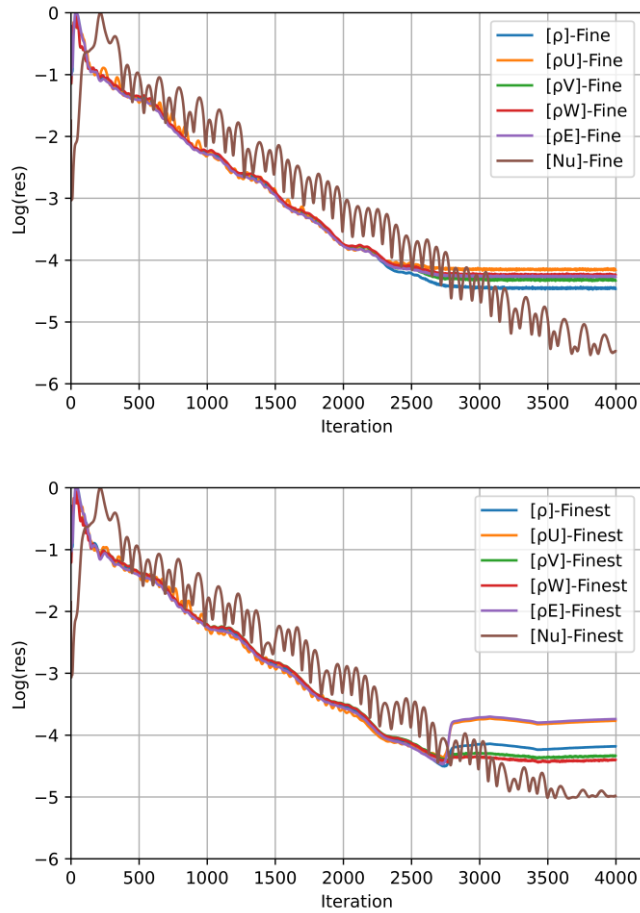


Figure 4.4: Basic Finner: Residual Plots for the Fine and Finest grids

Since there is no control surface on the basic finner generic geometry, a cant angle of two degree is applied between tails and the fuselage in order to have a flight stability by an induced roll moment. For that reason, the roll moment coefficient and axial force coefficient are plotted as shown in Figure 4.5 and 4.6. Since there is a difference of 0.7% and 1.0% on the axial force and roll moment coefficient respectively, the grid with 25 million cell size is used for further RANS cases.

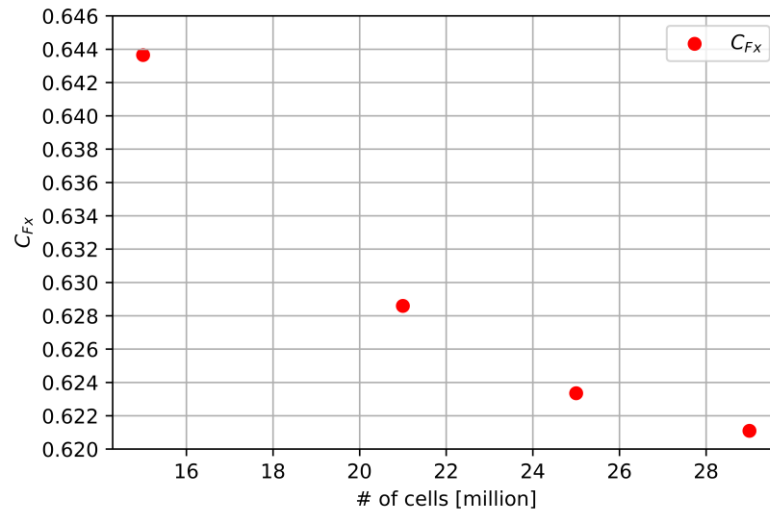


Figure 4.5: Basic Finner: Axial Force Coefficient ( $C_{Fx}$ ) Grid Dependency

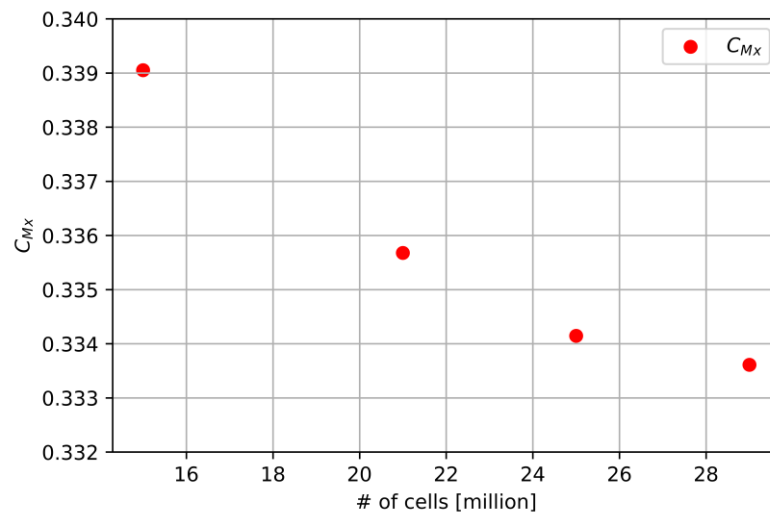


Figure 4.6: Basic Finner: Roll Moment Coefficient ( $C_{Mx}$ ) Grid Dependency

#### 4.1.2 Steady-State Simulations: RANS Results

Dupuis [74] derived the aerodynamic coefficients by multiple data reduction technique in which the time dependent data such as time, position and angles are used to derive static and dynamic aerodynamic coefficients by imposing linear theory and six degree of freedom analyses [29]. In Table 4.2 and 4.3, the static

aerodynamic coefficients are shown for free flight (FF) multiple fit data and RANS results of Exact Riemann (ER) solver and ROE solver with Spalart-Allmaras (SA) and Menter's  $k-\omega$  Shear Stress Transport (SST) turbulence model. The largest difference is observed for the axial force coefficient at angle of attack of  $0^\circ$ . It is expected to be due to the effect of turbulence model on the axial force coefficient.

Table 4.2 Basic Finner - RANS Results: Aerodynamics Coefficients at M = 0.766

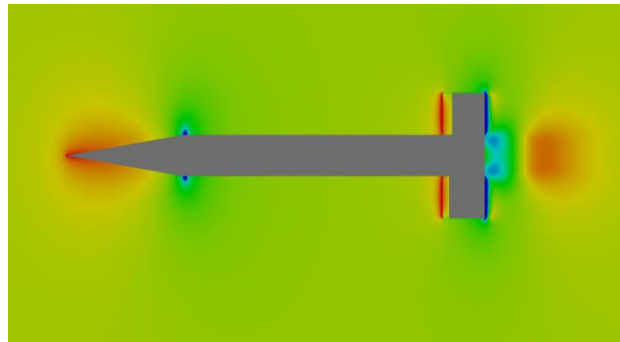
Methods	M	Re	$C_{Fx0}$	$C_{Fz\alpha}$ [rad <sup>-1</sup> ]	$C_{My\alpha}$ [rad <sup>-1</sup> ]	CP [mm]
FF	0.766	5E5	0.508	16.70	-40.80	238.3
ER-SA	0.766	5E5	0.618	16.64	-44.94	245.9
ROE-SA	0.766	5E5	0.623	15.96	-38.06	246.4
ROE-SST	0.766	5E5	0.546	15.94	-43.50	246.9
ER-SST	0.766	5E5	0.547	16.04	-43.02	245.4

Table 4.3 Basic Finner - RANS Results: Aerodynamics Coefficients at M = 0.934

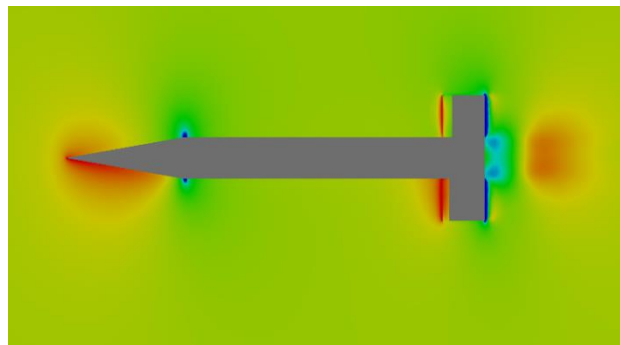
Methods	M	Re	$C_{Fx0}$	$C_{Fz\alpha}$ [rad <sup>-1</sup> ]	$C_{My\alpha}$ [rad <sup>-1</sup> ]	CP [mm]
FF	0.934	6.1E5	0.669	18.30	-47.20	222.6
ER-SA	0.934	6.1E5	0.897	17.76	-50.27	249.8
ROE-SA	0.934	6.1E5	0.893	17.81	-50.45	250.0
ROE-SST	0.934	6.1E5	0.786	17.73	-50.16	249.8
ER-SST	0.934	6.1E5	0.790	17.71	-50.11	249.9

Since the normal force coefficient ( $C_{Fz}$ ) is more sensitive to surface pressure distribution than that of axial force coefficient ( $C_{Fx}$ ), the inviscid flux scheme becomes dominant for normal force coefficient calculations.  $C_{Fz\alpha}$  is the derivative of normal force coefficient with respect to the angle of attack. The results of the Exact Riemann solver are in 0.36% and 2.95% error range for Mach numbers of 0.766 and 0.934, respectively.

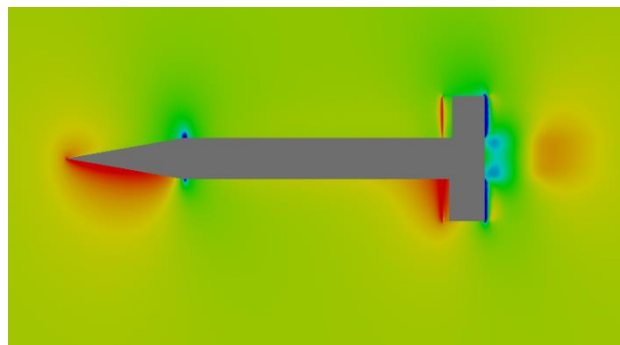
The static stability coefficient  $C_{My\alpha}$  is the derivative of pitching moment with respect to angle of attack. As shown in Table 4.2 and Table 4.3, calculated  $C_{My\alpha}$  is in 10.15% and 6.8% error range for Mach numbers of 0.766 and 0.934, respectively. In spite of its magnitude, the moment arm vector from the center of pressure to the center of gravity might cause large error band in  $C_{My\alpha}$  calculations. For that reason, center of pressure calculation that shows 7.6 mm difference with respect to free flight data for Mach number of 0.766 is performed to check moment arm length difference. The center pressure is in 2.53% error range when it is nondimensionalized by the basic finner geometry length. The error in the center of pressure increases as the Mach number is increased to 0.934 due to the deviation from turbulence models at larger Reynolds numbers. In Figure 4.7 and Figure 4.8, pressure and Mach contours around the basic finner geometry are shown at varying angle of attack, respectively.



a)  $\alpha = 0^\circ$



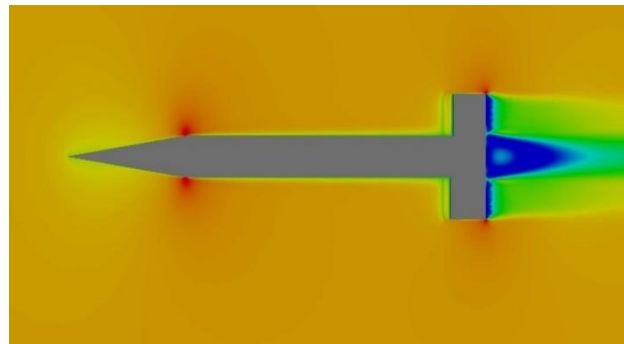
b)  $\alpha = 5^\circ$



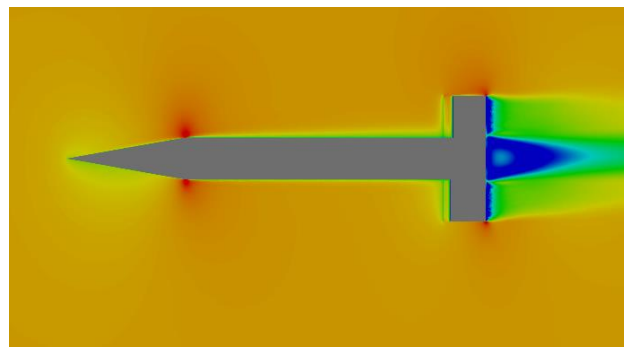
c)  $\alpha = 10^\circ$

Figure 4.7: Basic Finner: Pressure contours at sea level for  $M_\infty = 0.766$  at different angles of attack of  $\alpha = 0^\circ, 5^\circ, 10^\circ$

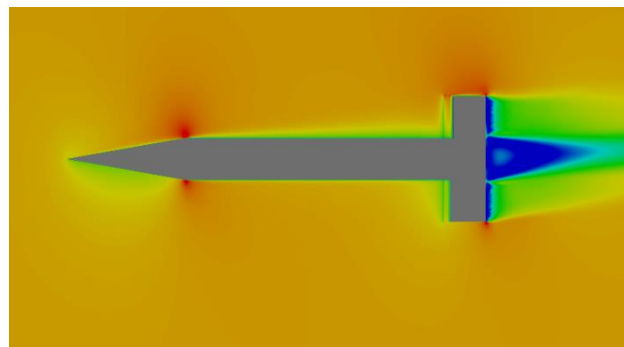




a)  $\alpha = 0^\circ$



b)  $\alpha = 5^\circ$



c)  $\alpha = 10^\circ$

Figure 4.8: Basic Finner: Mach contours at sea level for  $M_\infty = 0.766$  at different angles of attack of  $\alpha = 0^\circ, 5^\circ, 10^\circ$

### 4.1.3 Unsteady Simulations: URANS Results for Dynamic Coefficients

Dupuis [74] derived also the dynamic aerodynamic coefficients by multiple fitting technique to the free flight data. The pitch damping coefficient term derivation through CFD is performed by imposing a forced pitching motion as shown in Figure 2.5a. The missile diameter is used as characteristic length for determining the required frequency from a reduced frequency of 0.05 as shown in Table 4.4.

Since the converged RANS result is used as initial condition in URANS case, the pattern of pitching moment coefficient  $C_{M\dot{\gamma}}$  and normal force coefficient  $C_{Fz}$  start to have sinusoidal shapes after tens of iterations as shown in Figure 4.9 and 4.10. The hysteresis curve of the pitching moment coefficient based on angle of attack has a repeatable pattern as shown in Figure 4.11. For that reason, the mean angular displacement method is also used in  $C_{Mq} + C_{M\dot{\alpha}}$  calculation as shown in Figure 4.11.

The  $C_{Mq} + C_{M\dot{\alpha}}$  calculation, the combination of the pitch damping coefficient and the dynamic stability coefficient, is performed by both mean angular displacement and integration over period method as shown in Table 4.5. As shown in Figure 4.12, there is no difference between converged results for single and double period integration methods. Although the results have a discrepancy of 2-4% from other CFD works in the literature [78, 80], there is a wide range of gap between the free flight multiple fit data by Dupuis [74]. Since the combination of the pitch damping coefficient and the dynamic stability coefficient ( $C_{Mq} + C_{M\dot{\alpha}}$ ) is calculated from time average of each cycle, the possible behaviour in free flight may not indicate full cycle time average precisely.

Table 4.4 Basic Finner - URANS: CFD Simulation Parameters at M = 0.766

Methods	Re	Time Step [sec]	Omega [rad/s]	Amplitude [deg]
URANS	5E5	36E-6	876.304	0.5

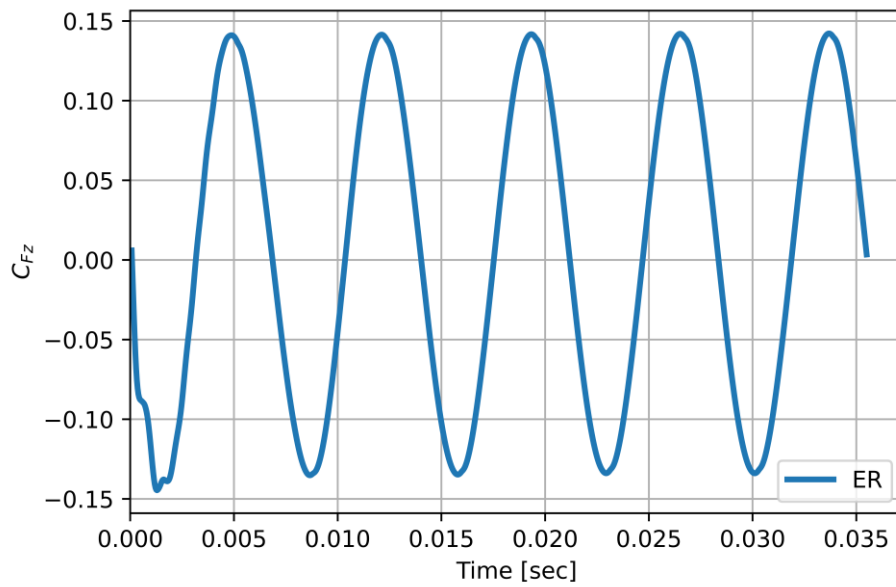


Figure 4.9: Basic Finner: Normal Force Coefficient ( $C_{Fz}$ ) vs Time in Forced Pitching using ER Solver

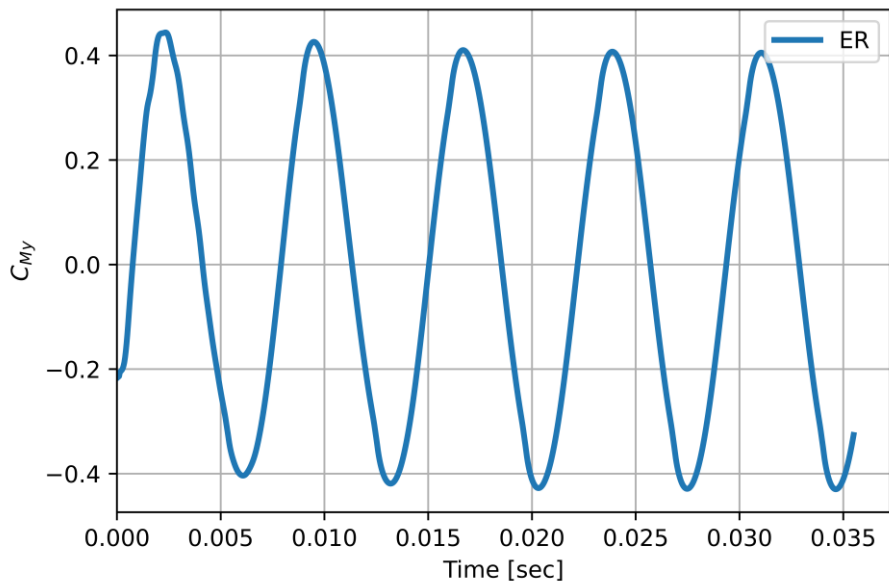


Figure 4.10: Basic Finner: Pitching Moment Coefficient ( $C_{My}$ ) vs Time in Forced Pitching using ER Solver

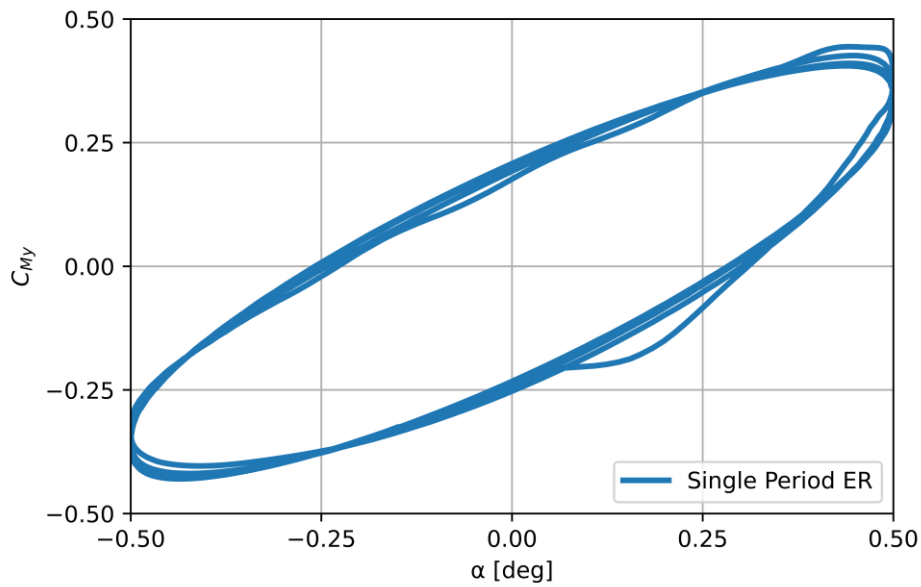


Figure 4.11: Basic Finner: Pitching Moment Coefficient Hysteresis Curve ( $C_{My}$  vs  $\alpha$ ) in Forced Pitching using ER Solver

Table 4.5 Basic Finner - URANS Results: ( $C_{Mq} + C_{M\dot{\alpha}}$ ) Calculations

Methods	$C_{Mq} + C_{M\dot{\alpha}}$ [rad <sup>-1</sup> ]
Single Period Integration Method	-513
Double Period Integration Method	-513
Mean Angular Displacement Method	-518
Single Period Integration Method [78]	-487
Single Period Integration Method [80]	-498
Dupuis Method [72]	-224

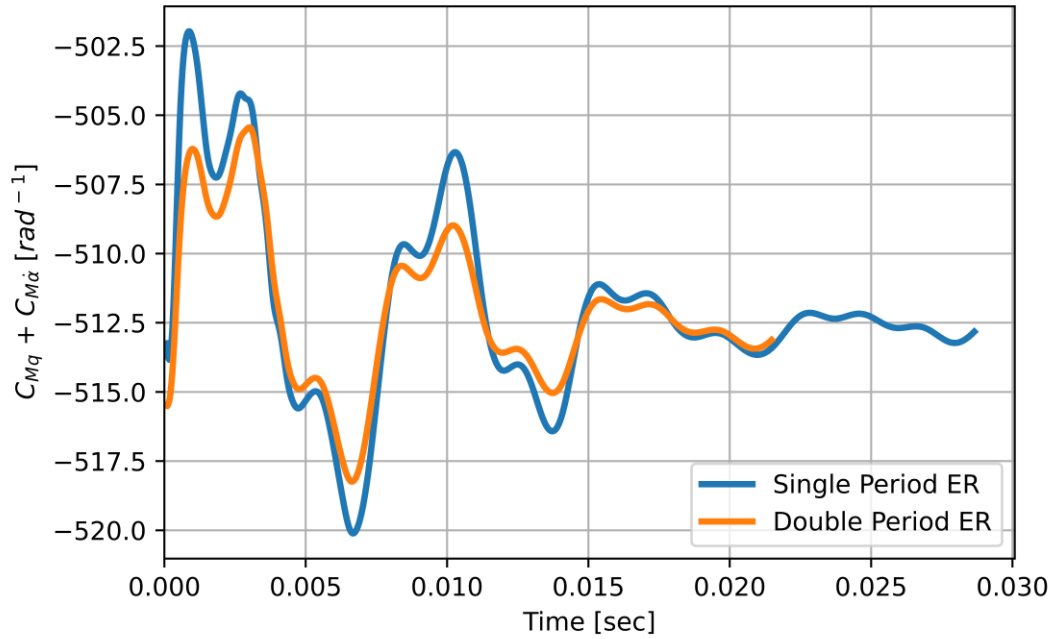


Figure 4.12: Basic Finner: Pitch Damping Coefficient ( $C_{Mq} + C_{M\dot{\alpha}}$ ) vs Time in Forced Pitching using ER Solver

#### 4.1.4 Summary and Discussions

In this test case, the static aerodynamic coefficients are calculated by both Riemann solvers by RANS simulations. Since the unsteady effects are completely modeled by eddy viscosity in RANS cases, there is no notable difference between Riemann solvers on static aerodynamic coefficients. The pitch damping coefficient is calculated by mean angular displacement and integration method techniques. Although the results have a discrepancy of 100% with the free flight data, there is a discrepancy range of 2-4% with the available results in the literature [78, 80]. This case is used to emphasize that there is no effect of the Riemann solver in steady cases.

## 4.2 CFD Simulations for Missile with Wrap-Around Fins

A generic geometry of a wrap-around fin missile is tested by Dahlke in wind tunnel test campaign in which the induction of roll moment and its response to increasing freestream Mach number are investigated experimentally. A numerical approach starting from grid dependency is pursued in order to have understanding the variation of roll moment induction under increasing angles of attack. In the final section, DDES case is performed for comparing the differences between Roe's Approximate Riemann solver and the Exact Riemann solver.

### 4.2.1 Grid Independence Study

The spanwise dimension constructed with a diameter of 12 meter that is 12 times larger than the missile length. There are three different locally refined volumes which cover nose, tails and the wake region as shown in Figure 4.13. The grid convergency study is performed by four different grids with a refinement factor of 1.25 on each surface on the missile and refined volumes as shown in Table 4.6.

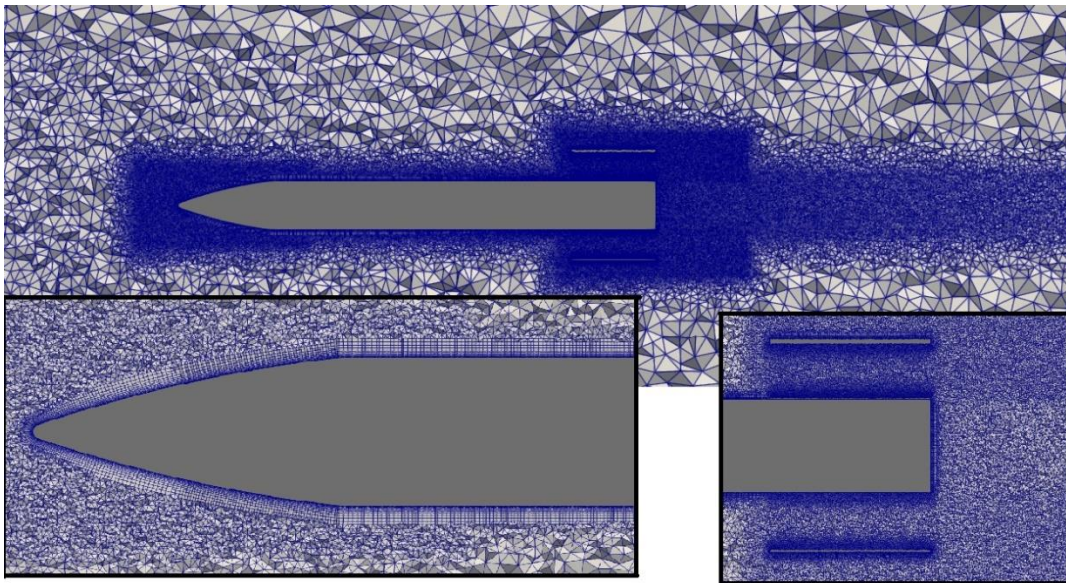


Figure 4.13: Missile with WAFs: Unstructured Grid

The first layer thickness is kept as  $2e-6$  meter for having a  $y^+$  below 1.5 for majority of the surface grid as shown in Figure 4.14. The surface of the missile is covered by maximum 36 viscous layers with a growth ratio of 1.25. Viscous layer addition is automatically stopped when the volume ratio of 1.5 is achieved with the adjacent tetrahedral cell after the addition of first layer.

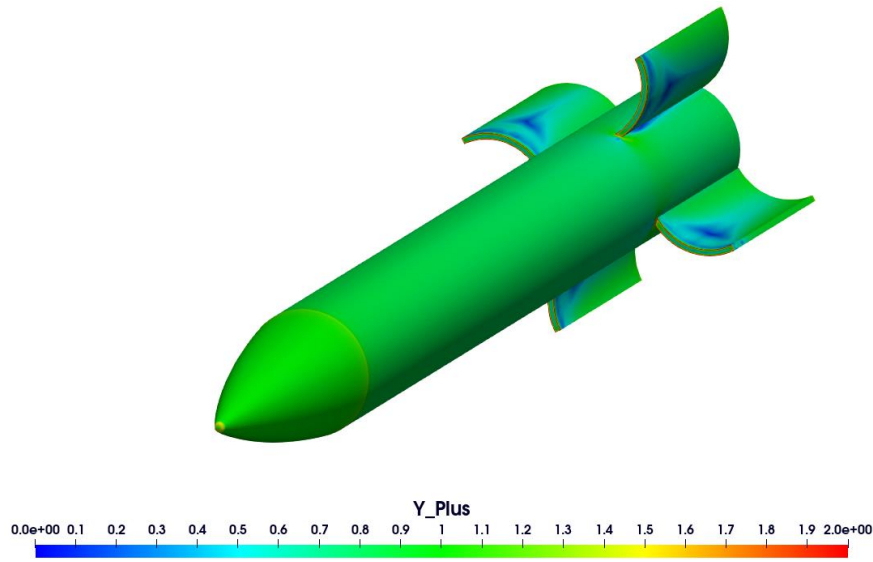


Figure 4.14: Missile with WAFs:  $y^+$  contours on the surface grid

Roe's Approximate Riemann solver is used in the grid convergency case with Spalart-Allmaras turbulence model. The implicit time integration is used for having a CFL number of 15.0 for easier convergence. The residuals decrease three order after 4000 iterations as shown in Figure 4.15-4.18.

Table 4.6 Missile with WAFs: Grid Independence Study for RANS Simulations

Grids	Number of Surface Cells	Number of Volume Cells	First Layer Thickness [m]	Grid Size @ Tail [m]	Grid Size @ Wake [m]	Grid Size @ Nose [m]
Coarse	223698	10E+6	2E-6	5E-3	5E-3	5E-3
Medium	381488	16E+6	2E-6	4E-3	4E-3	4E-3
Fine	540660	24E+6	2E-6	3E-3	3E-3	3E-3
Finest	791652	36E+6	2E-6	2E-3	2E-3	2E-3

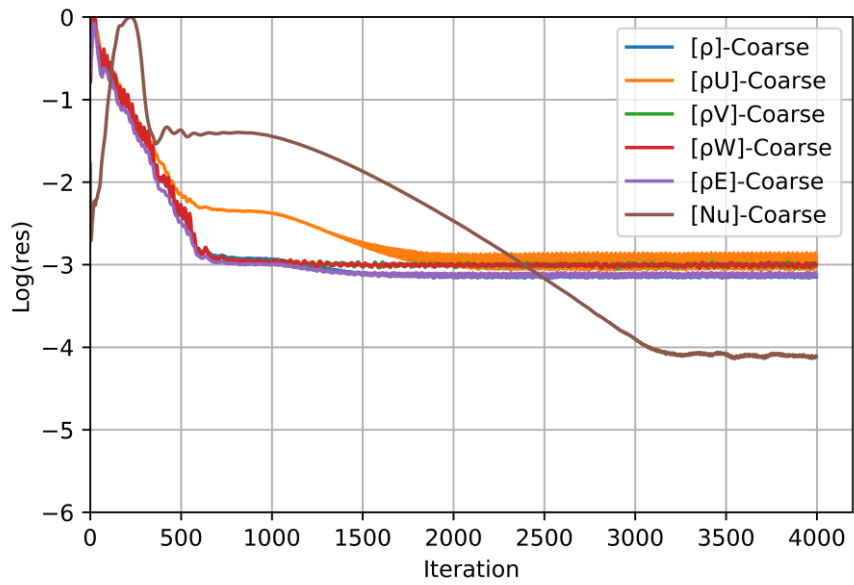


Figure 4.15: Missile with WAFs: Residual plots for coarse grid

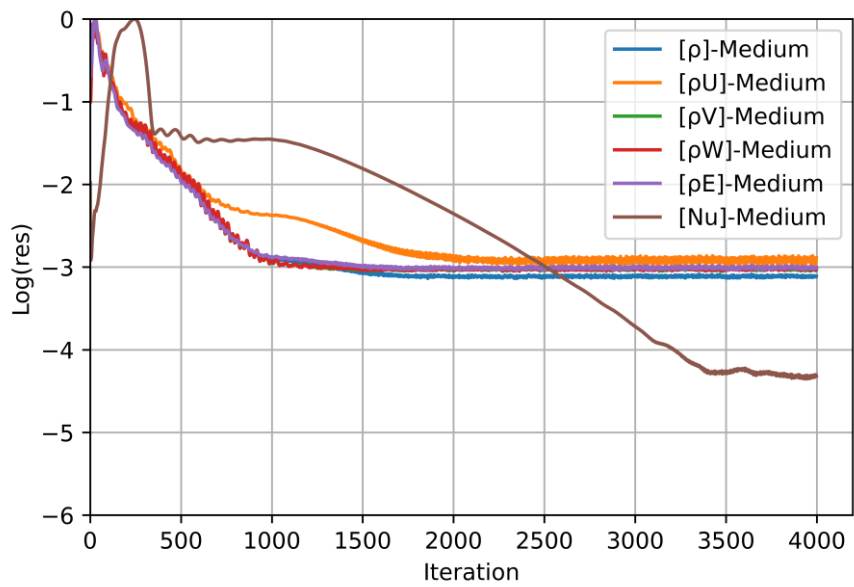


Figure 4.16: Missile with WAFs: Residual plots for medium grid



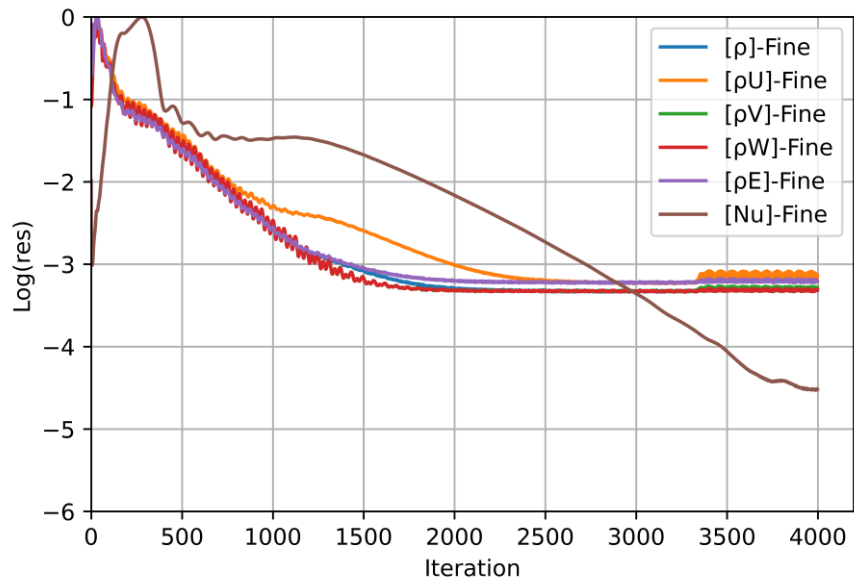


Figure 4.17: Missile with WAFs: Residual plots for fine grid

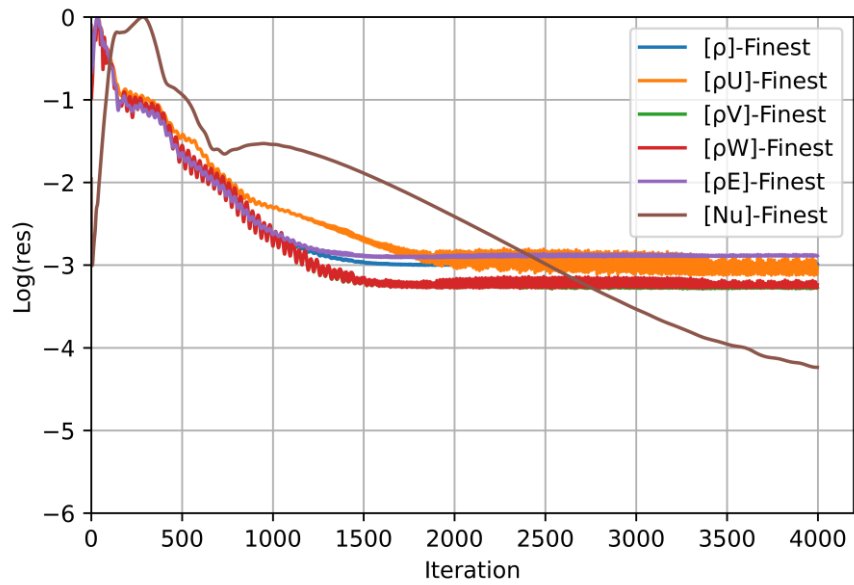


Figure 4.18: Missile with WAFs: Residual plots for finest grid

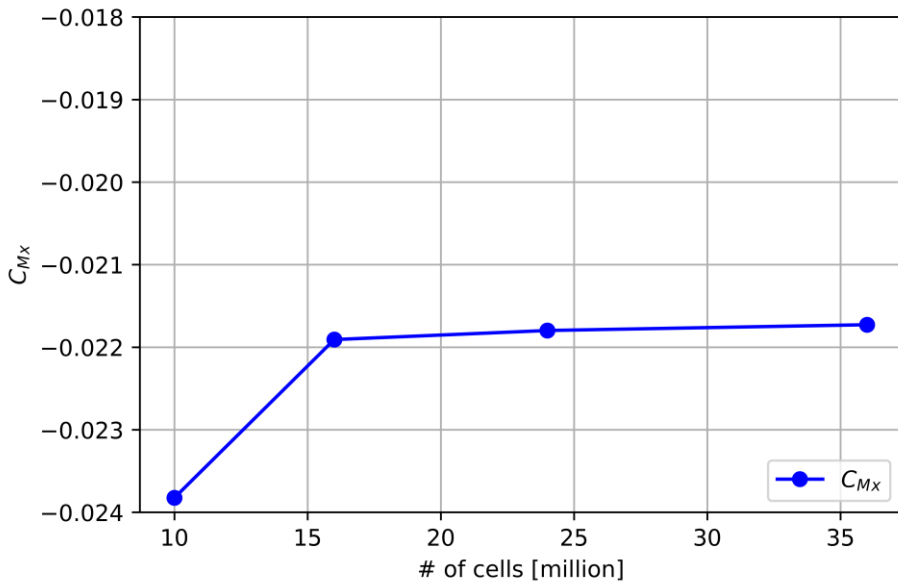


Figure 4.19: Missile with WAFs: Roll Moment Coefficient Grid Dependency

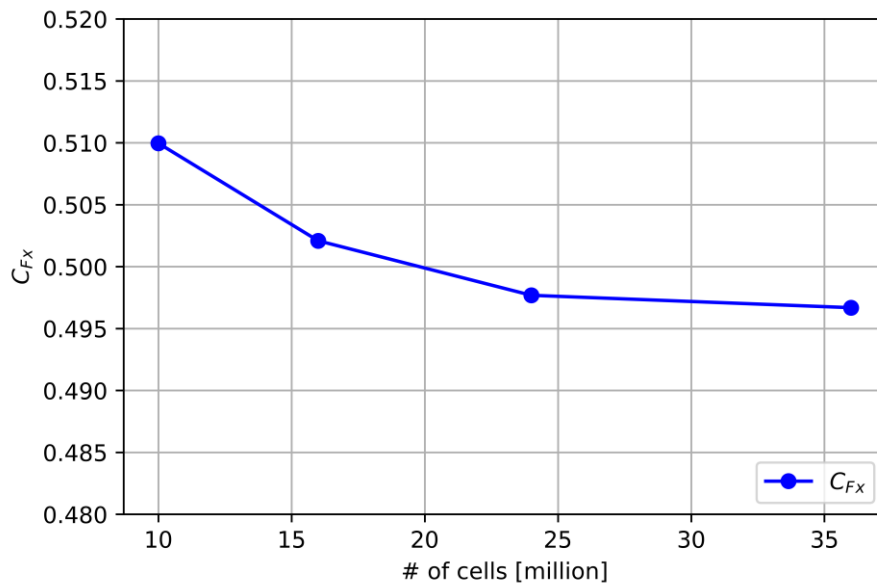


Figure 4.20: Missile with WAFs: Axial Force Coefficient Grid Dependency

Monotone decrease is achieved in both roll moment and axial force coefficients as shown in Figure 4.19 and 4.20. Since the change in the aerodynamic coefficient is less than 0.2% in both roll moment and normal force coefficients, the fine grid is used in further analyses.

#### 4.2.2 Roll Induction for Missiles with Wrap-Around Fins

The wrap-around fins are in wrapped position inside the launch tube, there is no need to have a closure slots on the body as it is required for traditional tail fins. For those reasons, the illustration of roll induction mechanism for the wrap-around tail fins that are preferred in subsonic tactical missiles is of paramount importance

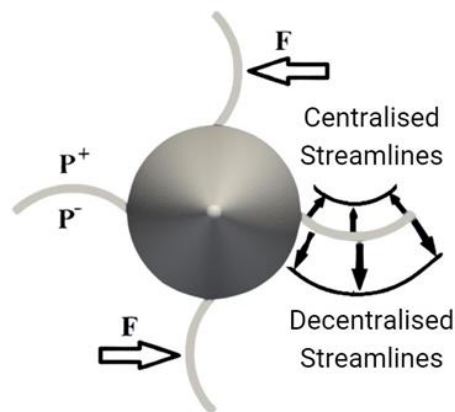


Figure 4.21: Missile with WAFs: Roll Induction in Subsonic Flow

The roll induction mechanism is associated with the behavior of streamlines in Euler equations due to the no through boundary condition. Each wrap-around fin distracts all the streamlines around its body such that the streamlines are separated as decentralized and centralized on the upper and lower regions of the fin, respectively, as shown in Figure 4.21.

Since the vertical area is decreasing between the streamlines in the centralized region, the relative velocity is expected to increase whereas the pressure decreases. The same aerodynamic phenomenon occurs inversely for the decentralized region. Thus, a pressure difference occurs from decentralized to centralized region from upper to lower surface of the fin. At zero angle of attack flight condition, the net forces cancel out each other while inducing a moment in the x direction. Therefore, a roll moment is induced in the x direction while there is no net force in y and z

directions. Abate used a converging diverging nozzle analogy to explain the roll moment induction and shift of direction in supersonic flows [12].

#### 4.2.2.1 Effects of Mach Number

The effect of Mach number on roll moment coefficient in subsonic regime has tendency to increase the roll moment coefficient until transonic effects appears around Mach number of 0.8. Since the converging-diverging analogy of Abate requires sign shift of roll moment under supersonic conditions, the transonic effects make the sign reversal of the coefficient in a more continuous manner [12].

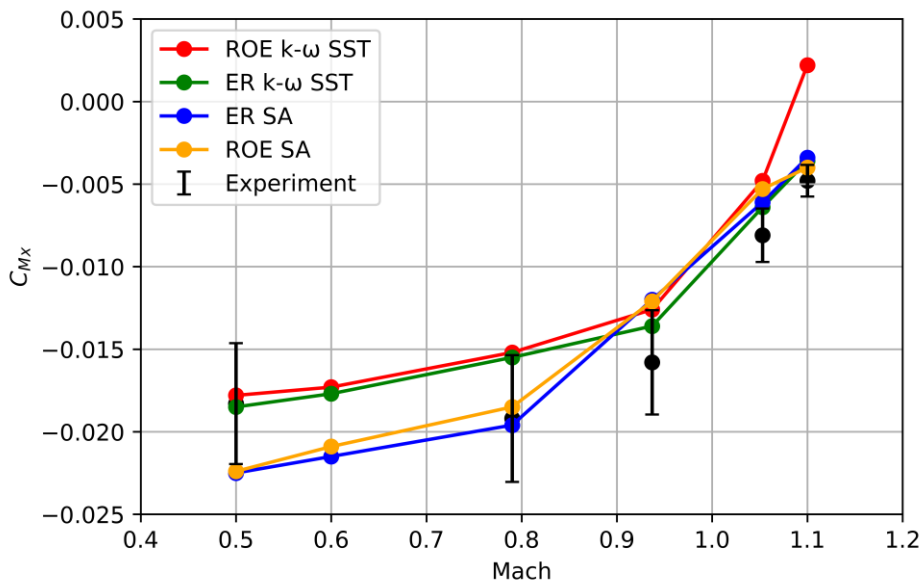


Figure 4.22: Missile with WAFs: Comparison of CFD results with Dahlke wind tunnel tests

In Figure 4.22, the wind tunnel results of Dahlke’s geometry with the CFD results are compared. Dahlke added an uncertainty of measured cant angle sensitivity of  $0.1^\circ$  which corresponds to a magnitude of 0.005 – 0.002 in terms of  $C_{Mx}$  coefficients as specified error bars.

The discrepancy is smaller in the Exact Riemann solver coupled with  $k-\omega$  SST turbulence model than Spalart-Allmaras. In subsonic Mach numbers, the results between Roe's Approximate Riemann solver and the Exact Riemann solver show a small difference that might be due to the small dissipation of Roe's Approximate Riemann solver due to the entropy fixing as shown in Figure 4.23 and 4.24.

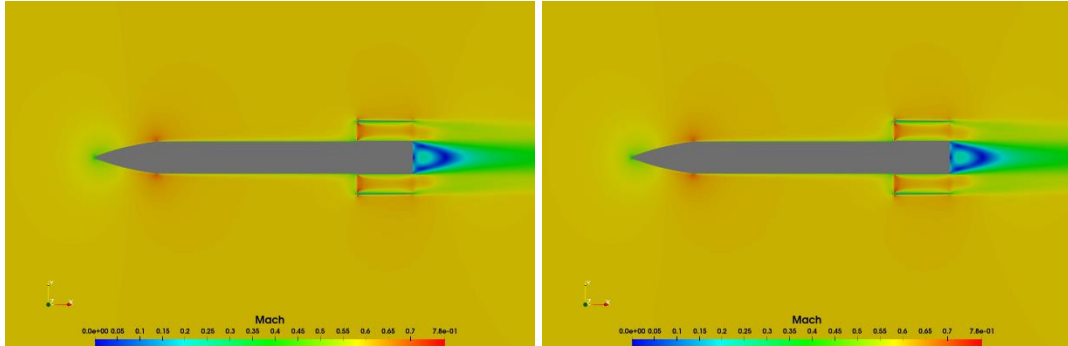


Figure 4.23: Missile with WAFs: Mach Contours at  $M = 0.6$  for  
 (a) Exact Riemann (b) Roe's Approximate Riemann solver with SA

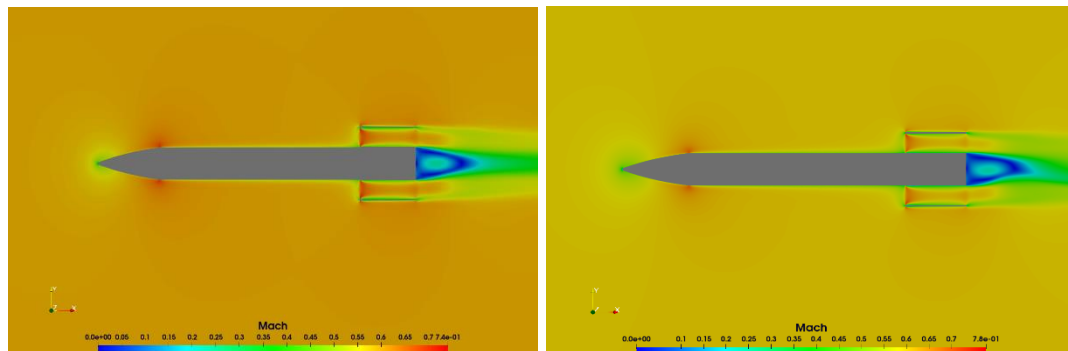


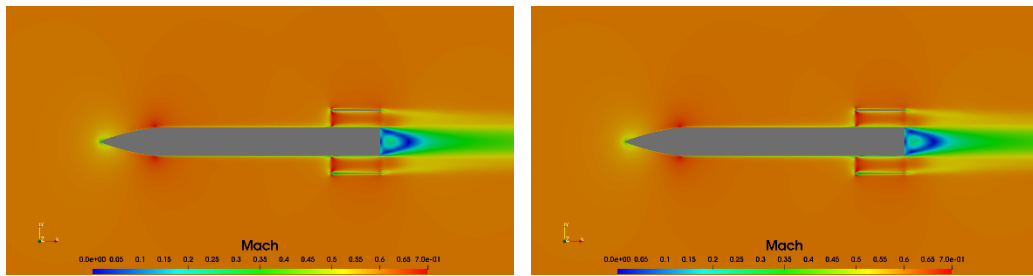
Figure 4.24: Missile with WAFs: Mach Contours at  $M = 0.6$  for  
 (a) Exact Riemann and (b) Roe's Approximate Riemann solvers with  $k-\omega$  SST

The Mach contour plots for the results of RANS simulations for the missile with WAFs at different Mach numbers ( $M = 0.6, 0.937, 1.053,$  and  $1.1$ ) are shown in Figures 4.25 and 4.26 for different turbulence models. The results are also obtained with both the Exact Riemann (ER) and Roe's Approximate Riemann (ROE) solvers and by using Spalart-Allmaras (SA) and  $k-\omega$  SST turbulence models. As the Mach number is increased from high subsonic condition ( $M = 0.6$ ) to the transonic

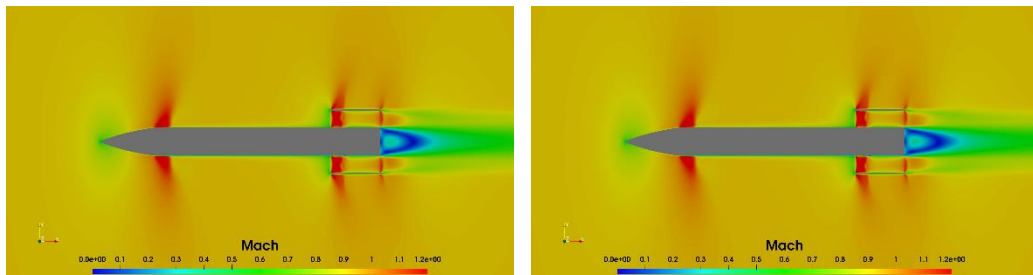
conditions ( $M = 0.937, 1.053, \text{ and } 1.1$ ), the flow fields with shock waves are observed from the Mach contours in the Figures 4.25 and 4.26 as expected. Smaller differences can be observed with ER and ROE solvers and also with SA and  $k-\omega$  SST turbulence models, especially in the separated wake regions.

The pressure coefficient distribution for Mach number of 1.1 is plotted in Figure 4.27. The inverse symmetry between the midspan of the Tail 3 and Tail 1 is visible due to angle of attack of  $0^\circ$  as shown in Figure 4.27. Coefficient of pressure in the mid span of the Tail 3 is plotted in Figure 4.28. The upper section and lower section denotes the larger and smaller  $z$  coordinates, respectively. The shock waves are distinguished in terms of coefficient of pressure whereas there is no notable difference for different turbulence models and Riemann solvers.

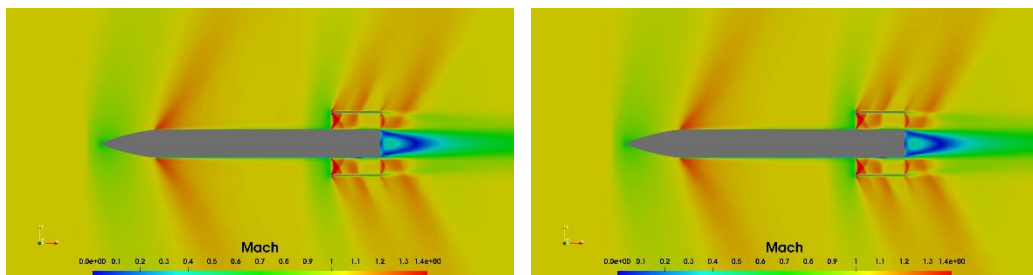
The asymmetry between the upper and lower sections are clear as shown in Figure 4.28. The shock waves in the upper section are not as strong as in lower section due to the strong concavity in the upper section. Nevertheless, the subsonic flow after the shock wave caused another acceleration inside the concavity that leads to another subsequent shock wave. Although similar shock wave patterns can be observed on both sides of the tails, the difference of concavity leads to asymmetric pattern and roll induction even at an angle of attack of  $0^\circ$ .



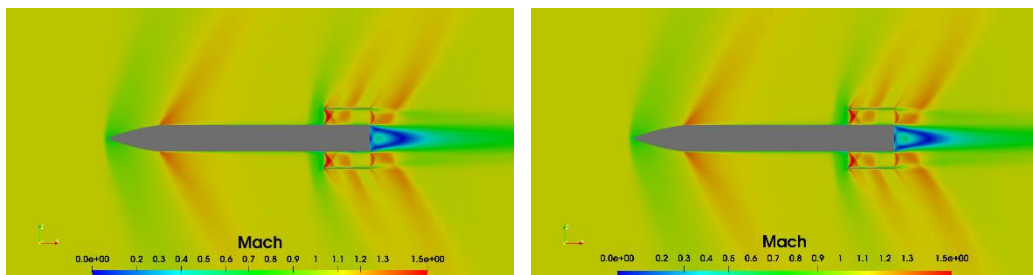
(a)  $M = 0.6$



(b)  $M = 0.937$

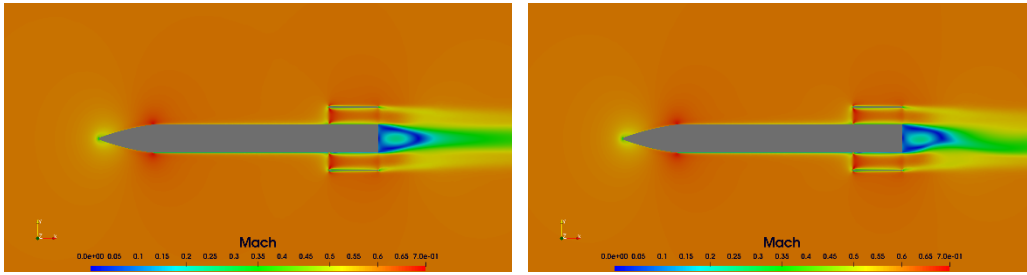


(c)  $M = 1.053$

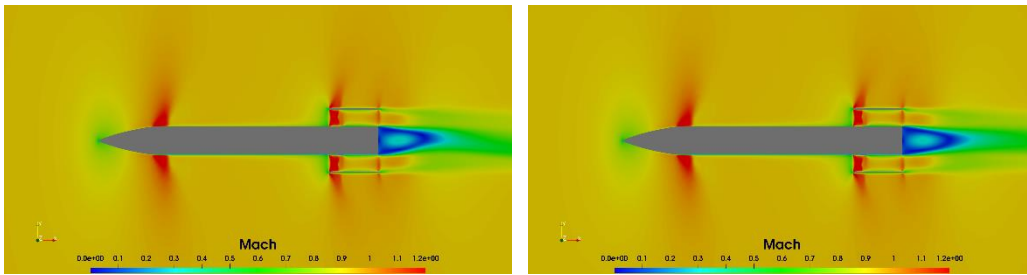


(d)  $M = 1.1$

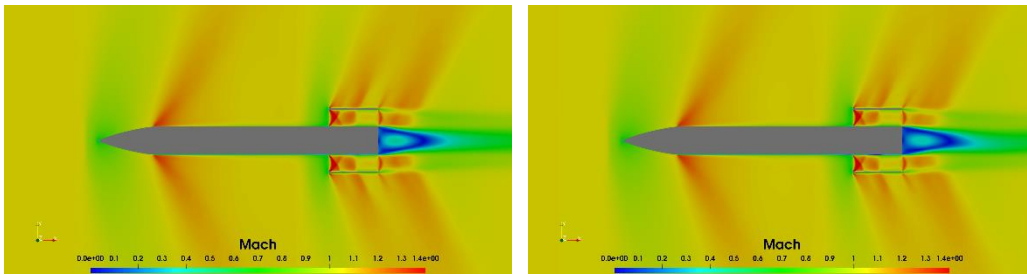
Figure 4.25: Missile with WAFs: Mach contours for different Mach number flow conditions at  $M = 0.6, 0.937, 1.053,$  and  $1.1$  for RANS simulations with SA turbulence model by using ER (left) and ROE (right) Riemann solvers



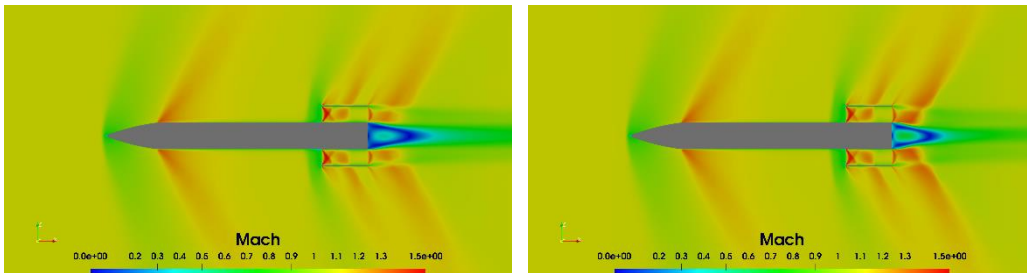
(a)  $M = 0.6$



(b)  $M = 0.937$



(c)  $M = 1.053$



(d)  $M = 1.1$

Figure 4.26: Missile with WAFs: Mach contours for different Mach number flow conditions at  $M = 0.6, 0.937, 1.053,$  and  $1.1$  for RANS simulations with  $k-\omega$  SST turbulence model by using ER (left) and ROE (right) Riemann solvers



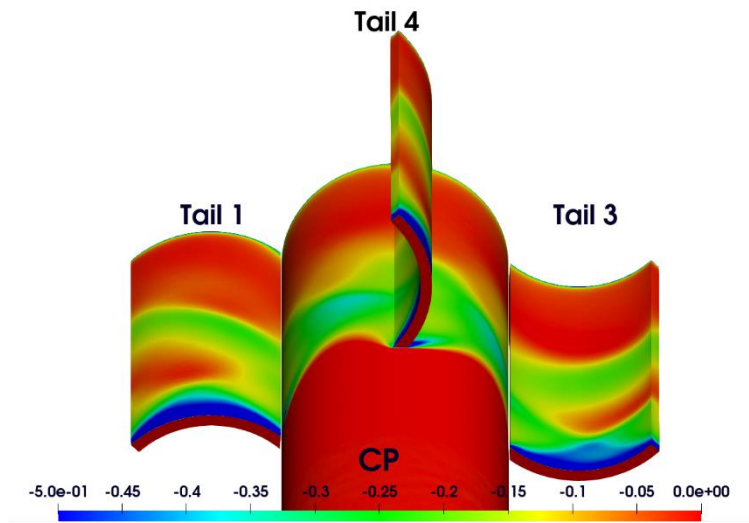


Figure 4.27: Missile with WAFs: Pressure Coefficient Distribution at  $M = 1.1$   
Exact Riemann solver with Spalart-Allmaras

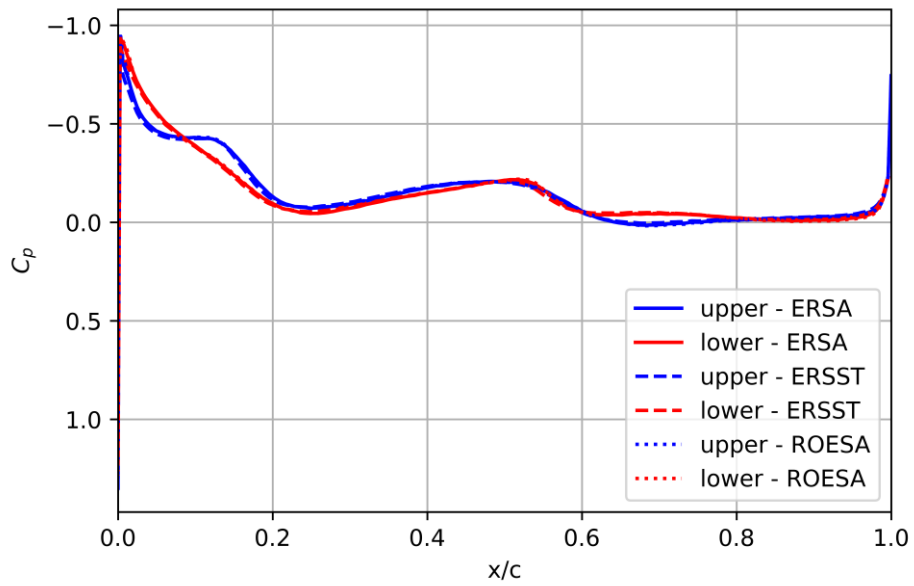


Figure 4.28: Missile with WAFs: Pressure Coefficient vs Chord along Midspan on  
Tail 3

#### 4.2.2.2 Effects of Angle of Attack

The effect of angle of attack on the roll moment coefficient is examined by a series of CFD analyses for angle of attack between  $0^\circ$  and  $10^\circ$ . Implicit density based coupled solver settings are used with Spalart-Allmaras turbulence model. Surface  $y^+$  values are kept smaller than 1 on wall boundary conditions and no wall function is used. The standard Roe scheme [27] without low dissipation is chosen as the convective numerical method. GMRES linear solver with ILU preconditioner is chosen with 25 maximum number of iterations for the implicit solver. The side slip angle  $\beta$  is not taken into consideration due to its generation of roll moment even for planar fins under asymmetric flight conditions due to the body blockage effect over the tails.

In Figure 4.29 and 4.30, the normal force coefficient and roll moment coefficient variation with the angle of attack are shown at a freestream Mach number of 0.5, respectively. The normal force coefficient has linear variation with respect to angle of attack as expected from the literature [2, 5]. On the other hand, the variation of roll moment coefficient with angle of attack loses linearity particularly for angle of attack larger than  $6^\circ$  as shown in Figure 4.30.

Due to the nonlinearity in the roll moment coefficient, the missile roll moment coefficient are decomposed with respect to the tail numbering in Figure 3.2. Since the positive angle of attack is applied on the positive z direction, the roll moment of Tail 1 and Tail 3 have different signs but close to each other in magnitude. For that reason, their resultant contribution is taken into the account in the calculations as shown in Figure 4.31.

As expected, body has no contribution to the roll moment due to its symmetry and short moment arm in the roll direction. The contribution from Tail 2 shows more linear tendency with respect to the Tail 1+3 and Tail 4.

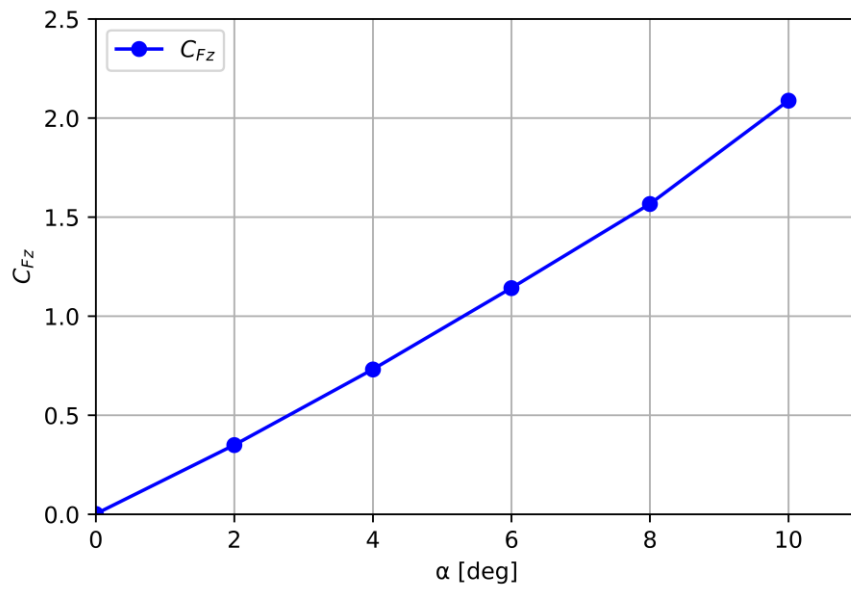


Figure 4.29: Missile with WAFs: Normal Force Coefficient ( $C_{Fz}$ ) vs Angle of Attack at  $M = 0.5$

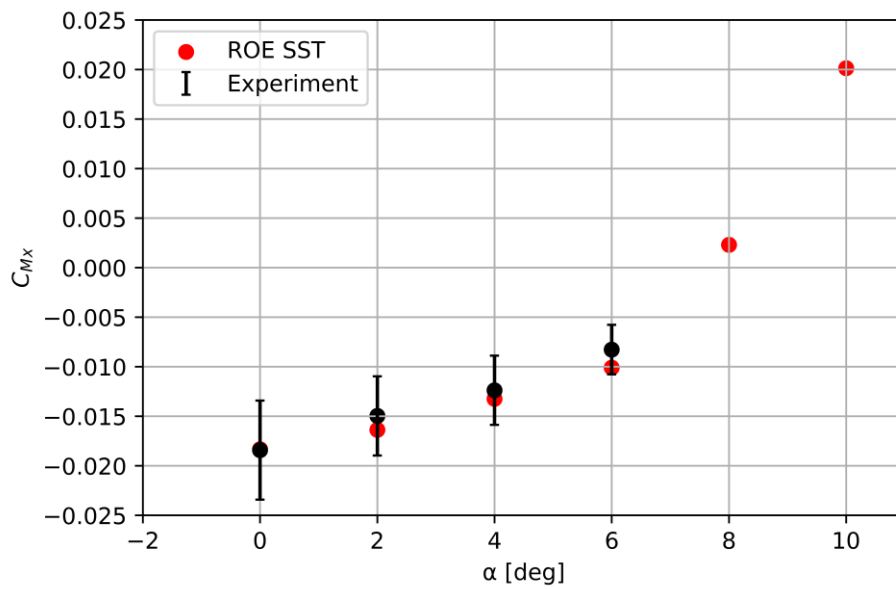


Figure 4.30: Missile with WAFs: Roll Moment Coefficient ( $C_{Mx}$ ) vs Angle of Attack at  $M = 0.5$

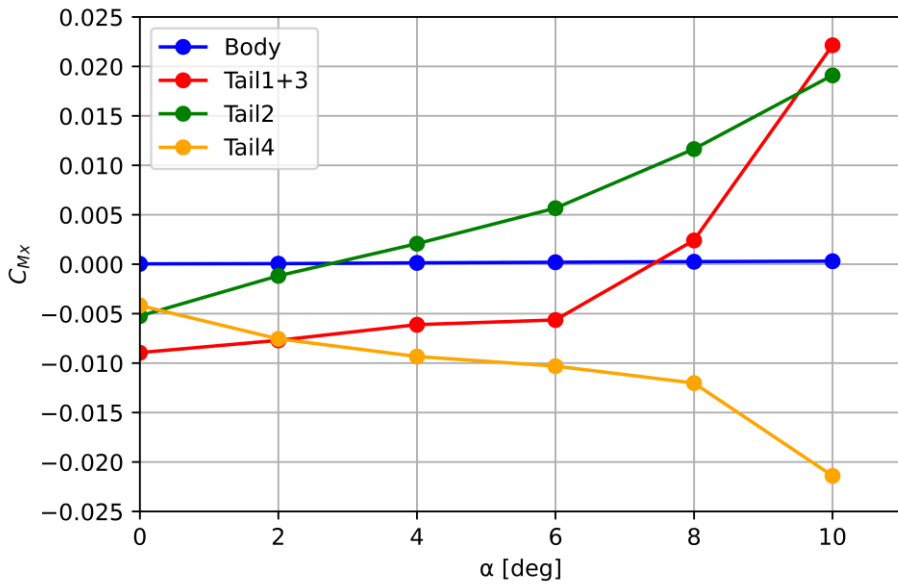


Figure 4.31: Missile with WAFs: Partial  $C_{Mx}$  contributions of body parts (Body only, Tail 1 and 3, Tail 2 only and Tail 4 only) at  $M = 0.5$

Since the air velocity is higher on the inner section of the wrap-around fin, the pressure is lower on that section. However, as the air velocity gains a component towards the inner section, it increases the pressure over that region as shown in Figure 4.32 due to the fact that the air flow expands in inner section and compresses in outer section as shown in Figure 4.33.

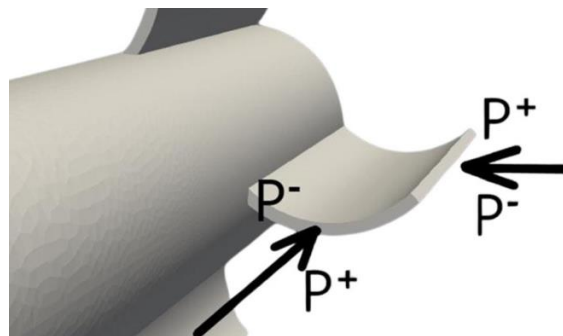


Figure 4.32: Missile with WAFs: Velocity decomposition on Tail 2 in a nonzero Angle of Attack

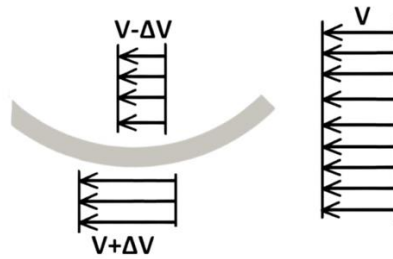


Figure 4.33: Missile with WAFs: Expansion and compression in Tail 2 in a nonzero Angle of Attack

Therefore, the lateral velocity component causes local pressure increase to suppress the pressure decrease by the axial velocity component. For that reason, roll moment contribution of Tail 2 gains an inverse tendency with respect to the angle of attack of  $0^\circ$  orientation. Therefore Tail 2 changes its sign as the angle of attack increases.

The inverse of this phenomenon occurs for Tail 4 with an increasing tendency. However, Tail 4 has a nonlinearity at larger angle of attack unlike Tail 2 due to the body blocking effect. Due to the body blockage, Tail 4 indicates a nonlinearity at angle of attack of  $10^\circ$ .

The contribution from Tail 1+3 has less deterministic nature than the others. Since the Tail 1 produces a negative force with respect to the angle of attack direction, the increasing angle of attack reduces the stall margin and vice versa for Tail 3. For that reason, the local separation regions over those fins are less anticipated than the others.

Since Tail 3 produces positive lift at zero angle of attack unlike Tail 1, at positive angle of attack the contribution from Tail 3 is always larger than that of Tail 1. For that reason, their moments with respect to missile axis are not equal to each other even if they have the same moment arm.

The moment arm on Tail 1 and Tail 3 is the point where the center of pressure exists. Since the flow separation on the tails are varying due to the wrap-around shape, center of pressure on Tail 1 and Tail 3 are different unlike planar fins.

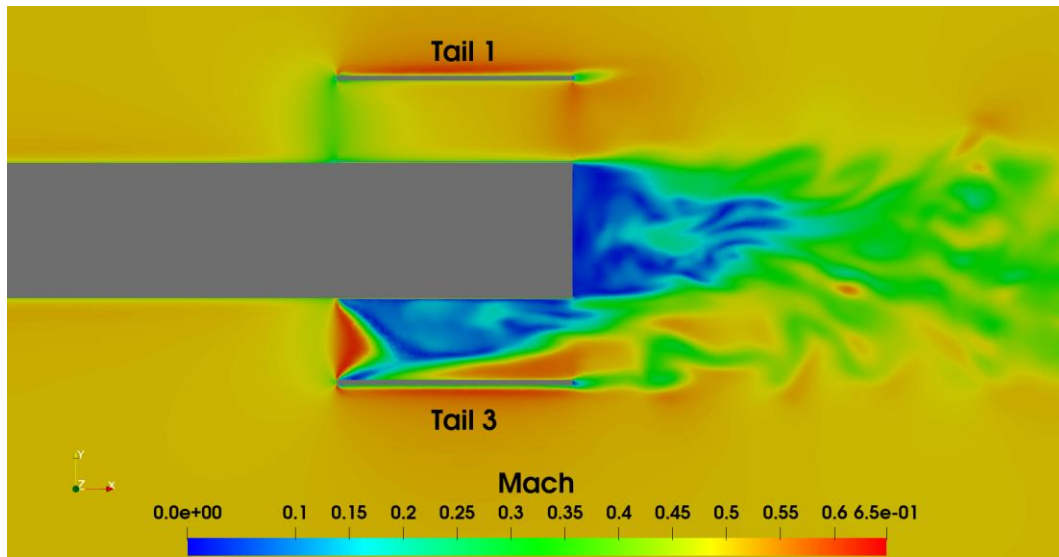


Figure 4.34: Missile with WAFs: Mach contours using DES ( $M = 0.5$ ,  $\alpha = 10^\circ$ )

In Figure 4.34, the flow separation asymmetry on Tail 3 can be seen in the Mach number contours from DES analyses. In the tip of the wrap-around fin, the flow is attached to the wall since the local angle of attack is higher with respect to midspan section on Tail 3. At different angles of attack, the asymmetric flow separation changes i.e. the shift of moment arm and center of pressure. Since this shift is different in Tail 1 and Tail 3, time averaged and instantaneous roll moments are different. For that reason, roll moment is induced and varies nonlinearly with the angle of attack.

#### 4.2.3 DDES Results of Missile with WAFs

The comparison of Roe's Approximate Riemann solver and the Exact Riemann solver is performed for a DDES case with angle of attack of  $10^\circ$ . Component based and missile based FFT spectrum is applied to explain the aerodynamic characteristics.

#### 4.2.3.1 Grid Independence Study

The integral scale of the turbulence is calculated for k- $\varepsilon$  and k- $\omega$  turbulence models as shown in Equation 76 where k is the turbulent kinetic energy,  $\varepsilon$  is the rate of dissipation of turbulent kinetic energy and  $C_\mu$  is the constant of 0.09 [33].

$$l_\varepsilon = \frac{k^{3/2}}{\varepsilon} = \frac{k^{3/2}}{C_\mu k \omega} = \frac{\sqrt{k}}{C_\mu \omega} \quad (76)$$

RANS based grid index is determined by the ratio of integral scale to the average cell size that is approximated by the cubic root of cell volume as shown in Equation 77.

$$r_{l_\varepsilon} = \frac{l_\varepsilon}{\sqrt[3]{\Delta}} = \frac{k^{3/2}}{C_\mu k \omega \sqrt[3]{\Delta}} = \frac{\sqrt{k}}{C_\mu \omega \sqrt[3]{\Delta}} \quad (77)$$

The solution domain is generated by increasing the localized volumes by four times based on the finest grid in the grid convergency study as shown in Table 4.7.

Table 4.7 Missile with WAF: Grid Independence Study for DDES Simulations

Grids	Number of Surface Cells	Number of Volume Cells	First Layer Thickness [m]	Grid Size @ Tail [m]	Grid Size @ Wake [m]	Grid Size @ Nose [m]
Finest	791652	36E+6	2E-6	2E-3	2E-3	2E-3
DDES Grid	791652	81E+6	2E-6	5E-4	5E-4	2E-3

Instead of having a locally refined region around the tails, one larger cylinder is generated to cover all the turbulent eddies around the tails as shown in Figure 4.35 and 4.36. More than 80% of the turbulent kinetic energy from the shed vortices is resolved for the regions where the RANS index is larger than 4.8.

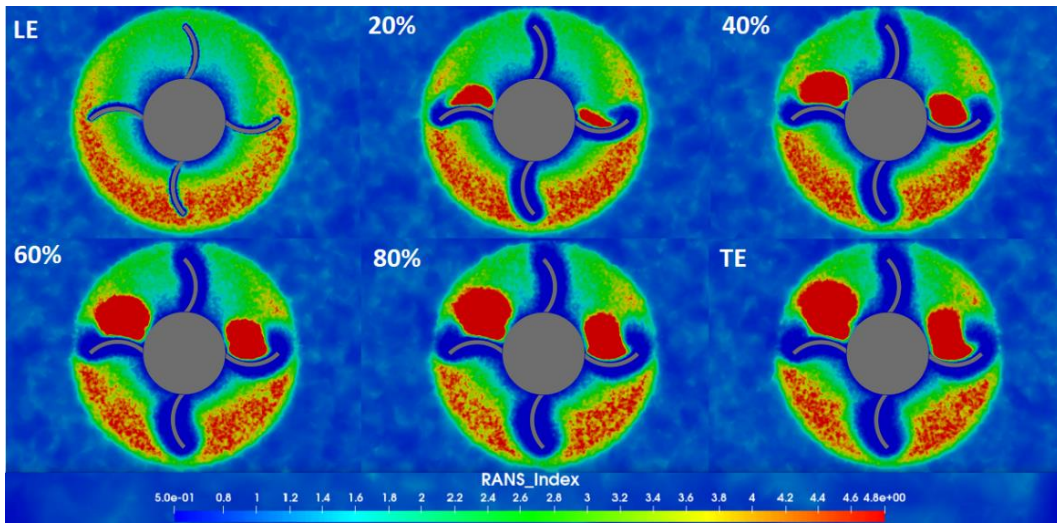


Figure 4.35: Missile with WAFs: RANS/LES index change along the tail percentage of chord from leading edge (LE) to trailing edge (TE)

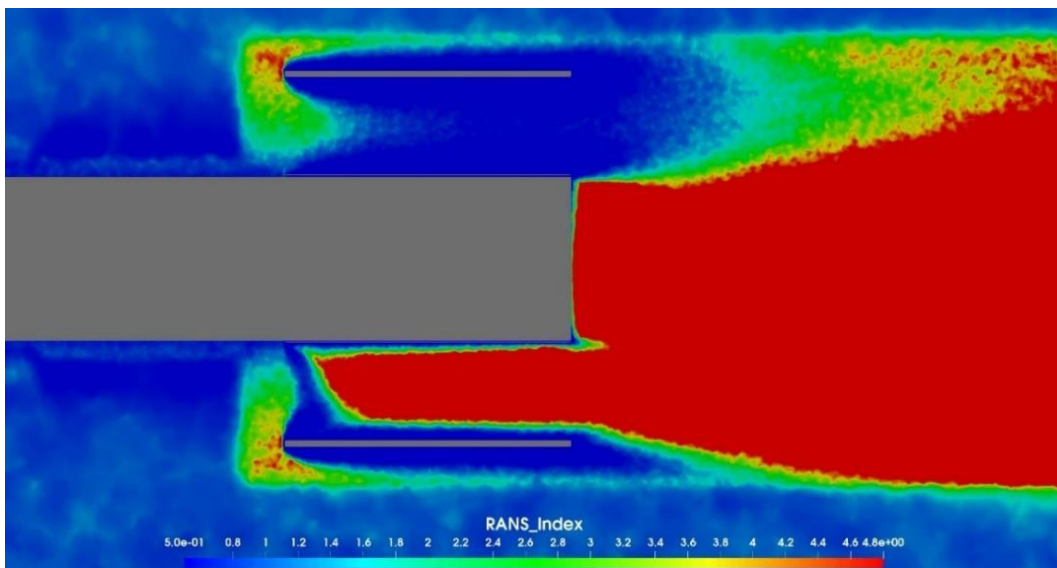


Figure 4.36: Missile with WAFs: RANS/LES index change in the wake and tail downstream at the mid-section vertical plane



### 4.2.3.2 DDES Simulations: Riemann Solvers Comparison

Since the average length of cells inside the refined volume is equal to  $5e-4$  meter, the time step is taken as  $5e-6$  for having a CFL number below unity when freestream is equal to 171 m/s. Dual time stepping with second order temporal accuracy is used with 25 inner iterations at each physical time step.

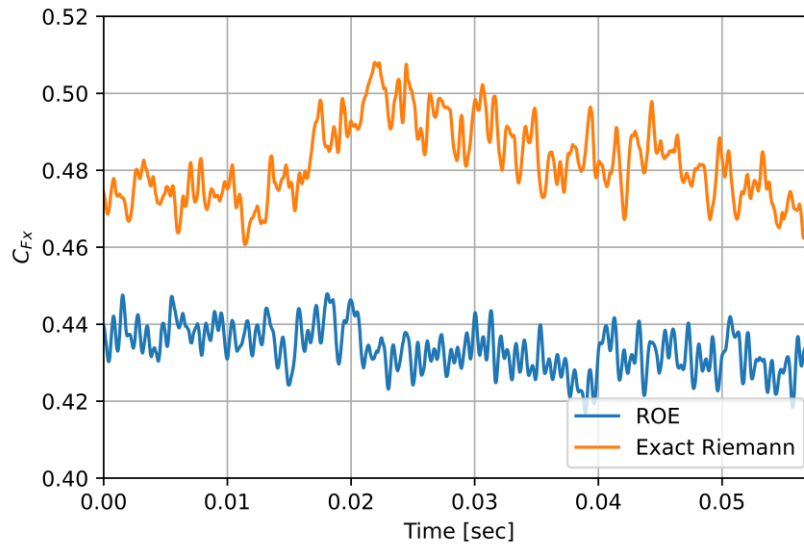


Figure 4.37: Missile with WAFs:  $C_{Fx}$  signal in time domain

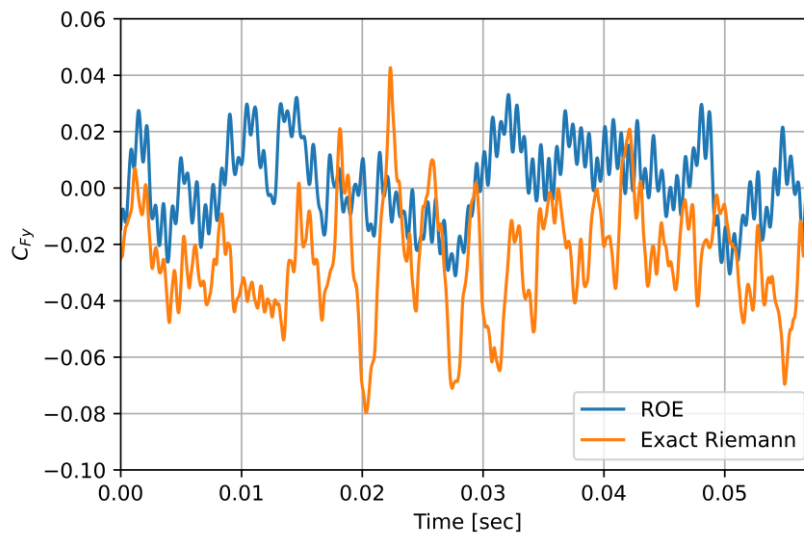


Figure 4.38: Missile with WAFs:  $C_{Fy}$  signal in time domain

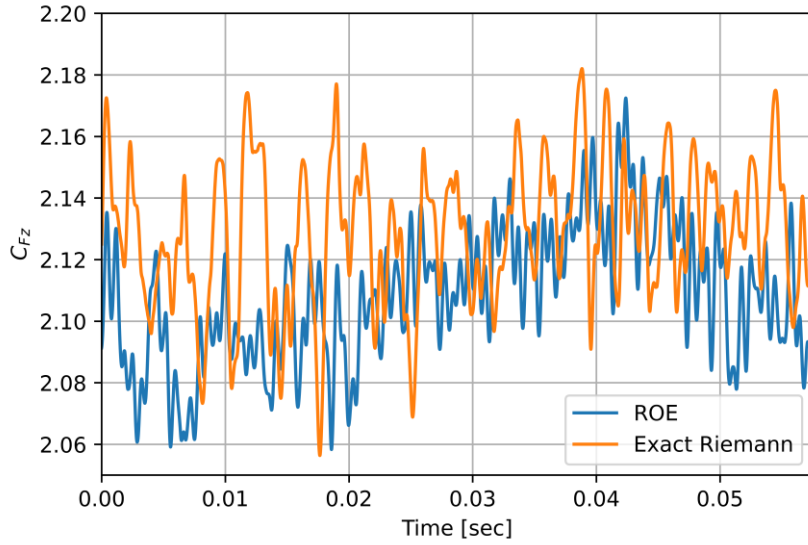


Figure 4.39: Missile with WAFs:  $C_{Fz}$  signal in time domain

17499 physical time iteration is applied for both Riemann solvers in a Delayed Detached Eddy Simulation. First 2000 iterations are omitted from the data sampling process i.e. the time required for more than one missile length. The data sampling is performed for 15499 samples with a time length of 0.0775 second that is thirteen times larger than missile length divided by the freestream velocity as shown in Figure 4.37-39.

In order to check the repeatability, FFT is performed to  $C_{Fz}$  signal by separating signal time domain into the two halves as shown in Figure 4.40 and 4.41. In the Exact Riemann (ER) solver, the peak in 0.25 Strouhal number is consistent in both halves whereas another inconsistency arises around 0.15 Strouhal number in the second half. Since they are very close to each other, the frequency resolution increase by sampling more data can change this inconsistency. On the other hand, the peaks in Roe's Approximate Riemann solver are smaller than half of the peaks in the Exact Riemann solver.

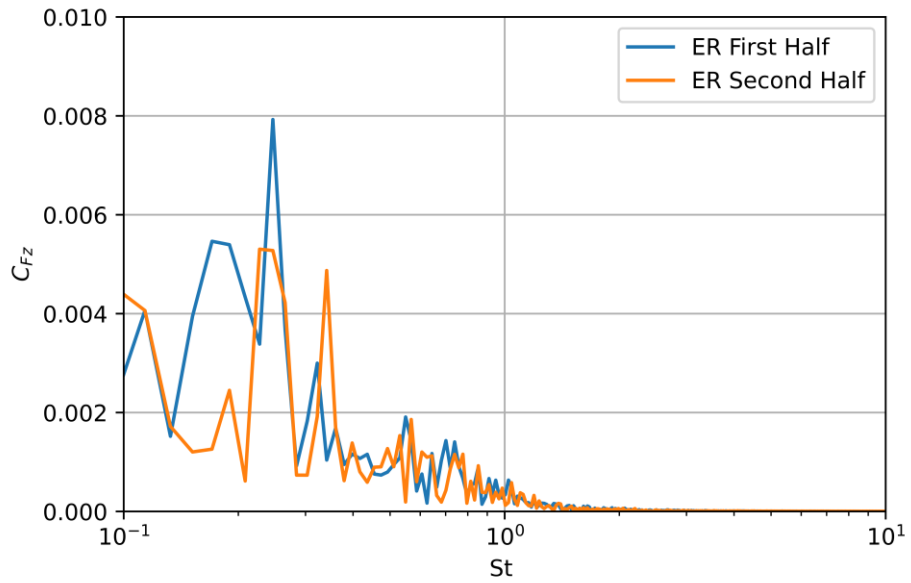


Figure 4.40: Missile with WAFs: Comparison of two halves in FFT spectrum (ER)

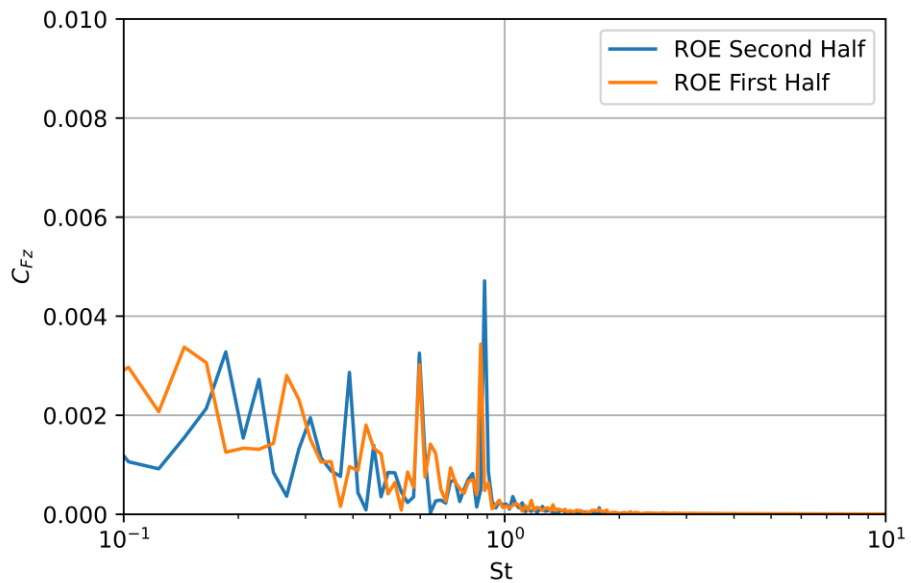


Figure 4.41: Missile with WAFs: Comparison of two halves in FFT spectrum (ROE)

The comparison of the Exact Riemann solver and Roe's Approximate Riemann solver is performed for  $C_{Fz}$  signal as shown in Figure 4.42. The consistent peak around the 0.25 Strouhal number is not shown in Roe's Approximate Riemann

solver. Due to the lack of experimental data, experimental validation is not possible from the literature. However, the distinction between Riemann solvers indicates that the harmonic frequencies in the Exact Riemann solver are smaller with a larger amplitude.

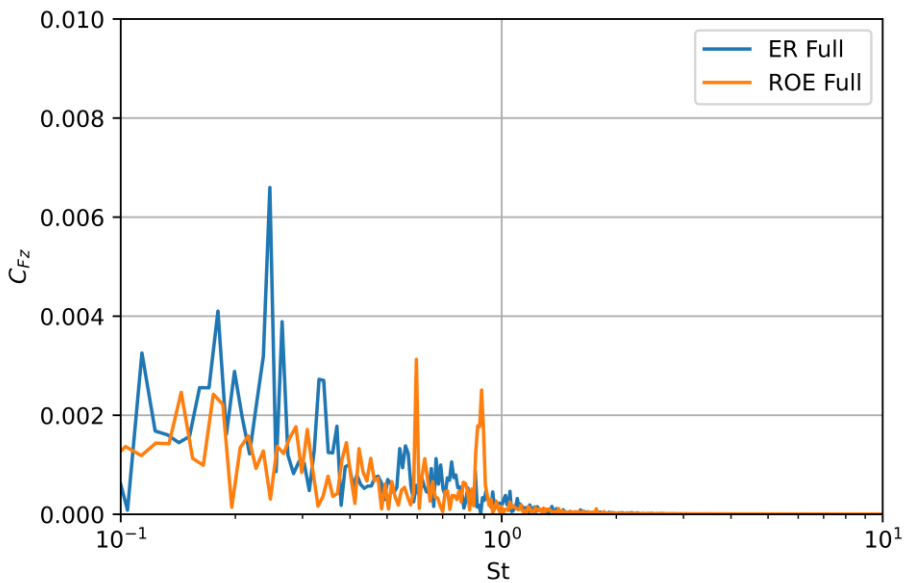


Figure 4.42: Missile with WAFs: FFT spectrum of  $C_{Fz}$  signal

The oscillations in Tail 3 is larger than Tail 1 due to the stronger shed vortices on the suction side of Tail 3 by the centralized streamlines in subsonic flow as shown in Figure 4.43 and 4.44. ROE solver has no distinctive property to calculate the flux based on the existing weak solutions. Since the weak solutions can only exist in unsteady cases for subsonic flows, the differences between the Riemann solvers changes as the unsteady effects increases. It explains why the Tail 3 has larger peaks than Tail 1 because the higher effective angle of attack causes stronger shed vortices and unsteady effects.

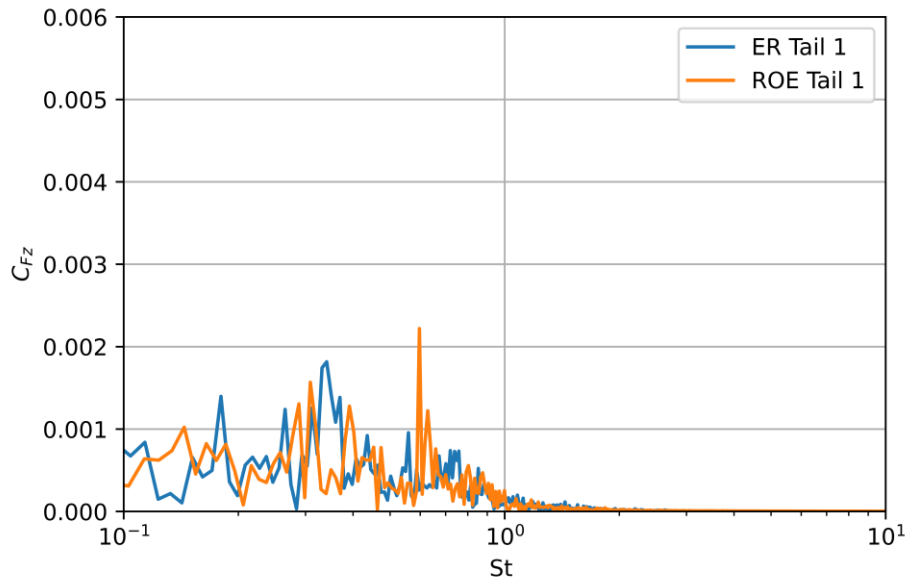


Figure 4.43: Missile with WAFs: FFT Spectrum Comparison (Tail 1)

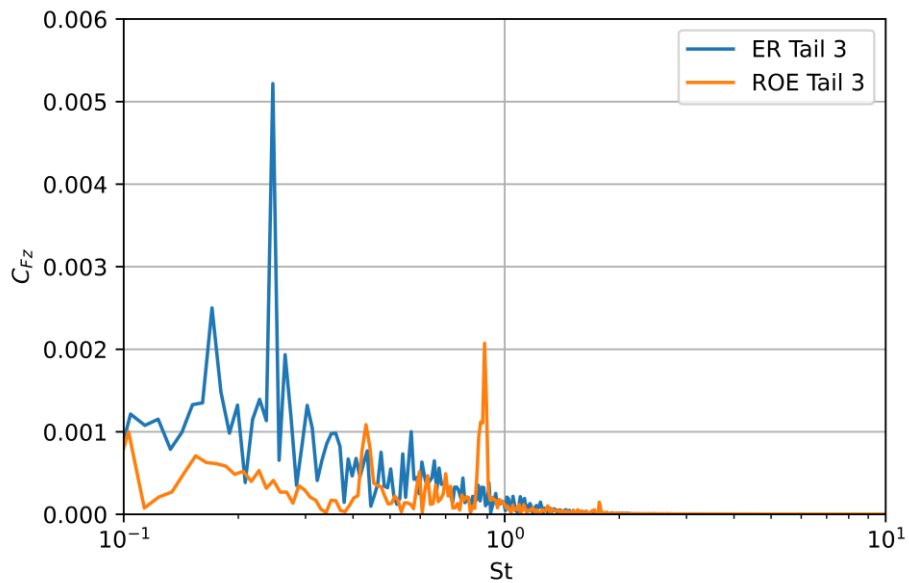


Figure 4.44: Missile with WAFs: FFT Spectrum Comparison (Tail 3)

### 4.2.3.3 DDES Simulations: Aerodynamic Interpretation

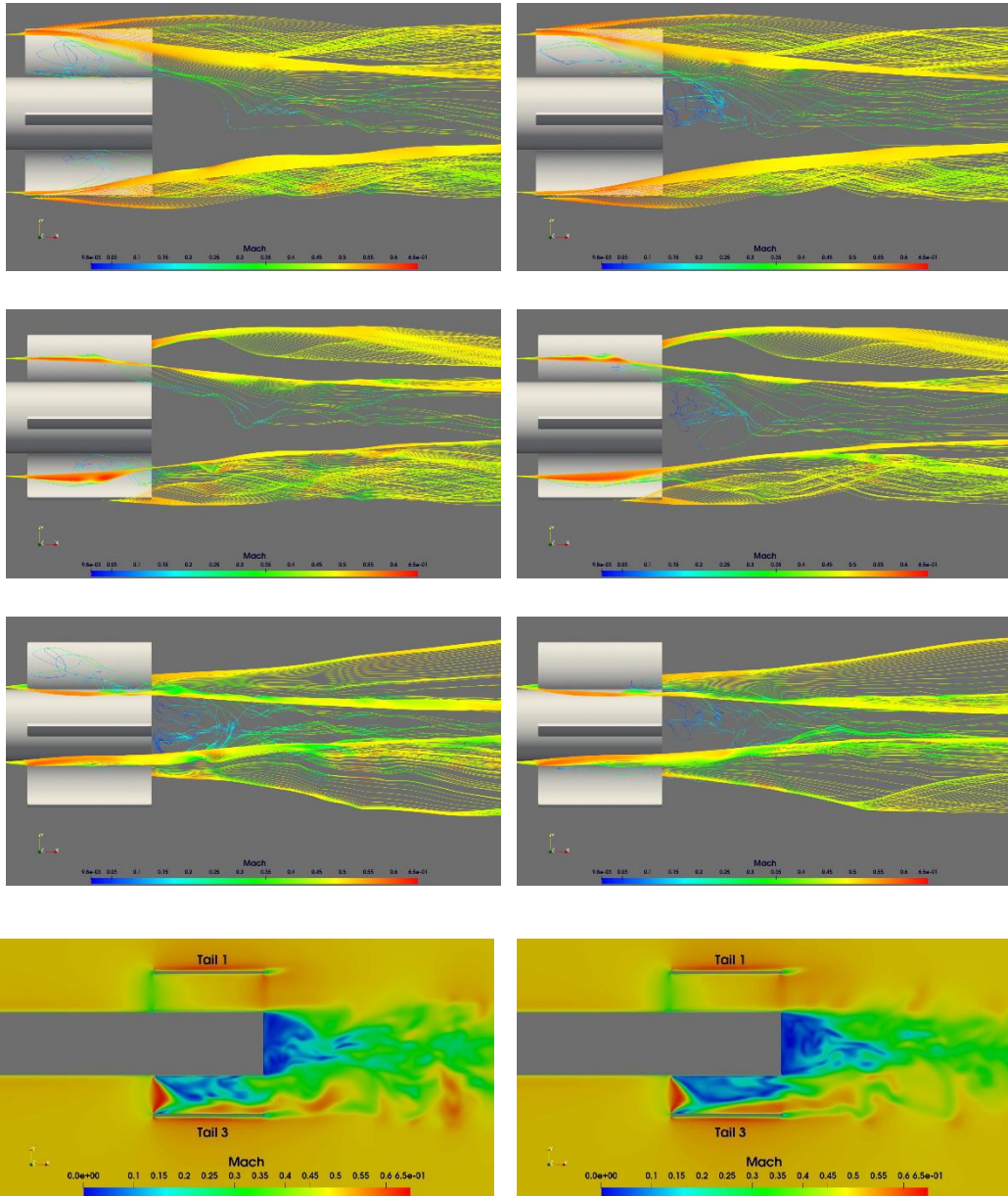
In Figure 4.47 and 4.48, the instantaneous streamlines and Mach contours around the Tail 1 and Tail 3 are shown. Since the time averaged normal force is larger on Tail

3, the tip vortices are stronger in Tail 1 than that of Tail 3. It is due to the fact that the Tail 3 has a larger effective angle of attack than Tail 1 as explained by de Laval nozzle analogy.

The wake region of the missile has low pressure region in the flow field. Since the flow under the wrap-around fin has high pressure, it causes interaction with the wake region. However, the larger tip vortex in Tail 3 causes less interaction with the wake region due to the stronger wing tip vortices in Tail 3 as shown in Figure 4.45 and 4.46.

In the root section, the difference between tails is negligible whereas it increases as going to the tip section from the root due to the dominance of the pressure gradient from the wake region for the suction section. In the pressure side, the streamlines in the root section changes their route towards the mid span because of the higher pressure in the midspan on the pressure side.

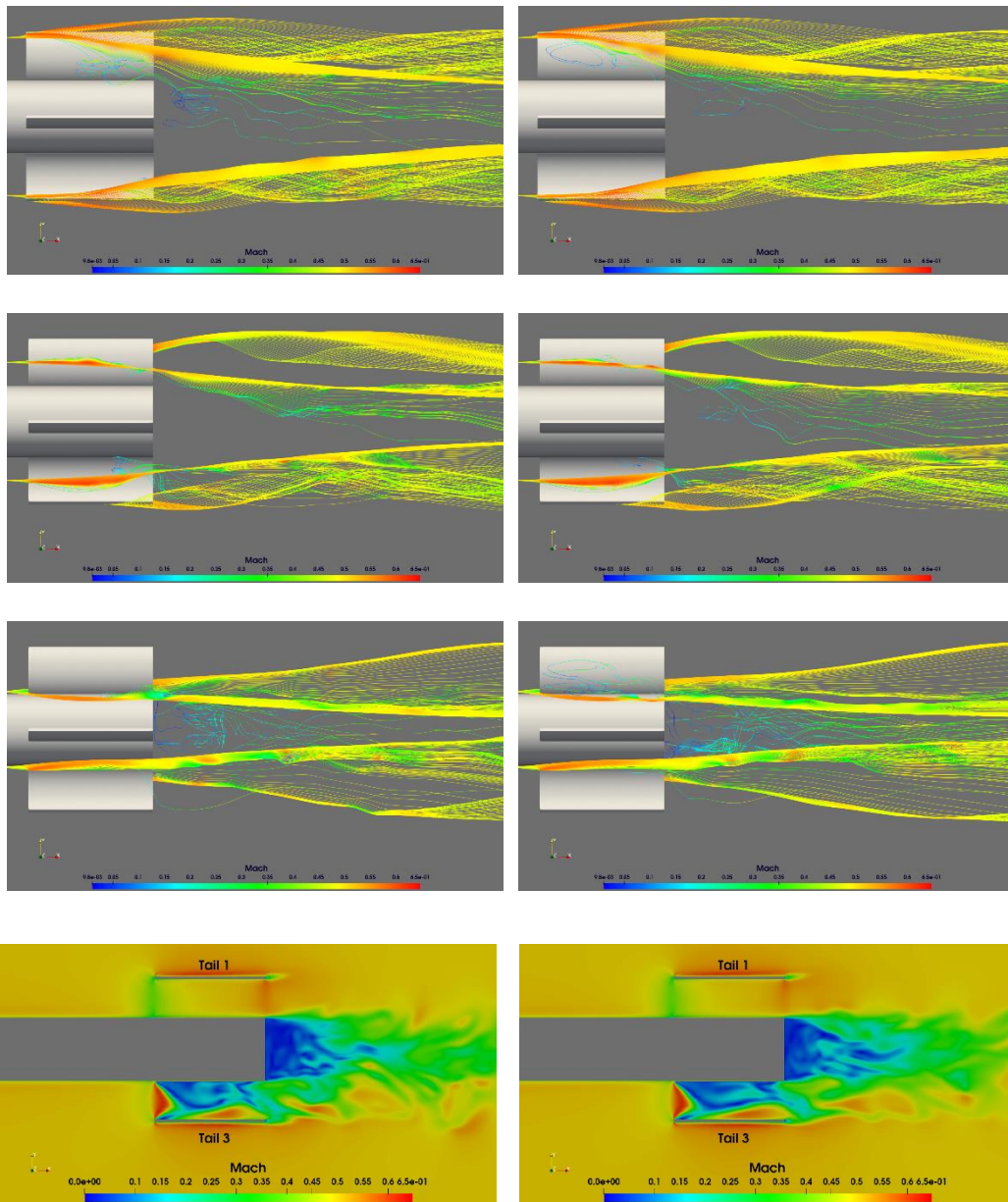
The flow separation around the midspan is more severe in Tail 3 than Tail 1. However, its interaction with the wake region is negligible unlike Tail 1 as shown in Figure 4.45 and 4.46. Instead, the separation region has more interaction with the unseparated regions closer to the tip section where the pressure gradient is larger than the wake region.



(a)  $t = 4.5e-4$  s

(b)  $t = 9e-4$  s

Figure 4.45: Missile with WAFs: Time accurate DDES Simulations: Instantaneous streamlines at  $t = 4.5e-4$  s and  $t = 9e-4$  s around the tip, mid, and root regions of wrap-around fins and Mach contours at the centerline cut plane.

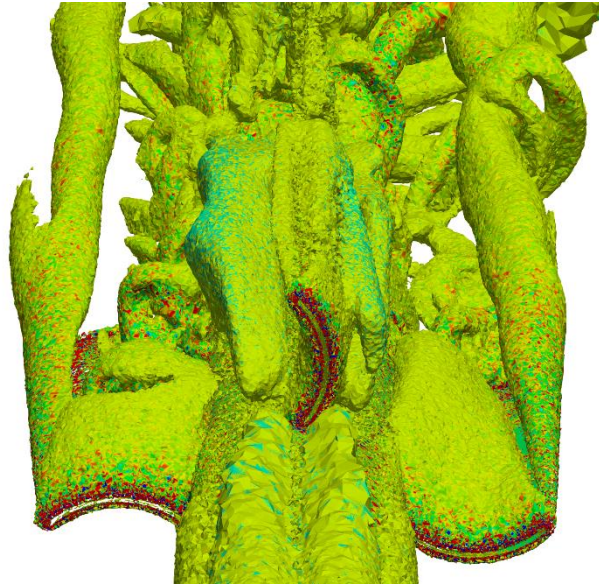
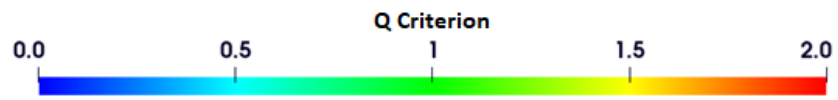


(a)  $t = 13.5e-4$  s

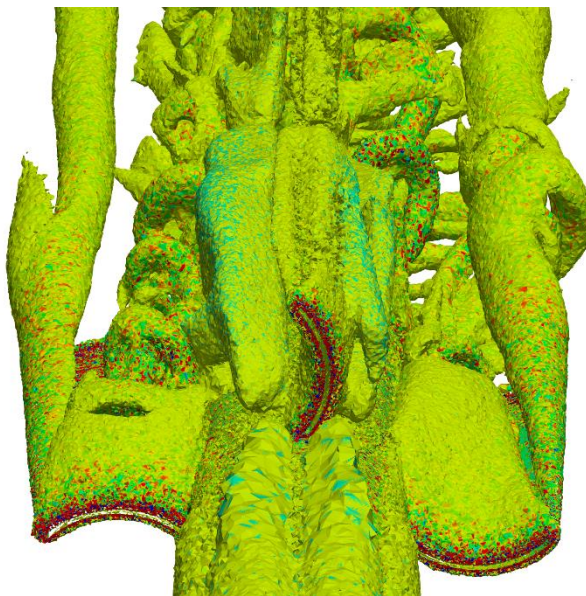
(b)  $t = 18e-4$  s

Figure 4.46: Missile with WAFs: Time accurate DDES Simulations: Instantaneous streamlines at  $t = 13.5e-4$  s and  $t = 27e-4$  s around the tip, mid, and root regions of wrap-around fins and Mach contours at the centerline cut plane.



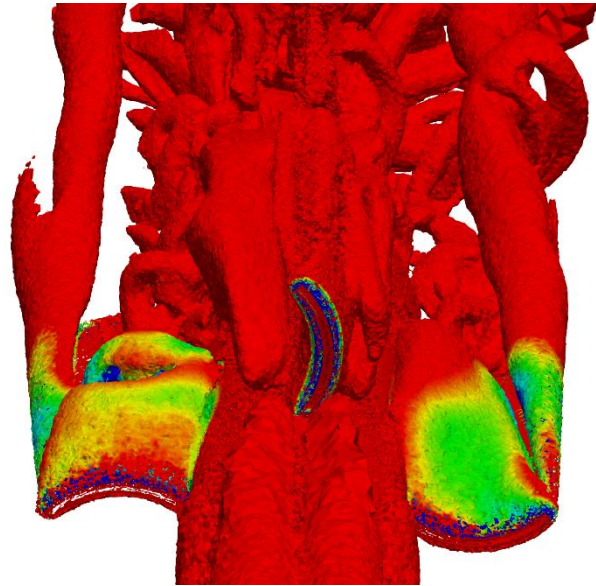
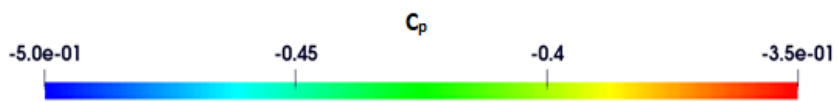


(a)  $t = 9e-4$  s

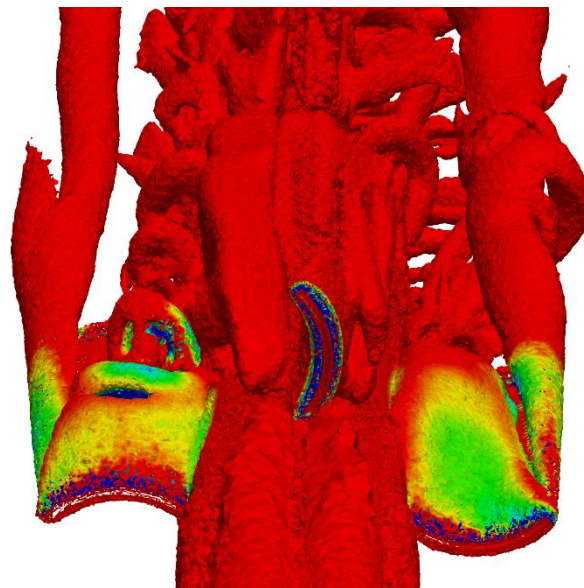


(b)  $t = 18e-4$  s

Figure 4.47: Missile with WAFs: Time accurate DDES Simulations: Instantaneous Q-criterion iso-surfaces over Tail 1 (left) and Tail 3 (right)

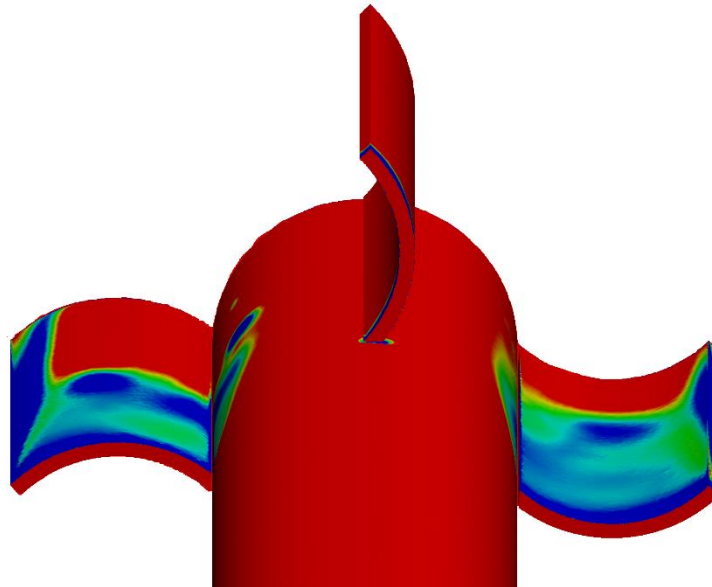
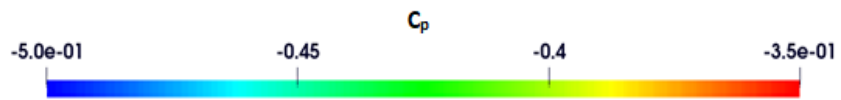


(a)  $t = 9e-4$  s

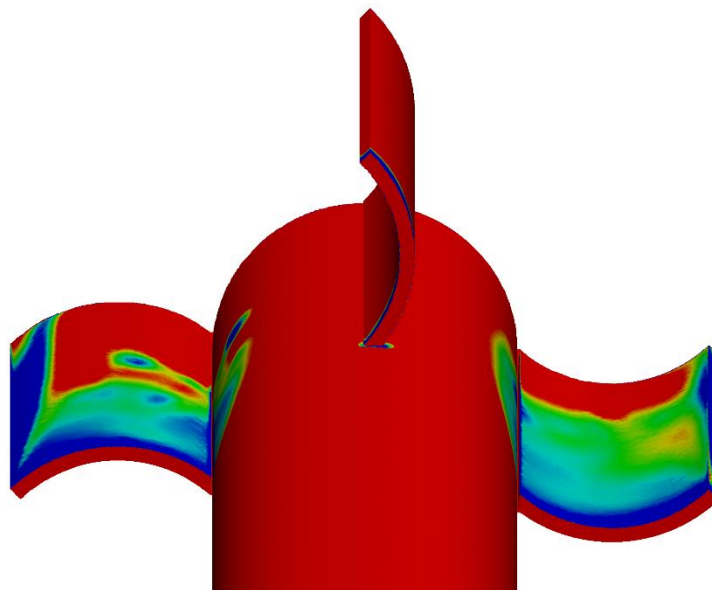


(b)  $t = 18e-4$  s

Figure 4.48: Missile with WAFs: Time accurate DDES Simulations: Instantaneous coefficient of pressure iso-surfaces over Tail 1 (left) and Tail 3 (right)



(a)  $t = 9e-4$  s



(b)  $t = 18e-4$  s

Figure 4.49: Missile with WAFs: Time accurate DDES Simulations: Instantaneous coefficient of pressure distribution over Tail 1 (left) and Tail 3 (right)

The isosurfaces are generated for DDES case for having a comparison between the tails where the flow separation and pressure distribution are different. The pressure is smaller on Tail 3 suction surface as shown in Figure 4.47 and Figure 4.48. Due to the lower pressure, the wingtip vortex size is larger on the tip of Tail 3 than that of Tail 1. In Figure 4.49, the distribution of pressure coefficient over the surfaces are shown over the tails suction side. Wrap-around fin geometry caused more pressure decrease on Tail 3 than that of Tail 1 as expected from the de Laval analogy.

#### **4.2.4 Summary and Discussions**

The roll induction mechanism is explained by RANS simulations depending on the angle of attack and freestream Mach number. The nonlinear variation of roll moment coefficient is explained by partial contribution of different tails. In order to understand the nonlinear flow separation over the wrap-around fins, DDES case is performed by both Riemann solvers for freestream Mach number of 0.5 with an angle of attack of  $10^\circ$ . The amplitudes and frequencies in the dominant modes are three times smaller in frequency and two times larger in Exact Riemann solver. Due to the absence of unsteady wind tunnel data, two unsteady validation cases are performed in the following sections for subsonic and transonic flow conditions in the next Chapter.

## CHAPTER 5

### RESULTS FOR AIRFOIL CFD SIMULATIONS

In this chapter, the results of the airfoil CFD simulations for two selected validation test cases are presented to investigate the Riemann solvers. Due to the absence of an unsteady experimental validation test case in the missile simulations, the two different unsteady validation test cases available for NACA 0021 and OAT 15A airfoils are analyzed by both ER and ROE Riemann solvers. The DDES simulation is performed for NACA 0021 airfoil in deep stall condition with angle of attack of  $60^\circ$  and Reynolds number of 270,000. The URANS simulation is performed for OAT 15A airfoil in transonic buffeting condition with angle of attack of  $3.9^\circ$  and Mach number of 0.73.

#### 5.1 NACA 0021 Airfoil in Deep Stall

Swalwell, *et al.*, [75] performed a detailed wind tunnel study with the NACA 0021 Airfoil with chord based Reynolds number of 270,000. Molina *et al.* [77] performed a DDES study with Roe's Approximate Riemann solver coupled with Ducros shock sensor to detect the weak solutions. Based on the experimental study of Swalwell, *et al.*, [75], three different grids are used to validate the average  $c_p$  over the chordwise direction and the Strouhal number based FFT spectrum of lift coefficient is compared with the DDES Results of Roe's Approximate Riemann solver and the Exact Riemann solver.

### 5.1.1 Grid Independence Study

The spanwise dimension is set to two chord length for ensuring that the largest vortical size that is equal to chord length can be resolved properly. The diameter of the cylindrical solution domain is set to 5 meter that is equal to 22 chord length approximately. The first layer cell thickness is set to  $3e-6$  meter to ensure that the  $y^+$  is kept below 1.0 along the airfoil surface. 30 viscous layers are used in the structured grid near the airfoil surface. The grid cross section and surface grid are as shown in Figure 5.1 - 5. 3.

In the grid dependency, the refinement factor of 1.5 is used in azimuthal and radial directions as shown in Table 5.1.

The grid convergency study is performed for the time average of center of pressure along the central section of the airfoil surface due to the unsteady nature of the flow conditions. Roe's Approximate Riemann solver is used in grid convergency study for computational advantage. Due to the smaller unsteady effects, the differences are smaller in the lower section of the airfoil as shown in Figure 5.4

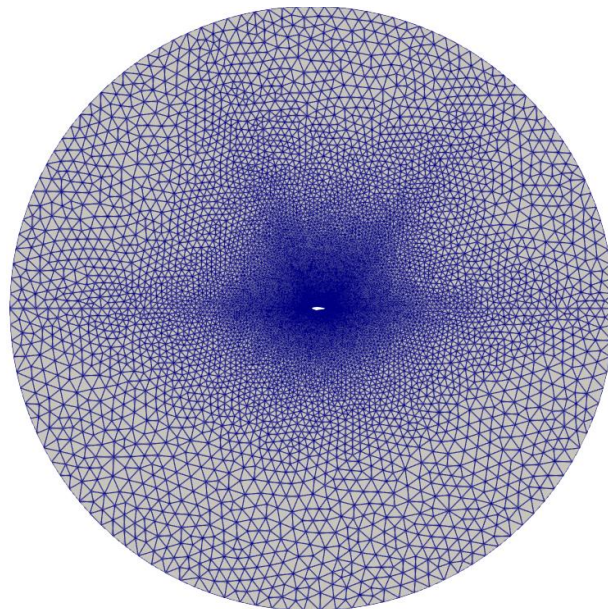


Figure 5.1: NACA 0021 Airfoil: Cylindrical Computational Domain and Unstructured Grid



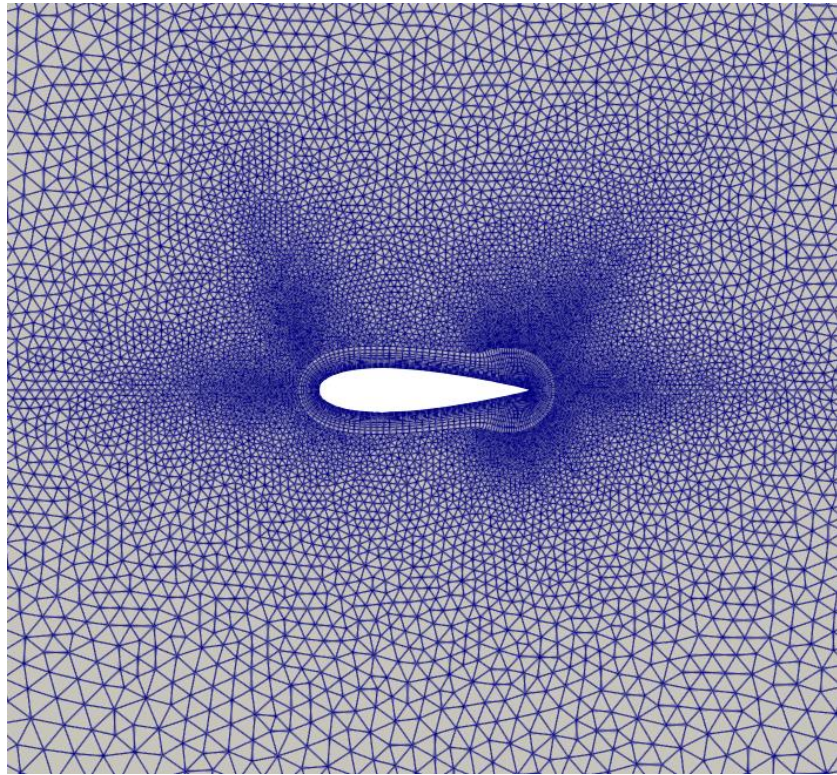


Figure 5.2: NACA 0021 Airfoil: Unstructured Grid

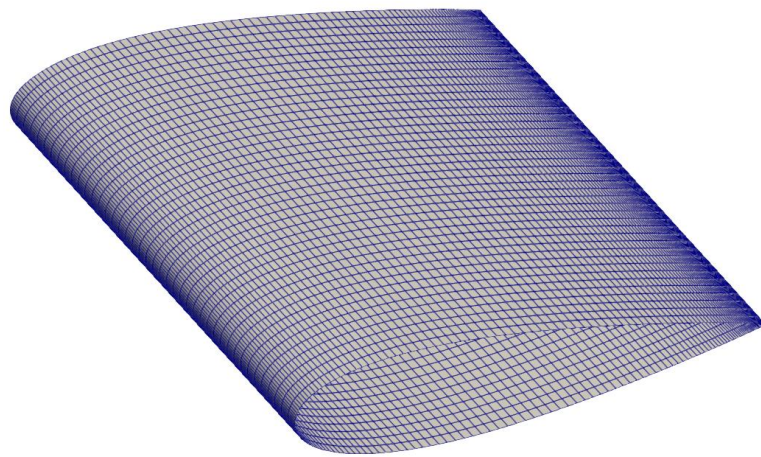


Figure 5.3: NACA 0021 Airfoil: Rectangular Surface Mesh

Table 5.1 NACA 0021 Airfoil: Grid Independence Study

Grids	Number of Grid Points $N_r$	Number of Grid Points $N_\theta$	Number of Grid Points $N_z$	First Layer Thickness [m]
Coarse	102	98	38	3E-6
Medium	151	150	38	3E-6
Fine	226	222	38	3E-6

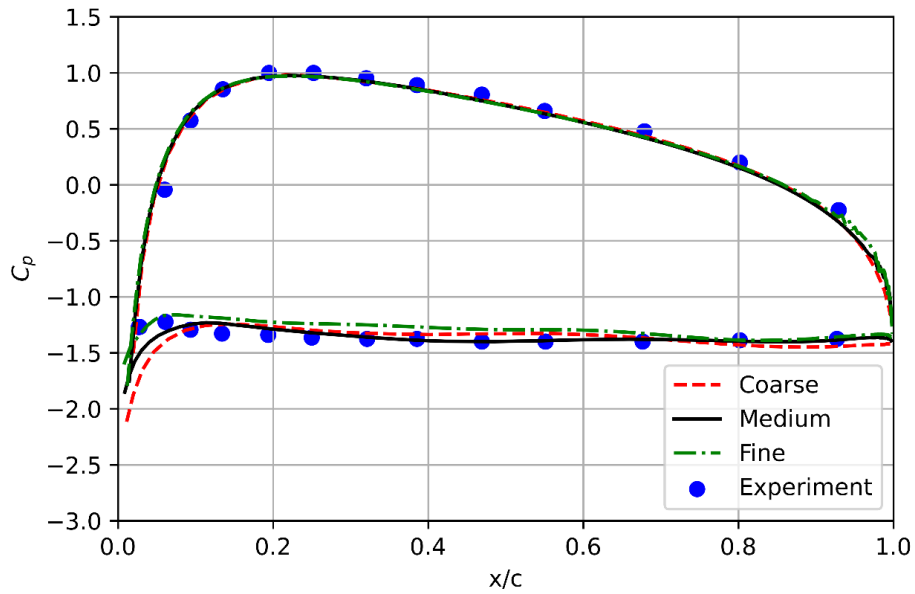


Figure 5.4: NACA 0021 Airfoil - RANS Results: Time-Averaged Pressure Coefficient Distribution



### 5.1.2 Results of DDES Simulations

DDES (Delayed Detached Eddy Simulation) case is restarted from two order converged steady RANS analysis. Dual time stepping is performed until the relative residual is decreased at least two orders. The time step is set to  $2e-6$  seconds that ensures a CFL number below one for the cells after the viscous layer and the further cells from the airfoil section. The FFT analyses are performed after 175000 iterations that is equal to physical time of 0.35 seconds as shown in Figure 5.5.

Figure 5.6 presents the frequency spectrum of the lift coefficient and their comparison with the experimental data for the Exact Riemann solver. As shown in Figure 5.6, the Exact Riemann solver could capture the first shedding frequency. However there is a gap between the amplitudes due to insufficient frequency resolution.

In order to highlight the difference between the Exact Riemann solver and Roe's Approximate Riemann solver, standard Roe scheme is used without any low dissipation function such as Ducros or Travin sensors. Although Roe's Approximate Riemann solver could capture the first and second harmonic, it is not as accurate as Exact Riemann solver in general frequency domain as shown in Figure 4.46. It can be concluded that the detected weak solutions have a larger impact as the shed vortex frequencies are getting away from the harmonics. The time averaged pressure coefficient indicates a good accuracy for both Riemann solvers as shown in Figure 5.7 and 5.8.

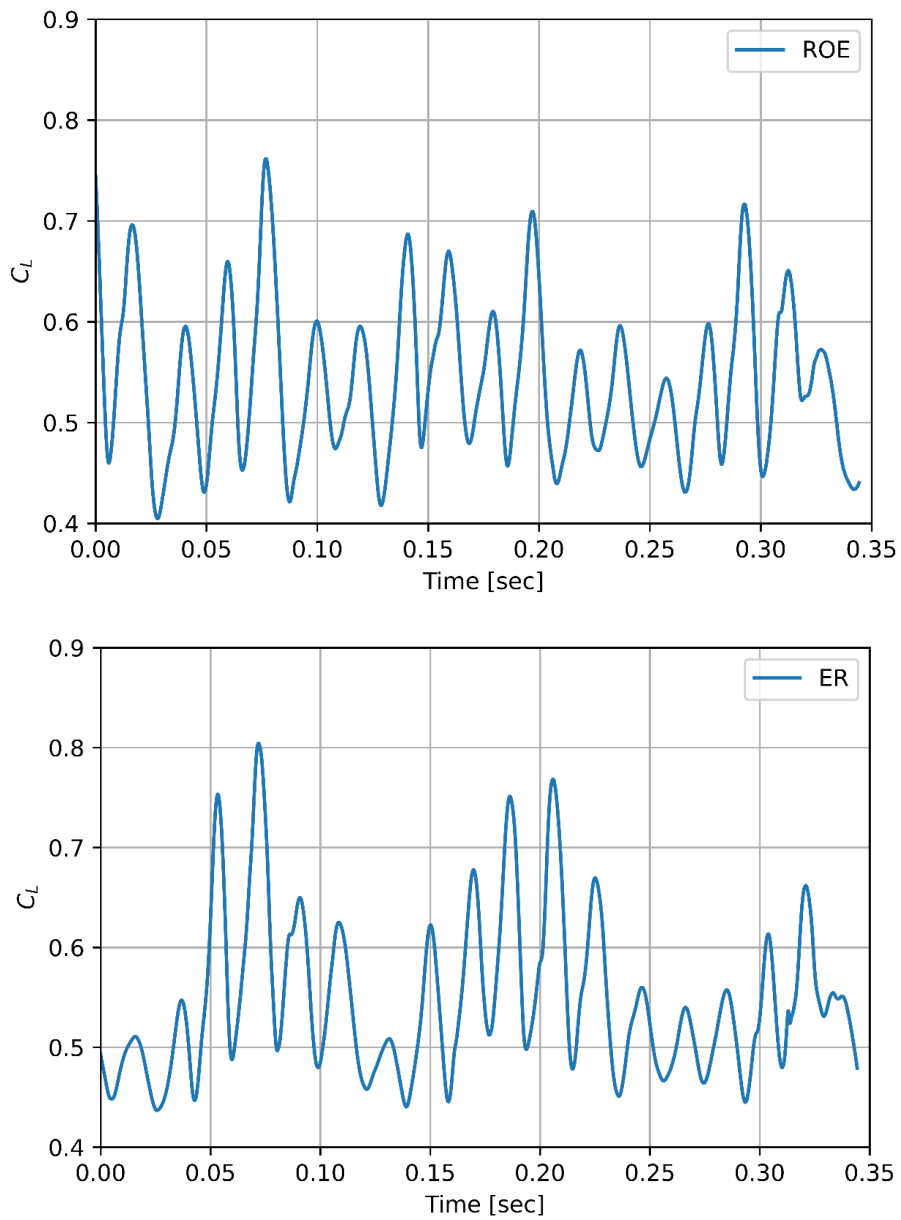


Figure 5.5: NACA 0021 Airfoil - DDES Results: Time History of Lift Coefficient using Exact Riemann (ER) and Approximate Riemann (ROE) Solvers

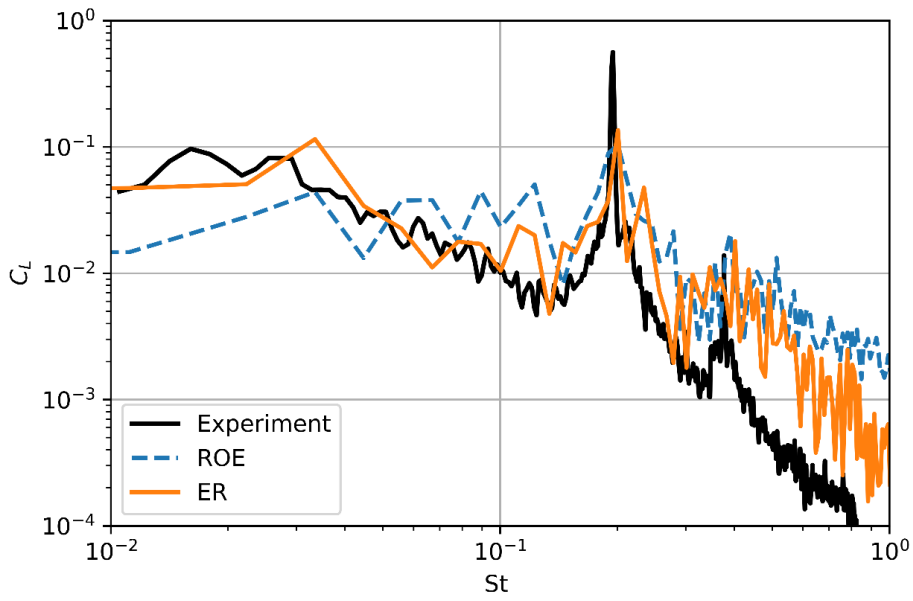


Figure 5.6: NACA 0021 Airfoil - DDES Results: FFT spectrum - Lift Coefficient vs Strouhal number (St) using Exact Riemann (ER) and Approximate Riemann (ROE) Solvers

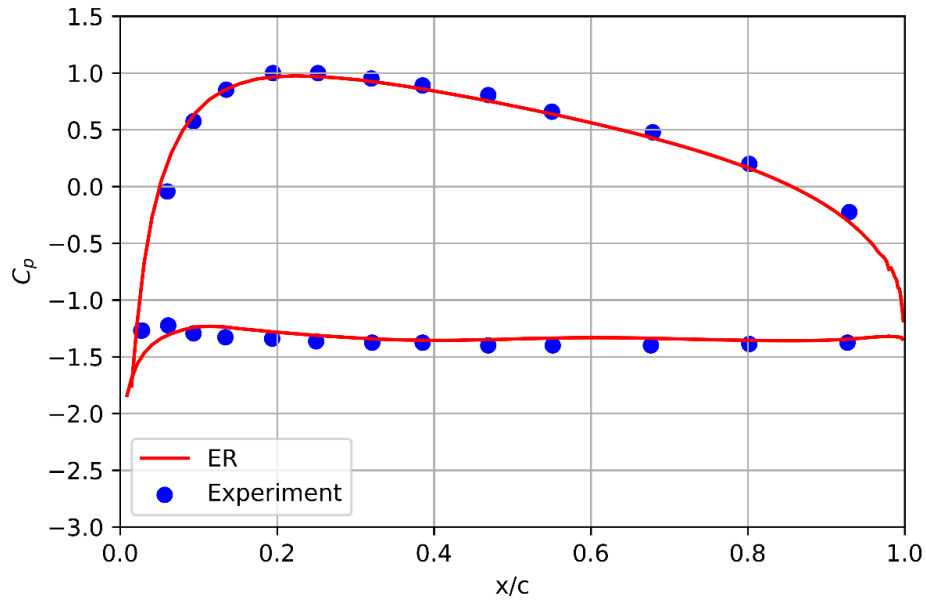


Figure 5.7: NACA 0021 Airfoil - DDES Results: Time-Averaged Pressure Coefficient Distribution using ER Riemann solver

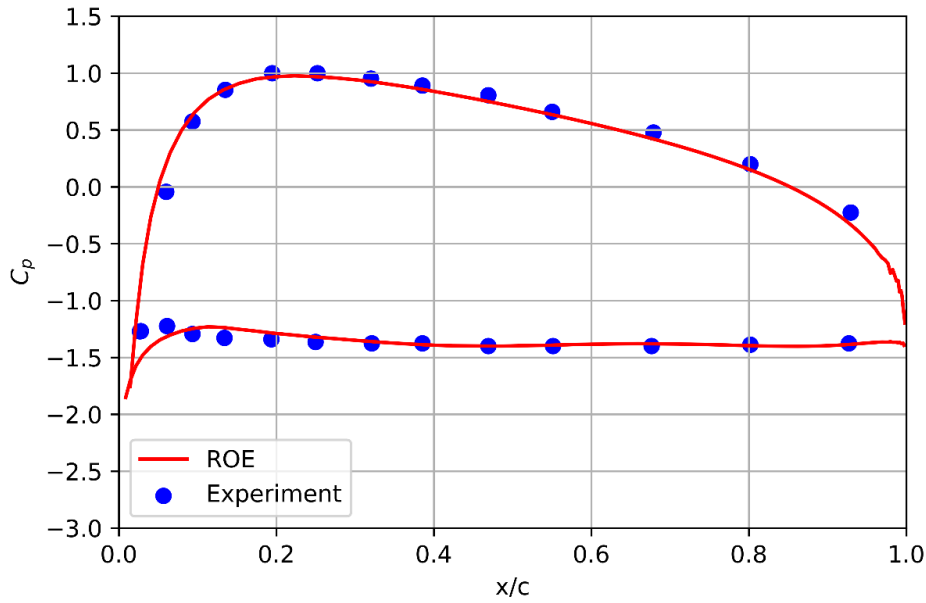


Figure 5.8: NACA 0021 Airfoil - DDES Results: Time-Averaged Pressure Coefficient Distribution using ROE Riemann solver

### 5.1.3 Computational Performance

DDES simulations are performed by using the National HPC TRUBA Supercomputing resources with the Hamsi server that contains Intel(R) Xeon(R) Gold 6258R CPU 2.70 GHz processors with 56 cores in each node. In order to avoid the disturbing effect of some instantaneous peaks due to the hardware, moving average of 5000 iterations are calculated for comparison. In Figure 5.9, the computational performance of both Riemann solvers showed that the average computational time of Exact Riemann solver is 1.8 – 1.9 times longer than Roe’s Approximate Riemann solver as expected from Toro’s results in the literature [31].

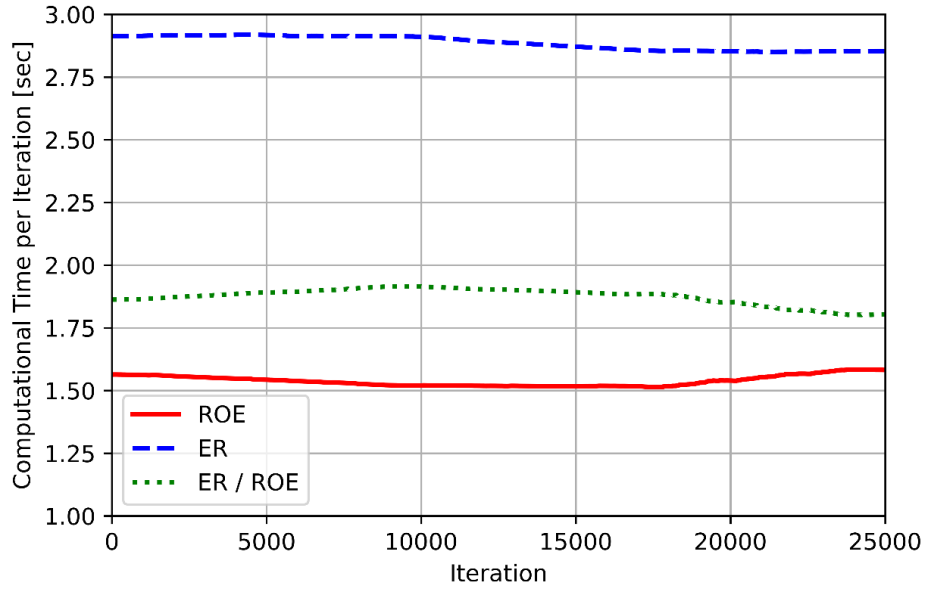


Figure 5.9: NACA 0021 Airfoil - DDES Results: Computational Performance of ER and ROE Methods by taking moving-average of 5000 iterations

## 5.2 OAT 15A Airfoil in Transonic Flow

Joacquin *et al.* [80] performed a set of wind tunnel tests for analyzing the unsteady transonic buffeting due to the shock boundary layer interaction at high subsonic flow conditions. Since Einfeldt [30] mathematically proved that the difference between approximate and exact Riemann solvers increases in low density and transonic flows, this transonic case at Mach number of 0.73 is chosen as the unsteady configuration test case.

### 5.2.1 Grid Independence Study

A two dimensional test case is used in a grid convergence study for the selection of grid that is used in URANS case for unsteady validation. The diameter of the cylindrical solution domain is set to 9.2 meter that is equal to 40 chord length as also implemented by Molina *et al.* [77]. The first layer cell thickness is set to  $3e-6$  m to ensure that the  $y^+$  is kept below 1.0 along the airfoil surface similarly as shown in

Table 5.1. The cell sizes are decreased by the factor of 0.7 that gives a number of cell increase as a factor of 2.0 between consecutive grids. Since the number of viscous layers are different in each cell for having an area ratio close to 1.0, the exact cell size of grids are not precisely equal to 2.0 as shown in Figure 5.10- 5.11.

The grid convergency check is used for the grids listed in Table 5.2. In the simulations  $k-\omega$  SST turbulence model is used with CFL number of 20.0 for all cases. The converged lift and drag coefficients have a discrepancy less than 0.3% as shown in Table 5.3. The residuals decrease up to 4-5 orders depending on the grid size as shown in Figure 5.12.

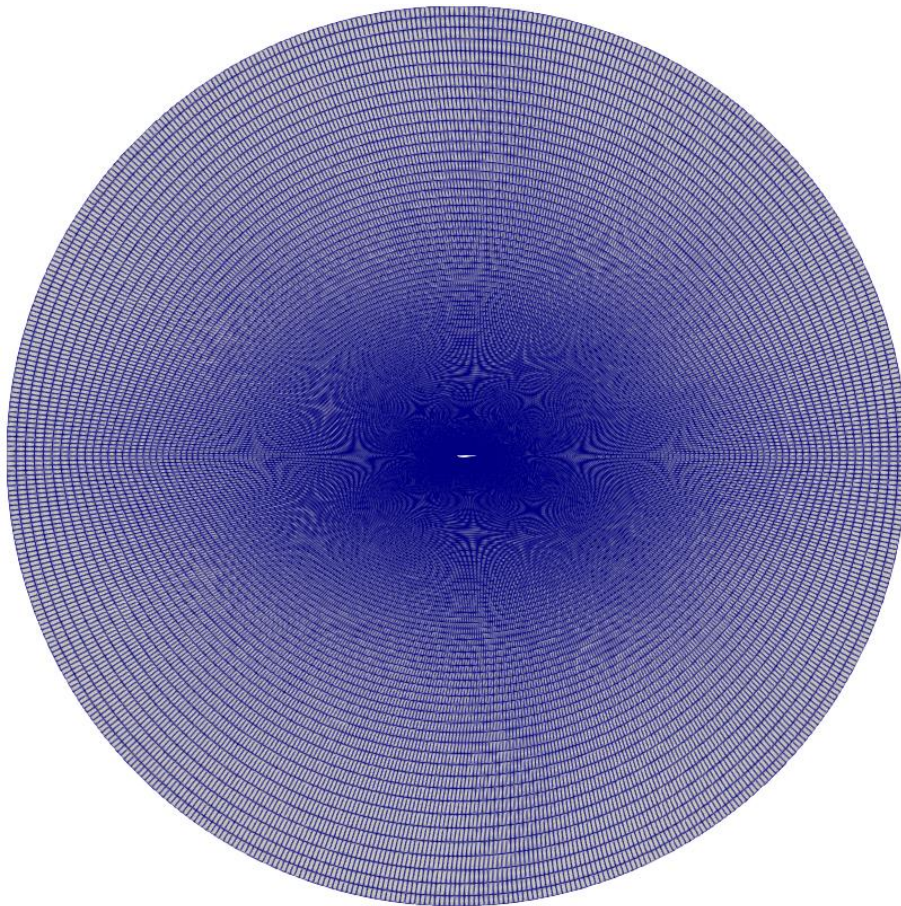


Figure 5.10: OAT 15A Airfoil: Computational Domain and Structured Grid

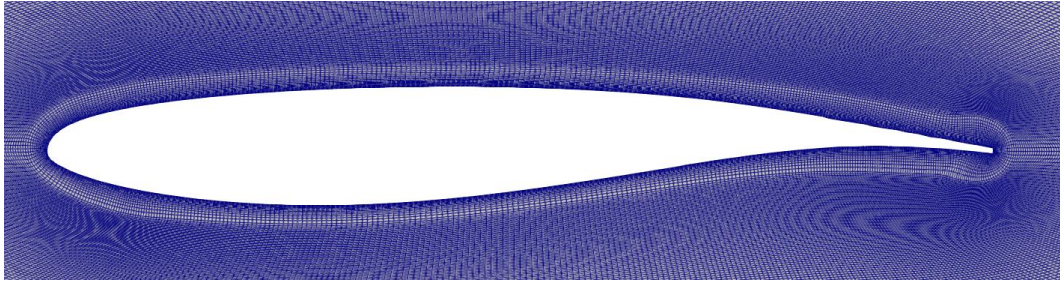


Figure 5.11: OAT 15A Airfoil: Structured O-Grid around the Airfoil

Table 5.2 OAT 15A Airfoil: Grid Independence Study for RANS Simulations

Grids	Number of Grid Points $N_r$	Number of Grid Points $N_\theta$	First Layer Thickness [m]
Coarse	304	570	3E-6
Medium	430	805	3E-6
Fine	583	1142	3E-6

Table 5.3 OAT 15A Airfoil - RANS Results: Aerodynamic Coefficients

Grids	$C_L$	$C_D$
Coarse	1.032614	0.056098
Medium	1.032614	0.056112
Fine	1.031511	0.056182

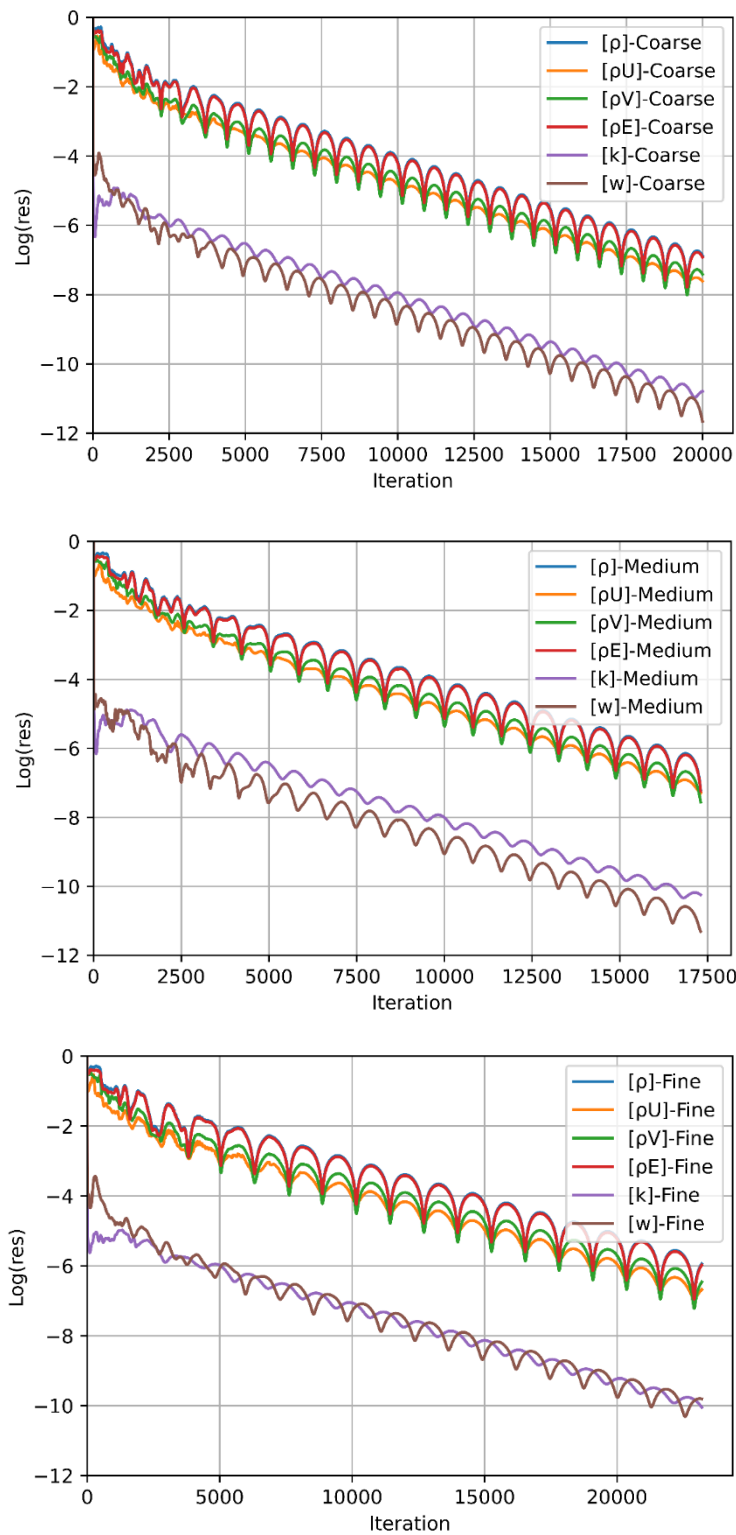


Figure 5.12: OAT 15A Airfoil - RANS Results: Residual Plots for the Coarse, Medium, and Fine Grids



### 5.2.2 Results of URANS Simulations

In the wind tunnel experiment campaign, Joacquin *et al.* [80] focused to find the starting angle of attack for transonic buffeting. It is reported that the unsteady oscillatory behavior is observed after an angle of attack of  $3.5^\circ$ . In order to check that the flow has unsteady conditions, angle of attack of  $3.9^\circ$  case is selected for validation. The grid is generated from the fine grid with 692000 cells by a refinement factor 1.41 in both radial and azimuthal directions. In URANS case a time step of  $5e-7$  second is applied. The time average pressure coefficients and the unsteady pressure measurement from 45% of the chord axis on the upper side is published by Joacquin *et al.* [80].

The time average of pressure coefficients shows no discrepancy with experimental data for both Exact Riemann (ER) solver and Roe's Approximate (ROE) solver as shown in Figure 5.13.

Pressure measurement is performed by many points on the upper section of the airfoil. Numerical pressure sensor is added to that point on SU2 CFD cases for comparing the pressure with the experimental data. The time data of the signal is selected to between the local minima position in order to minimize the spectral leakage between harmonics as shown in Figure 5.14.

As shown in Figure 5.16, the fundamental frequencies are expected to be close to each other. The damping amplitude of URANS from steady RANS solution are also close. For that reason, FFT analysis is performed to compare the possible difference in the frequency spectrum. Since the frequency of the other harmonics are not known, Hanning windowing function is applied to the signals for FFT analysis. As expected from the time history, there is no notable difference between Riemann solvers as shown in Figure 5.15.

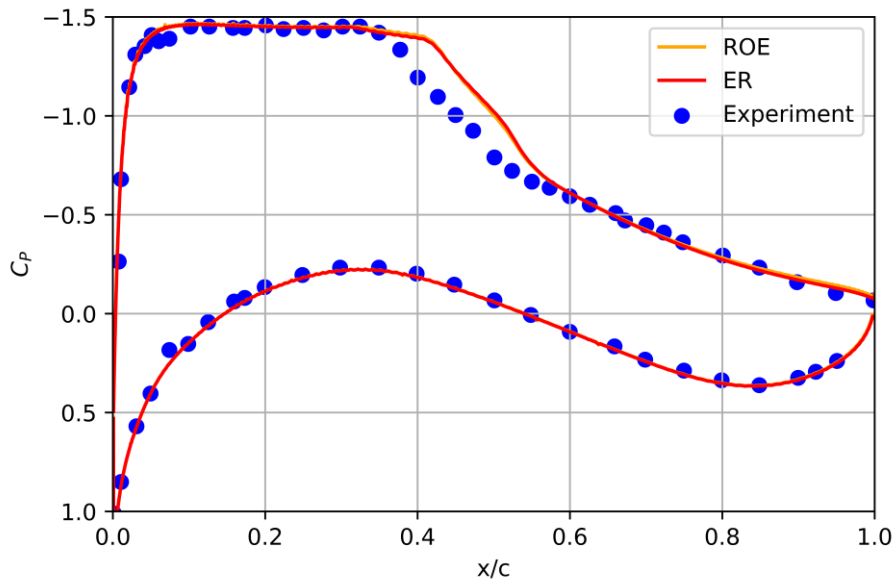


Figure 5.13: OAT 15A Airfoil - URANS Results: Time-Averaged Pressure Coefficient Distribution at  $M = 0.73$  and  $\alpha = 3.9^\circ$

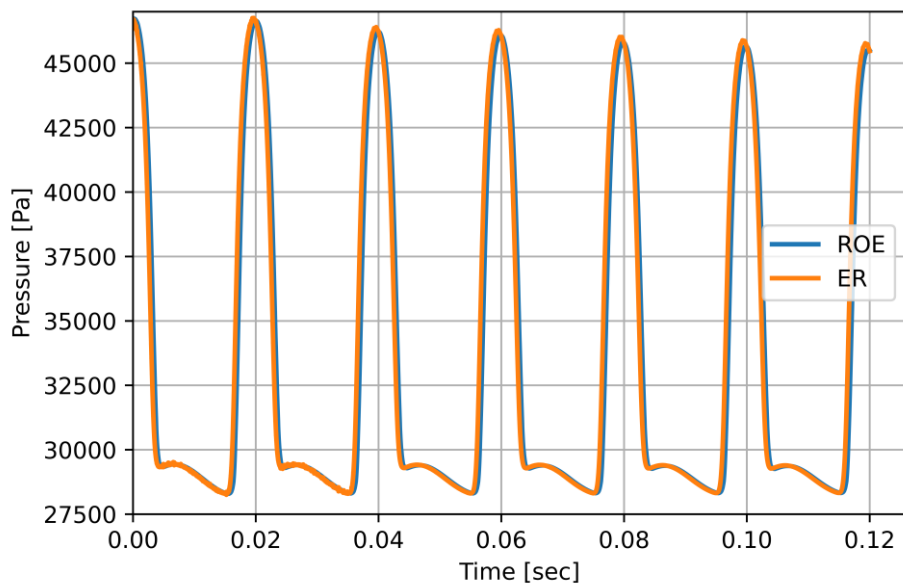


Figure 5.14: OAT 15A Airfoil - URANS Results: Time History of Pressure at the pressure sensor

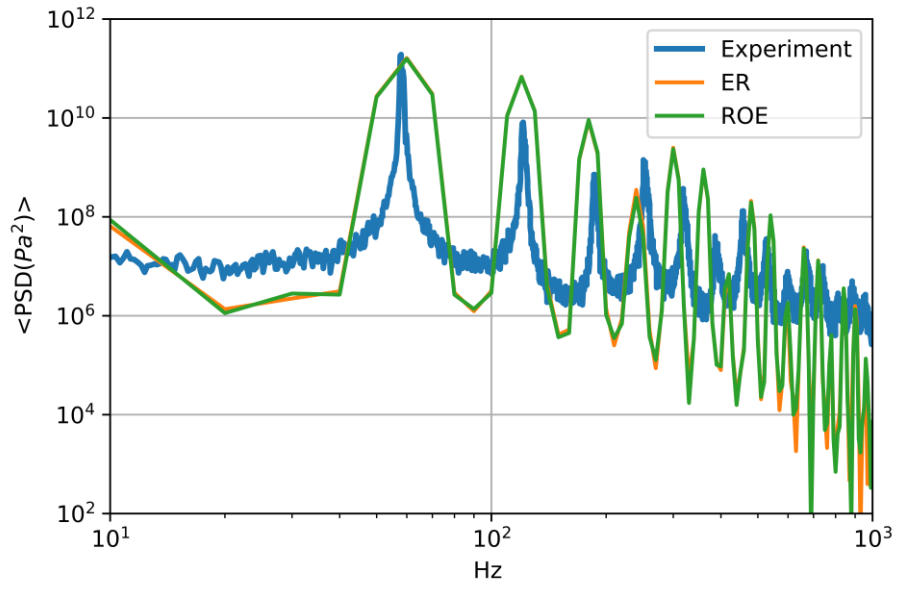


Figure 5.15: OAT 15A Airfoil - URANS Results: Power Spectral Density (PSD) of Pressure at the pressure sensor



## CHAPTER 6

### CONCLUSIONS

Roll induction for missiles with wrap-around tail fins is numerically investigated by using SU2 flow solver. In subsonic flow, the curvature of wrap-around tail induces a roll moment by centralizing and decentralizing subsonic streamlines around the fin's concave and convex side, respectively. The shift of direction occurs in supersonic flow since the concave side causes stronger shock wave than that of convex side.

The roll induction mechanism for wrap-around fin missiles are aerodynamically explained in terms of Mach number and angle of attack. In order to investigate the effect of flux scheme, Roe's Approximate Riemann solver is compared with the in house implemented Exact Riemann (ER) solver. The differences are less than 1% for most of the steady-state RANS simulations. The results indicated that the turbulence model have more significant differences in aerodynamic coefficients than the flux scheme. In subsonic flow, the  $k-\omega$  SST model has less discrepancy with the experimental results than that of Spalart-Allmaras model. On the other hand, Spalart-Allmaras model has less discrepancy in transonic flow.

On the other hand, DDES simulation showed that the differences between Riemann solvers in unsteady flow cause important changes in harmonics in terms of both amplitude and frequency. In the absence of experimental unsteady validation, the differences between Riemann solvers are investigated by a DDES campaign for solver comparison in Dahlke geometry. Although the time average aerodynamic coefficients differences are within the range of 5% and 2% for axial and normal force coefficients respectively, the differences in the FFT spectrum showed that the Exact

Riemann solver is able to detect the harmonics with two times larger amplitude in the Strouhal numbers between 0.2 and 0.3.

Due to the absence of unsteady experimental validation data for the Dahlke geometry and basic finner geometry, NACA 0021 and OAT 15A airfoil profiles are used as test cases for unsteady validation and verification.

In NACA 0021 simulations, three dimensional DDES simulation is performed for an angle of attack of  $60^\circ$ . The Exact Riemann solver has less discrepancy in the first harmonic amplitude whereas there is no peculiar difference in the second harmonic between the Riemann solvers. In addition, the Exact Riemann solver has less discrepancy with the experimental data in the overall frequency domain due to the identification of wave types in flux calculation. On the other hand, there is no particular difference between the time average of local pressure coefficients.

In OAT 15A simulations, two dimensional URANS simulation is performed for an angle of attack of  $3.9^\circ$  and a freestream Mach number of 0.73. In this case, the shockwave on the suction side of the airfoil has an oscillatory nature that is observed and measured by wind tunnel experiments. There is no distinctive discrepancy in the time averaged pressure coefficients and the power spectral density of the pressure sensor that is located 45% of chord length on the suction side for both Riemann solvers.

There are three contributions to the literature in this thesis. The first one is the aerodynamic interpretation of roll moment induction for wrap-around fin missiles. Although the roll induction is explained in the literature [2, 5], the nonlinear behavior of roll moment against varying angle of attack is examined by decomposing the roll moment contributions of each wrap-around fin in this thesis.

The second one is the comparison of the effect of flux schemes and turbulence models on the induced roll moment at neural flight angles with varying Mach numbers in steady RANS cases. The results are compared with the wind tunnel tests. In spite of its computational cost, the Exact Riemann solver shows the smaller

discrepancy with the test data compared to Roe's Approximate Riemann solver but differences are within the range 1-2% in RANS cases.

The third one is the comparison of Riemann solvers in DDES and URANS cases. Unlike small differences between Riemann solvers in time averaged results, the distribution of dominant modes are significantly different. It might be due to the fact that Roe linearizes the Riemann problem around the two rarefaction solution whereas the Exact Riemann solver identifies the shockwaves to calculate the flux accordingly.

In future, the sensor capability of the Exact Riemann solver is going to be used for setting the flux limiter for preventing numerical oscillations. In addition, DDES simulations is going to be extended larger angle of attack to have a better understanding of dominant modes for wrap-around fin missiles. In the NACA 0021 validation case, the DDES simulations is going to be extended to illustrate the effect of grid in the frequency domain as well as the different angles of attack. In addition, the OAT 15A airfoil case can be repeated for a three dimensional DDES simulation for having a better comparison between Riemann solvers.





## REFERENCES

- [1] Dahlke, C.W. and Flowers, L.D., "The Aerodynamic Characteristics of Wrap-around Fins, including Fold angle at Mach numbers from 0.5 to 1.3" U.S. Army Missile Research and Development Command, Redstone Arsenal, Alabama, TR-RD-75-19, AD-A009-735, 1974.
- [2] Holmes, J.E., "Wrap-around Fin Pressure Distribution", Naval Ordnance Laboratory, 73-107, 1973.
- [3] Lucero, E.F., "Aerodynamic Stability and Control Characteristics at High Subsonic Speeds of Configurations Incorporating Wrap-around Surfaces", AIAA-76-366, 9th Fluid and Plasma Dynamics Conference, San Diego, CA, USA, 14-16 July 1976.
- [4] Eastman, D.W. and Wemndt, D.L., "Aerodynamics of Maneuvering Missiles with Wrap-around Fins", AIAA-85-4083, AIAA 3rd Applied Aerodynamics Conference, Colorado Springs, CO, USA, 14-16 October 1985.
- [5] Winchenbach, G.L., Buff, R.S., Whyte, R.H. and Hathaway, W.H. "Subsonic and transonic aerodynamics of a wraparound fin configuration", *Journal of Guidance, Control, Dynamics*, Vol. 9, No. 6, pp. 627-632, 1986.
- [6] Abate, G.L., and Winchenbach, G.L., "Aerodynamics of Missiles with slotted configurations", AIAA-91-0676, AIAA 29th Aerospace Sciences Meeting, Reno, NV, USA, 07-10 January 1991.
- [7] Vitale, R.E., Abate, G.L., Winchenbach, G.L., and Riner, W., "Aerodynamic Test and Analysis of a Missile Configuration with Curved Fins", AIAA-92-4495, AIAA Astrodynamics Conference, Hilton Head Island, SC, USA, 10-12 August 1992.
- [8] Swenson, M.W., Abate, G.L., and Whyte, R.H., "Aerodynamic Test and Analysis of Wrap-around Fins at Supersonic Mach Numbers Utilizing Design of Experiments", AIAA-94-0200, 32nd AIAA Aerospace Sciences Meeting and Exhibit, Reno, NV, USA, 10-13 January 1994.

- [9] Tilmann, C.P., Huffman, R.E.Jr., Buter, T.A., and Bowersox, R.D.W., “Characterization of the flow structure in the vicinity of wrap-around fin at supersonic speeds”, AIAA-96-0190, AIAA 34<sup>th</sup> Aerospace Sciences Meeting and Exhibit, Reno, NV, USA, 15-18 January 1996.
- [10] Mandić, S., “Analysis of the Rolling Moment Coefficients of a Rocket with Wrap-around Fins”, *Scientific-Technical Review*, Vol 56, No. 2, pp. 30-37. 2006.
- [11] Bar-Haim, B. and Seginer, A., “Aerodynamics of Wraparound Fins”, *Journal of Spacecraft*, Vol 20, pp. 339-345, July-August 1983.
- [12] Abate, G.L. and Cook, T., “Analysis of Missile Configurations with Wrap-Around Fins Using Computational Fluid Dynamics”, AIAA-93-3631, Flight Simulation and Technologies, Monterey, CA, USA, 09-11 August 1993.
- [13] Kim, J.Y., Cho, S., and Lee, I., “Aerodynamic Analysis of a Rolling Wrap-around Fin Projectile in Supersonic Flow”, Fourth International Symposium on Physics of Fluids (ISPF4), *International Journal of Modern Physics: Conference Series* Vol. 19 (2012) 276–282, 2012.
- [14] Li, M., Abbas, L.K., and Rui, X., “The Simulation of Wraparound Fins” Aerodynamic Characteristics”, *WSEAS Transactions on Applied and Theoretical Mechanics*, 2015.
- [15] Mikhail, A.G., “Roll Damping for Finned Projectiles Including: Wraparound, Offset and Arbitrary Number of Fins”, *Army Research Laboratory Report*, 1995.
- [16] Tanrikulu, O. and Mahmutyazicioglu, G., “Wrap around finned missiles: Neat but Nasty”, AIAA-97-3493, 22nd AIAA Atmospheric Flight Mechanics Conference, New Orleans, LA, USA, 11-13 August 1997.
- [17] Tanrikulu, O. and Mahmutyazicioglu, G., “Magnus Effects on Stability of Wraparound Finned Missiles”, *Journal of Spacecraft and Rockets*, Vol 35 no.4, 1998.
- [18] Sharma, N. and Kumar, R., “A Ready Reckoner of CFD for Wrap-around Fins”, *INCAS Bulletin*, Vol 11, 2019.

- [19] Despeyroux, A., Hickey, J.P., Desaulnier, R., Luciano, R., Piotrowski, M., and Hamel, N., “Numerical Analysis of static and dynamic performances of grid fin controlled missiles”, *Journal of Spacecraft and Rockets*, Vol 52., No. 4, pp. 1236-1252, 2015.
- [20] Bhagwandin, V. and Sahu, J., “Numerical Prediction of pitch damping stability derivatives for finned projectiles”, *Journal of Spacecraft and Rockets*, vol 51., no. 5, pp. 1603-1618, 2014.
- [21] Carlucci, D.E. and Jacobson, S.S., “Ballistics: Theory and Design of Guns and Ammunition”, CRC Press, Boca Raton, FL, pp.169-178, 257-281, 2008.
- [22] Park, S.H., Kim, Y., and Kwon, J.H., “Prediction of Damping Coefficients Using the Unsteady Euler Equations”, *Journal of Spacecraft and Rockets*, Vol. 40, No. 3, pp. 356–362, 2003.
- [23] Park, S.H., Kwon, J.H., and Kim, Y., “Prediction of Damping Coefficients Using Unsteady Dual-Time Stepping Method”, AIAA Paper 2002-0715, 40th AIAA Aerospace Sciences Meeting & Exhibit, Reno, NV, USA, 14-17 January 2002.
- [24] Sahu, J., “Numerical Computations of Dynamic Derivatives of a Finned Projectile Using a Time-Accurate CFD Method”, AIAA Paper 2007-6581, AIAA Atmospheric Flight Mechanics Conference, Hilton Head, South Carolina, USA, 20-23 August 2007.
- [25] DeSpirito, J., Sifton, S.I., and Weinacht, P., “Navier–Stokes Predictions of Dynamic Stability Derivatives: Evaluation of Steady-State Methods”, *Journal of Spacecraft and Rockets*, Vol. 46, No. 6, pp. 1142–1154, 2009.
- [26] Yayla, K., “Numerical Prediction of Aerodynamic Stability Derivatives of a Projectile”, Master of Science Thesis, Department of Aerospace Engineering, Middle East Technical University, September 2021.
- [27] Toro, E.F., “Riemann Solvers and Numerical Methods for Fluid Dynamics: A Practical Introduction”, Third Edition, Springer, 2009.
- [28] Blazek, J., *Computational Fluid Dynamics: Principles and Applications*, Elsevier, 2001.

- [29] Godlewski, E. and Raviart, P. A., “Numerical Approximation of Hyperbolic Systems of Conservation Laws”, *Applied Mathematical Sciences*, Vol 118, 1996.
- [30] Leveque, R.J., “Numerical Methods for Conservation Laws”, Springer, Basel AG, 1990.
- [31] Toro, E.F., Karni, S., Abgrall, R., Dumbser, M., and Kaman, T., “Lecture Notes on Numerical Methods for Hyperbolic Equations: Short Course Book”, CRC Press, ISBN 973-0-203-59062-1, 2011.
- [32] Hesthaven, J.S., “Numerical Methods on Conservation Laws from Analysis to Algorithms”, *SIAM*, 2018.
- [33] Bulat, P.V., Uskov, N.W., “Gas-dynamic Waves and Discontinuities”, *IEJME Mathematics Education*, Vol, 11, No 5, pp. 1101-1111, 2016.
- [34] Rohde, A., “Eigenvalues and Eigenvectors of the Euler Equations in General Geometries”, AIAA 2001-2609, 15th AIAA Computational Fluid Dynamics Conference, Anaheim, CA, USA, 11-14 June 2001.
- [35] Pope, S.B., *Turbulent Flows*, Cambridge University Press, Cambridge, 2000.
- [36] Spalart, P.R., “Strategies for Turbulence Modelling and Simulations”, *International Journal of Heat and Fluid Flow*, Vol. 21, pp. 252-263, 2000.
- [37] Heinz, S., “A Review of Hybrid RANS-LES Methods for Turbulent Flows: Concepts and Applications”, *Progress in Aerospace Sciences*, April 2020.
- [38] Spalart, P.R. and Allmaras, S.R., “A One Equation Turbulence Model for Aerodynamic Flows”, AIAA 92-0439, AIAA 30th Aerospace Sciences Meeting and Exhibit, Reno, NV, USA, 6-9 January 1992.
- [39] Spalart, P.R., Allmaras, S.R., Jou W.H., and Strelets, M.Kh., “Comments on the feasibility of LES for wings, and on a hybrid RANS/LES approach”, In Proceedings of first AFOSR international conference on DNS/LES, Greyden Press, 1997.
- [40] Spalart, P.R., Deck S., Schur M.L., Squires K.D., Strelets M.Kh., and Travin, A., “A New Version of Detached Eddy Simulation, Resistant to Ambiguous

- Grid Densities”, *Theoretical and Computational Fluid Dynamics*, 0935-4964, pp. 181-195, Springer-Verlag 2006.
- [41] Wilcox, D.C., “Formulation of the  $k-\omega$  Turbulence Model Revisited”, *AIAA Journal*, Vol. 46, No. 11, November 2008.
- [42] Menter, F.R., “Two Equation Eddy Viscosity Turbulence Models for Engineering Applications”, *AIAA Journal*, Vol. 32, No. 8, August 1994.
- [43] Calgaro, C., Creusé, E., Goudon, T., and Penel Y., “Positivity-preserving schemes for Euler equations: Sharp and practical CFL conditions”, *Journal of Computational Physics*, Vol. 234, pp. 417-438, 2013.
- [44] Barth, T.J. and Jespersen, D.C., “The design and application of upwind schemes on unstructured meshes”, AIAA-89-0366, AIAA 27th Aerospace Sciences Meetings, Reno, NV, USA, 9-12 January 1989.
- [45] Venkatakrishnan, V., “Convergence to Steady State Solutions of the Euler Equations on Unstructured Grids with Limiters”, *Journal of Computational Physics*, Vol. 118, pp. 120-130, 1995.
- [46] Ducros, F., Ferrand, V., Nicoud, F., Weber, C., Darracq, D., Gacherieu, C., and Poinso, T., “Large-Eddy Simulation of the Shock/Turbulence Interaction”, *Journal of Computational Physics*, Vol. 152, pp. 517-549, 1999.
- [47] Chamathi, A.S., Hoffmann, N., and Frankel, S., “A wave appropriate discontinuity sensor approach for compressible flows”, *Physics of Fluids*, Vol 35, 2023.
- [48] Zhang, F., Liu, J., and Chen, B., “Modified multi-dimensional limiting process with enhanced shock stability on unstructured grids”, *Computers & Fluids*, Vol 161, pp. 171-188, 2018.
- [49] Roe, P.L., “Approximate Riemann Solvers, Parameter Vectors and Difference Schemes”, *Journal of Computational Physics*, Vol 43, pp. 357-372, 1981.
- [50] Quirk, J.J., “A Contribution to the Great Riemann Solver Debate”, *International Journal for Numerical Methods in Fluids*, Vol 18, pp. 555-574, 1994.

- [51] Gottlieb, J.J. and Groth C.P.T., “Assessment of Riemann Solvers for Unsteady One-Dimensional Inviscid of Perfect Gases”, *Journal of Computational Physics*, Vol 78, pp. 437-458, 1988.
- [52] Toro, E.F., “A linearized Riemann solver for the time dependent Euler equations of gas dynamics”, *Proc. R. Soc. Lond.*, 434, pp. 683-693. 1991.
- [53] Einfeldt, B., Munz, C.D., Roe, P.L., and Sjögreen, B., “On Godunov-Type Methods near Low Densities”, *Journal of Computational Physics*, Vol. 92, pp. 273-295, 1991.
- [54] Jameson, A., Schmidt, W., and Turkel, E., “Numerical Solution of the Euler Equations by Finite Volume Methods Using Runge Kutta Time-Stepping Schemes”, AIAA-1981-1259, AIAA 14th Fluid and Plasma Dynamics Conference, Palo Alto, CA, USA, 23-25 June 1981.
- [55] Jameson, A., “The Origins and Further Development of the Jameson-Schmidt-Turkel Scheme”, *AIAA Journal*, Vol. 55, pp 1-23, 2017.
- [56] Jameson, A., “Analysis and Design of Numerical Schemes for Gas Dynamics, 1: Artificial Diffusion, Upwind Biasing, Limiters and Their Effect on Accuracy and Multigrid Convergence”, *International Journal of Computational Fluid Dynamics*, Vol. 4, pp. 171-218, 1995.
- [57] Jameson, A., “Analysis and Design of Numerical Schemes for Gas Dynamics, 2: Artificial Diffusion and Discrete Shock Structure”, *International Journal of Computational Fluid Dynamics*, Vol 5, pp. 1-38, 1995.
- [58] Liou, M. and Steffen, C.J., “A new Flux Splitting Scheme”, *NASA Technical Memorandum 104404*, May 1991.
- [59] Liou, M., “A sequel to AUSM: AUSM+”, *Journal of Computational Physics*, Vol. 129, pp. 364-382, 1996.
- [60] Liou, M., “A sequel to AUSM, Part II: AUSM+-up for all speeds”, *Journal of Computational Physics*, Vol. 214, pp. 137-170, 2006.
- [61] Harten, A., Lax, P.D., and van Leer B., “On Upstream Differencing and Godunov Type Schemes for Hyperbolic Conservation Laws”, *SIAM Review*, Vol. 25, 1983.

- [62] Rusanov, V.V., “The Calculation of the Interaction of nonstationary shock waves and obstacles”, *USSR Computational Mathematics and Mathematical Physics*, pp. 304-320, 1962.
- [63] Chiodaroli, E., Kreml, O., Mácha, V., Schwarzacher, S., “Non-uniqueness of admissible weak solutions to the compressible Euler Equations with smooth initial data”, *Transactions of the American Mathematical Society*, Vol. 374, pp. 2269-2295, 2021.
- [64] Palacios, F., Alonso, J., Duraisamy, K., Colonno, M., Hicken, J., Aranake A., Campos, A., Copeland, S., Economon, T., and Lonkar, A., “Stanford University Unstructured (SU2): An Open-source Integrated Computational Environment for Multiphysics Simulation and Design”, 51st AIAA Aerospace Sciences Meeting Including the New Horizons Forum and Aerospace Exposition, Grapevine, Texas, 7-10 January 2013.
- [65] Molina, E.S., Spode, C., Gil, R., da Silva, A., Manosalvas-Kjono, D.E., Nimmagadda, S., Economon, T., Alonso, J.J., and Righi, M., “Hybrid RANS/LES Calculations in SU2”, 23rd AIAA Computational Fluid Dynamics Conference, Denver, Colorado, 5-9 June 2017.
- [66] Molina, E.S., Silva, D.M., Broeren, A.P., Righi, M., and Alonso, J.J., “Application of DDES to Iced Airfoil in Stanford University Unstructured (SU2)”, *Progress in Hybrid RANS-LES Modelling*, pp. 283-293, 2019.
- [67] Sharma, S., Geyer, T., Sarradj, E., and Schmidt, H., “Numerical investigation of noise generation by rod-airfoil configuration using DES (SU2) and the FW-H Analogy”, AIAA-2019-2400, 25<sup>th</sup> AIAA/CEAS Aeroacoustics Conference, Delft, the Netherlands, 20-23 May 2019.
- [68] Fano, D., Poggie, J., and Blaisdell, G., “Aerodynamic Heating in Missile-Fin Interaction Region”, AIAA-2020-0583, AIAA SciTech Forum, Orlando, Florida, 6-10 January 2020.
- [69] Albring, T., Beckett, Y.Z., Gauger, N.R., “Challenges in Sensitivity Computations for (D)DES and URANS”, AIAA-2019-0169, AIAA SciTech Forum, San Diego, California, 7-11 January 2019.

- [70] Mortazawy, M., Kontis, K., and Ekaterinaris J., “A Numerical Investigation of Shock Wave Propagation in Ducts with Grooves”, AIAA-2020-1139, AIAA SciTech Forum, Orlando, Florida, 6-10 January 2020.
- [71] Park, M.A., Kleb, B., Anderson, W.K., Wood, S.L., Balan, A., Zhou, B.Y., and Gauger, N.R., “Exploring Unstructured Mesh Adaptation for Hybrid Reynolds-Averaged Navier Stokes/Large Eddy Simulation”, AIAA-2020-1139, AIAA SciTech Forum, Orlando, Florida, 6-10 January 2020.
- [72] Singh, K.K., Drikakis, D., Frank, M., Kokkinakis, I.W., Alonso, J.J., Economon, T.D., and van der Weide, E.T.A., “Comparison of the Finite Volume and Discontinuous Galerkin Schemes for the Double Vortex Pairing Problem using the SU2 Software Suite”, AIAA-2018-1833, AIAA SciTech Forum, Kissimmee, Florida, 8-12 January 2018.
- [73] Sacks, A.H., “Aerodynamic Forces, Moments and Stability Derivatives for Slender Bodies of General Cross Section”, NACA TN 3283, 1954.
- [74] Dupuis, A., “Aerobalistic Range and Wind Tunnel Tests of the Basic Finner Reference Projectile from Subsonic to High Supersonic Velocities”, TM 2002-136, Defence R&D Canada: Valcartier, QC, Canada, 2002.
- [75] Swalwell, K.E., Sheridan, J., Melbourne, W. H., “Frequency Analysis of Surface Pressures on an Airfoil after Stall”, AIAA Paper 2003-3416, 21st AIAA Applied Aerodynamics Conference, Orlando, Florida, 23-26 June 2003.
- [76] Swalwell, K.E., “The Effect of Turbulence on Stall of Horizontal Axis Wind Turbines”, PhD Thesis, Monash University, 2005.
- [77] Molina, S.E., Spode, C., da Silva, R.G.A., Righi, M., Economon, T.D., and Alonso, J.J., “Delayed DES in SU2: Test Case 3 from the Second AIAA Aeroelastic Prediction Workshop”, IFASD 2017.
- [78] Shur, M., Spalart, P., Strelets, M., and Travin, A., “Detached-eddy Simulation of an Airfoil at High Angle of Attack”, *Engineering Turbulence Modelling and Experiments*, Vol. 4, 1999, pp. 669-678, 1999.
- [79] Guseva, E. K., Garbaruk, A. V., and Strelets, M. K., “Assessment of Delayed DES and Improved Delayed DES Combined with a Shear-Layer-Adapted



- Subgrid Length-Scale in Separated Flows,” *Flow, Turbulence and Combustion*, 2016, pp. 1–22
- [80] Joaquin, L., Molton, P., Deck, S., Maury, B., and Soulevant, D., “Experimental Study of Shock Oscillation over a Transonic Supercritical Profile”, *AIAA Journal* Vol. 47, No. 9, 2009.
- [81] Smagorinsky, J., “General Circulation Experiments with the Primitive Equations”, *Monthly Weather Review*, Vol. 91, pp. 99-164, 1963.
- [82] Deardorff, J., “A Numerical Study of Three Dimensional Turbulent Channel Flow at Large Reynolds Numbers”, *Journal of Fluid Mechanics*, Vol. 41, pp. 453-480, 1970.
- [83] Weinacht, P. and Danberg, J.E., “Prediction of the Pitch-Damping Coefficients Using Sack’s Relations”, *Journal of Spacecraft and Rockets*, Vol 42, No. 5, pp. 865-872, 2005.
- [84] Ma, Y., Lv, M., and Su, C., “Numerical Simulation of Pitch-Damping Dynamic Derivatives”, EUCASS2019-78, 8<sup>th</sup> EUCASS, 2019.
- [85] Oktay, E. and Akay, H.U., “CFD Predictions of Dynamic Derivatives for Missiles”, AIAA-2002-0276, 40th AIAA Aerospace Science Meeting & Exhibit, Reno, NV, USA, 14-17 January 2002.
- [86] Shelton, A. and Martin C., “Characterizing Aerodynamic Damping of a Supersonic Missile with CFD”, 20180006293, *NASA Technical Reports Server*, 2018.
- [87] Kayabasi, I., “Numerical Investigation of Characteristics of Pitch and Roll Damping Coefficients for Missile Models”, Master of Science Thesis, Middle East Technical University, 2012.

## CURRICULUM VITAE

Surname, Name: Demirtaş, Uğurtan

### EDUCATION

Degree	Institution	Year of Graduation
MS	von Karman Institute Turbomachinery	2016
MS	TOBB ETÜ Mechanical Engineering	2015
BS	BOUN Mechanical Engineering	2011
High School	Samsun Science High School, Samsun	2006

### FOREIGN LANGUAGES

Advanced English

### PUBLICATIONS

1. Demirtaş, U. and Sezer-Uzol, N., "Comparison of Inviscid Flux Schemes and Turbulence Models on SU2 for Roll Induction Mechanism of Subsonic Missiles with Wrap-around Fins", 2nd SU2 Conference Virtual Event, July 12-14, 2021. (Abstract & Presentation) <https://su2foundation.org/su2conference2021/>.
2. Demirtaş, U. and Sezer-Uzol, N., "Numerical Investigation on Aerodynamic Roll Induction Phenomenon of Subsonic Wrap-around Tail Finned Missiles", AIAC-2021-087, 11th Ankara International Aerospace Conference, 8-10 September 2021, METU, Ankara, TURKEY.
3. Demirtaş, U. and Sezer-Uzol, N., "Parallel Performance Comparison of GMRES Type Sparse Matrix Solvers for Inviscid Flux Schemes using Open-Source CFD Solver SU2", BAŞARIM 2022, İstanbul, Türkiye, 11-13 Mayıs 2022.